STRUCTURAL IMPAIRMENT DETECTION USING ARRAYS OF COMPETITIVE ARTIFICIAL NEURAL NETWORKS

A Dissertation

by

BRETT ALAN STORY

Submitted to the Office of Graduate Studies of
Texas A&M University
in partial fulfillment of the requirements for the degree of

DOCTOR OF PHILOSOPHY

May 2012

Major Subject: Civil Engineering

Structural Impairment Detection Using Arrays of Competitive Artificial Neural Networks

STRUCTURAL IMPAIRMENT DETECTION USING ARRAYS OF COMPETITIVE ARTIFICIAL NEURAL NETWORKS

A Dissertation

by

BRETT ALAN STORY

Submitted to the Office of Graduate Studies of
Texas A&M University
in partial fulfillment of the requirements for the degree of

DOCTOR OF PHILOSOPHY

Approved by:

Chair of Committee,	Gary T. Fry
Committee Members,	Stefan Hurlebaus
	Harry Jones
	Anastasia Muliana
Head of Department,	John Niedzwecki

May 2012

Major Subject: Civil Engineering

ABSTRACT

Structural Impairment Detection Using Arrays of Competitive Artificial Neural Networks. (May 2012)

Brett Alan Story, B.S., Texas A&M University; M.S., Texas A&M University

Chair of Advisory Committee: Dr. Gary T. Fry

Aging railroad bridge infrastructure is subject to increasingly higher demands such as heavier loads, increased speed, and increased frequency of traffic. The challenges facing railroad bridge infrastructure provide an opportunity to develop improved systems of monitoring railroad bridges. This dissertation outlines the development and implementation of a Structural Impairment Detection System (SIDS) that incorporates finite element modeling and instrumentation of a testbed structure, neural algorithm development, and the integration of data acquisition and impairment detection tools. Ultimately, data streams from the Salmon Bay Bridge are autonomously recorded and interrogated by competitive arrays of artificial neural networks for patterns indicative of specific structural impairments.

Heel trunnion bascule bridges experience significant stress ranges in critical truss members. Finite element modeling of the Salmon Bay Bridge testbed provided an estimate of nominal structural behavior and indicated types and locations of possible impairments. Analytical modeling was initially performed in SAP2000 and then refined with ABAQUS. Modeling results from the Salmon Bay Bridge were used to determine measureable quantities sensitive to modeled impairments. An instrumentation scheme was designed and installed on the testbed to record these diagnostically significant data streams. Analytical results revealed that main chord members and bracing members of the counterweight truss are sensitive to modeled structural impairments. Finite element models and experimental observations indicated maximum stress ranges of approximately 22 ksi on main chord members of the counterweight truss.

A competitive neural algorithm was developed to examine analytical and experimental data streams. Analytical data streams served as training vectors for training arrays of competitive neural networks. A quasi static array of neural networks was developed to provide an indication of the operating condition at specific intervals of the bridge's operation. Competitive neural algorithms correctly classified 94% of simulated data streams. Finally, a stand-alone application was integrated with the Salmon Bay Bridge data acquisition system to autonomously analyze recorded data streams and produce bridge condition reports. Based on neural algorithms trained on modeled impairments, the Salmon Bay Bridge operates in a manner most resembling one of two operating conditions: 1) unimpaired, or 2) impaired embedded member at the southeast corner of the counterweight.

DEDICATION

To my family

ACKNOWLEDGEMENTS

The successful completion of this dissertation work benefitted from input from numerous individuals. I would like to express my great appreciation for my committee chair, Dr. Gary Fry. Dr. Fry's professional guidance, technical expertise, and enthusiasm for instruction were invaluable components of my success. I appreciate and respect both his confidence in my abilities and the patience he exhibited during my academic development.

I would also like to thank my committee members Dr. Stefan Hurlebaus, Dr. Harry Jones, and Dr. Anastasia Muliana for their input and support during my dissertation work. In addition to the professors on my committee, I would like to express my appreciation for the support of my research group office mates and Mrs. Amy White for her critique and review of my dissertation. I recognize Dr. Nicholas Marianos for his experienced advice and knowledge of bridge engineering. I would also like to thank Dr. Akram Abu-Odeh of the Texas Transportation Institute for his willingness and significant time commitment to instruct me in the methods of finite element modeling.

I thank Burlington Northern Santa Fe Railroad for their financial support of this work and for the opportunity to develop my research with such a unique testbed. Specifically, Mr. Steven Rogers and the BNSF crew at the Salmon Bay Bridge worked efficiently and safely and were instrumental in the success of the experimental components of this research.

I owe my family a debt that cannot be repaid. Because of their special support, I will always strive to exude the same level of support, service, and encouragement towards others.

Lastly, I would like to thank my wife Nicole. Undoubtedly, she has sacrificed the most throughout the years for my success. I cherish her overwhelming love, encouragement, and focused perspective. She has both given me the strength to perform academically, and provided much needed perspective on the priorities in my life.

TABLE OF CONTENTS

Page

CHAPTER Page

CHAPTER Page

LIST OF FIGURES

Page

Page

Page

Page

LIST OF TABLES

Page

Page

CHAPTER I
INTRODUCTION

1.1 Railroad Bridge Infrastructure

Civil engineering infrastructure such as bridges, buildings, and highways is susceptible to structural impairment which may inhibit acceptable functionality. Regular inspection and maintenance by federal and private owners facilitates uninterrupted, safe operation of infrastructure as many structures approach their intended design life spans (Hyland and Fry 1999, FRA 2010). The United States Department of Transportation reports that approximately 25% of the 600,000 U.S. highway bridges are structurally deficient or functionally obsolete (FHWA 2009). In addition to highway bridges, approximately 100,000 U.S. railroad bridges are owned, operated, and inspected (FRA 2010). Many of these railroad bridges are subject to service live loads well above their original design loads and continue in operation beyond their intended design lives (Leighty et al. 2004, AAR 2008). The need for increased freight efficiency is expected to drive the maximum weight of a coal car from 286 kips to 315 kips (Leighty et al. 2004). In addition to continually increasing car capacities, the amount of freight car traffic has increased approximately 80% from 19,500,000 carloads in 1985 to 35,000,000 carloads in 2008 (AAR 2008). Railroad bridges are critical components of rail infrastructure and warrant close scrutiny as many of the increased demands imposed on aging railroad bridges may not have been considered by the design engineers. Concern over railroad functionality has perpetuated an increase in track and structure expenditures from $29.31/ mile in 1955 to $40.16/ mile in 2006 (Weatherford et al. 2006).

Engineering decision making concerning the huge inventory of bridges in civil infrastructure relies on time consuming visual inspections. Inspections depend on the availability of inspection crews and, given the number of bridges that need monitoring,

---

This dissertation follows the style of the *Journal of Structural Engineering*.

inspection frequency may be inadequate to detect all impairments before a failure occurs. To facilitate the nominal operation of any infrastructure system, structural impairments should be discovered, reported, and addressed in a timely manner. An opportunity exists to create a system that aids and improves the efficiency of current monitoring practices (i.e. visual inspections).

1.2 Project Goal, Methodology, and Objectives

The overall goal of this dissertation research is to address challenges that arise when designing, deploying, operating, and maintaining a Structural Impairment Detection System (SIDS) that is capable of continuously assessing a specific structure to detect signatures of potential structural impairments. Despite the many efforts of both academic and industrial researchers to develop monitoring systems capable of detecting changes in readings from sensors, there is no real agreement about which technique or tool can detect and correctly identify changes in sensor reading that are, in fact, caused by structural impairment.

The SIDS presented in this dissertation is a continuous monitoring system that records relevant structural data and analyzes this data using pattern recognition algorithms to determine possible structural impairments at the Salmon Bay Bridge testbed. The numerical analysis tool implemented for pattern recognition is an array of neural networks. A neural network is a so-called soft computing method that "learns" and "remembers" relationships based on training data; relationships are then available for use with new data (Haykin 1999, Hagan 1996). Successful SIDS development ultimately depends on the ability of the neural network algorithm to efficiently interpret data from transducers and correctly classify the operational state of the bridge (i.e. detect impairments). The methodology to develop a SIDS is as follows:

1. Quantify nominal, or unimpaired, structural behavior,
2. Quantify changes in structural behavior caused by structural impairments,

3. Design sensor networks to create data streams that are sensitive to behavioral changes that indicate the presence of structural impairments,
4. Design, produce, and install instrumentation and a data acquisition system,
5. Develop competitive neural network algorithms that interrogate the data streams and alert decision makers to possible impairment, and
6. Integrate the data acquisition system and neural network algorithms to form a Structural Impairment Detection System.

The SIDS developed in this project is distinguishable from other methods of structural health monitoring (SHM) and non-destructive evaluation (NDE) presented in literature for key reasons. First, SIDS focuses on correlating detectable changes in structural behavior to known and probable impairments. Through detailed finite element modeling, professional inspections, and communication with engineers, bridge tenders, and railroad workers familiar with the bridge, researchers gain invaluable insight into what types of impairment are likely to occur. Rather than indicate only the presence of a change in structural behavior, a SIDS provides indication of a specific structural impairment that analyses or experience have shown to be likely.

A second distinguishing feature of SIDS is the use of an array of sensors specifically designed to detect expected impairments based on changes in the overall patterns of behavior. Having a network of sensors creates a data pattern that contains diagnostic content as it documents the interaction of several structural components. Impairment detection does not rely on one specific transducer at one specific location, but rather estimates the operational condition of the bridge through the analysis of patterns created by the global interaction of structural members.

1.3 Structural Health Monitoring and Non-Destructive Evaluation

Numerous efforts have been made to develop successful monitoring and damage detection systems for structural and mechanical systems (Sohn et al. 2001, Doebling et al. 1997). Structural health monitoring and non-destructive evaluation methods are

commonly classified into 4 levels ranging from an indication of damage (level 1) and adding requirements of damage location, severity estimation, and remaining service life for levels 2-4, respectively (Rytter 1993).

Many challenges in structural monitoring are highlighted in literature such as instrumentation and data collection, loading conditions of the structural system, and effective analysis of collected measurements (Doebling et al. 1997, Salawu 1995). Effective data collection is essential for monitoring and evaluating structures and is often made difficult by logistic considerations such as equipment shelter, power sources, and data storage (Catbas et al. 2009). Many structural health monitoring schemes rely on the measurement and evaluation of dynamic parameters of a structural system. Natural frequencies, mode shapes, curvatures, and a myriad of other dynamic measures are extensively investigated in literature. Some of these dynamic evaluations are hampered by the limitation of transducers to accurately measure and record the required number of frequencies and mode shapes necessary for the correct damage identification (Sohn et al. 2001, Salawu 1995). While different damage identification techniques require different measured parameters, some structural excitation must take place to produce measureable quantities of these parameters. For this reason, structural excitation is often a critical design parameter for a damage detection scheme (Salawu 1995). Excitation sources used in literature include vehicle traffic (DelGrego et al. 2008), imbalanced hydraulic shakers or impact hammers (Alwash 2010, Chopra 2001), and even seismic activity (Soyoz et al. 2009). The primary challenge of structural monitoring is to determine what information is needed and how best to utilize such information in engineering decisions (Liu et al. 2009).

1.4 Artificial Neural Networks

One key component in impairment detection is establishing a baseline, or "healthy" structural behavior (Doebling et al. 1996, Sohn et al. 2001). Material characteristics, connection details, typical wear, and random loading of bridge structures contribute to difficulties in accurate modeling and deterministic analysis of bridges to

establish a baseline behavior. One method of detecting patterns in data streams and relating them to particular damage states is through the use of neural networks. Neural networks are numerical computation tools, originally theorized on the cognitive abilities of the brain, which can classify data, map input data to output data, or find and distinguish patterns in data (Hagan 1996, Fausett 1994, Haykin 1999).

1.4.1 Characteristics and Theory of Neural Networks

Neural networks are an appealing approach to this research due to the immense complexity of the mathematical and physical models required to properly predict the behavior of the system (Bishop 1994). Neural networks provide a method of correlating the data from models and measured data in a manner that does not require exact matching of engineering values from models and measurements. Instead of directly comparing values for strains, stresses, and load effects in the bridge, patterns and trends in these measurements may be established and correlated to damage states. Neural networks may be an efficient method of analysis and data processing defined by trends and patterns, rather than the inexact or unknown relationships between structural response and structural impairment.

Neural networks were first conceptualized by Rosenblatt (1958) and were continually refined and improved to their current state by Rumelhart and Mclelland (1986). A neural network is a system of processors, or neurons, that are designed to roughly mimic the cognitive abilities of a brain (Minsky and Papert 1969, Hagan 1996). Input is entered and weighted through synapses into a neuron, which produces an output through the use of a non-linear transfer function (Haykin 1999). This simple system is called a perceptron (Rosenblatt 1958). Initially, a perceptron contains no information about the system it aims to predict; the neural networks learn relationships by adjusting synaptic weights that contain information about the system. One common training algorithm for neural networks is back propagation shown in Figure 1.1.

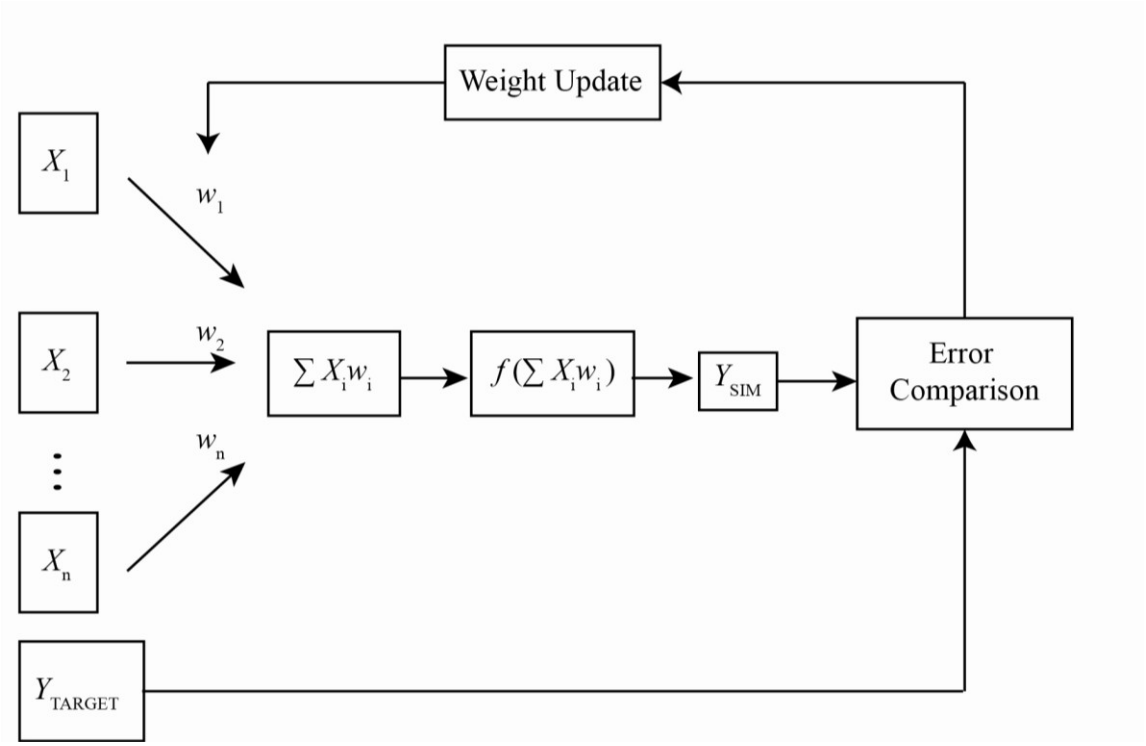

Figure 1.1: Back Propagation in a Perceptron

Training a neural network using back propagation consists of examining input (X_i) corresponding with a known output (Y_{TARGET}), providing the input to internal, non-linear functions in a neural network, and comparing the produced output (Y_{SIM}) with the known output. Some measure of error is calculated, and the weights in the neurons are updated to reduce the error through a gradient or steepest descent algorithm (Haykin 1999). The process is iterated until a stopping criterion is satisfied. Many stopping criteria are available to determine when the system has been properly trained; a common stopping criterion is error convergence below a specified tolerance between simulated output and target output (Hagan 1996, Haykin 1999). The neural network can then be used to determine the unknown output or classification corresponding to new input. Many layers of neurons can be used to form an entire neural network that, when given

input different from training input, can sort and determine, through its neurons, a previously-taught classification or new output (Hagan 1996). Effective neural network architectures and training parameters vary significantly by application, and many techniques such as genetic algorithms have been proposed to determine an optimum configuration for a specific application (Haykin 1999).

1.4.2 Application of Neural Networks to Structural Engineering Research

Neural networks have been applied in the field of engineering research towards structural analysis (Kortesis and Panagiotopoulos 1993), structural damage detection in laboratory conditions (Chang et al. 2000, Li et al. 2004, Fang et al. 2005, Lee et al. 2006), and control of aerospace systems (Hyland and King 1992, Hyland and Davis 2002). The most popular approach to damage detection using neural networks focuses on dynamic properties such as frequencies and mode shapes. Yeung and Smith created a feature vector from the dynamic properties of a structural model subject to various damage states and reported 70% damage identification (2005). Neural networks trained on displacement data have also been shown to successfully locate and identify damage types in trusses (Pandey and Barai 1995). Barai and Pandey also demonstrated that dynamic neural networks perform better than traditional neural networks in some instances (1996).

While the successful implementation of neural networks has been demonstrated in ideal laboratory conditions, translating the same level of success to an in situ structure, such as a railroad bridge, is difficult. Training a neural network requires a large amount of data (for many possible damage states) which can be produced in a model. Equivalent appropriate data from a complex structure may be difficult, unsafe, or impossible to obtain. Unknown variations in loading, material composition and interaction, and structural geometry make it difficult to accurately validate a model. While matching values for deflections or stresses exactly between a real structure and a computer model is not realistic outside of a simple laboratory experiment, one does expect that the overall behavior of a structure can be captured in a structural model, and trends in behavior can be validated. The most beneficial feature of the neural network

approach in a SIDS is the ability of the network to examine trends in structural behavior and identify patterns that correspond to impairment. A successful SIDS implementation consists of instrumentation and a data acquisition system running in tandem with a neural network based analysis algorithm.

1.5 Strauss Heel Trunnion Bascule Bridges

Critical instances of reliable railroad bridge functionality arise in situations where waterway transportation conflicts with bridge traffic. Movable bridges can be designed to accommodate both flows of traffic; movable bridge types include swing bridges, lift bridges, and bascule bridges (Hool and Kinne 1923). Historically, the most popular movable bridge design is the bascule bridge (Reichmann 1924, Hool and Kinne 1923).

1.5.1 Components and Theory of a Heel Trunnion Bascule Bridge

Figure 1.2 illustrates the components of a typical heel trunnion bascule bridge. Ideally, the pinned parallelogram linkage bounded by the leaf, tower, counterweight truss, and counterweight link allows a prescribed, continual adjustment of the leaf and counterweight so that moment equilibrium is satisfied (Waller and Pircher 2007). Bascule bridges operate through a prescribed motion allowed by a mechanism consisting of cylindrical bearings (two trunnions and two pins). Figure 1.2 illustrates the unstable parallelogram mechanism indicated by the red, dashed line.

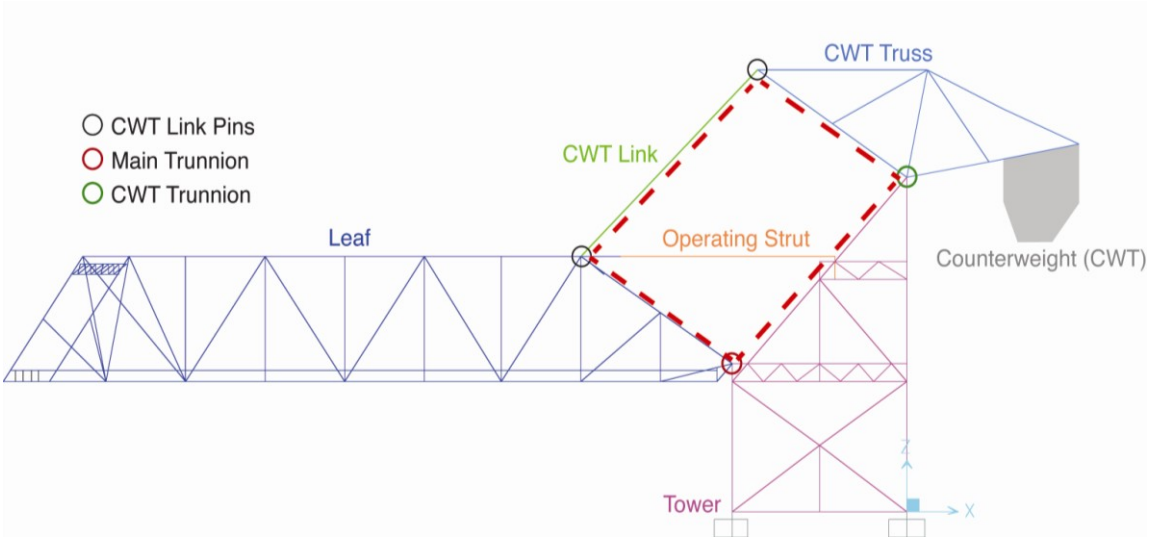

Figure 1.2: Heel Trunnion Bascule Bridge Components

The leaf rotates about the main trunnion (or "heel trunnion") which serves as one pivot axle of the structure. A second pivot axle, or counterweight trunnion, is located at the top of the tower and allows the counterweight truss supporting the counterweight to pivot as the leaf rotates about the main trunnion. The operating strut stabilizes the linkage, and the bridge is opened and closed by this rack and pinion mechanism. Theoretical moment balance allows the bridge to be opened and closed with relatively little external torque provided by motors located on the bridge (Reichmann 1924).

Heel trunnion bascule bridges utilize a very large reinforced concrete counterweight to balance the leaf (span) throughout operation of the bridge (Hool and Kinne 1923). A counterweight model, shown in layers in Figure 1.3, consists of a steel frame embedded in concrete with several pockets used for the addition of balancing weight (sections of steel rail and concrete blocks) to fine tune the balance of structure.

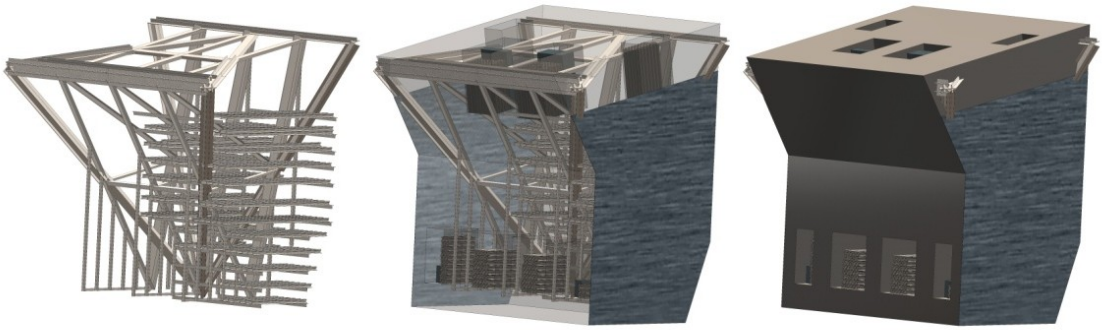

Figure 1.3: SolidWorks Counterweight Model

The drive shaft/operating strut system raises and lowers the leaf and produces the forces necessary for the equilibrium of the bascule mechanism while the bridge is operating. Each drive shaft is driven at one end by machinery in the machine room and is supported at the other end by a bearing at the truss line. Pinion gears on the outer ends of the drive shafts interlock with racks on the undersides of the operating struts as shown in Figure 1.4.

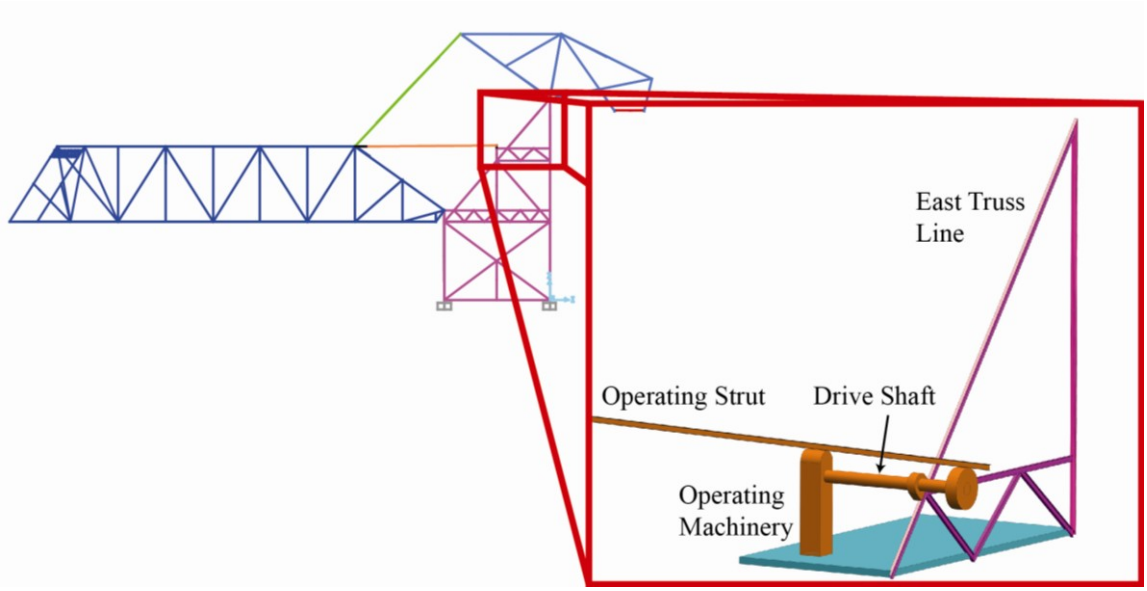

Figure 1.4: Schematic of Drive Shaft and Operating Strut

Traditionally, the cost of building bascule bridges can be more than the cost for other moveable bridges. The cost for building the structural components of the bridge can be similar for any type of bridge. A Strauss heel trunnion bascule bridge has a counterweight which adds to the production cost of the bridge. Constructing the reinforced concrete counterweight increases the initial construction costs of a bascule bridge over other bridge types; however, considering the entire life of a bascule bridge generally results in a more cost efficient movable bridge solution (Hool and Kinne 1923).

1.5.2 Heel Trunnion Bascule Bridge Failures

While popular, heel trunnion bascule bridges have not been without problems and failures. Bascule bridges are subject to full cycles of opening and closing on a daily basis, and thus component fatigue and trunnion operation are chief concerns. Deterioration of these bascule bridges has caused several failures in various stages of service life. The Hackensack Bascule Bridge in New Jersey failed in 1928 after approximately 1 year of service. As the bridge was being lowered, the counterweight

truss failed and toppled into the river. Causes of the failure, such as poor trunnion maintenance or improper design for dynamic loads, were debated (Paine 1929). In 1947, the counterweight of the Cherry Street Bascule Bridge in Toronto fell after 30 years of service. In this instance, the cause of failure was agreed to be the deterioration of the bond between the counterweight truss framing and the concrete counterweight itself (Graydon 1949).

1.5.3 Motivation for a Heel Trunnion Bascule Bridge Testbed

The dynamic nature of bascule draw bridges distinguishes them from most bridge structures and provides many unique opportunities and challenges in engineering research. From a modeling and instrumentation perspective, dynamic features present challenges. Careful consideration and planning can overcome these challenges. Many characteristics of bascule bridges provide the unique opportunity to circumvent a separate and more critical set of challenges faced in the arena of structural monitoring and damage assessment. One example of a critical issue present in many damage assessment methods is the loading of the test structure (Doebling et al. 1997, Salawu 1995).

Two loading concerns are the ability to provide an excitation to the structure that produces useful data and uncertainty in loading caused by traffic or environmental effects. Bascule bridges are especially unique because they need no external excitation to produce useful data; their self-imposed excitation when opening and closing supplies ample, repeatable loading and diagnostic data.

Heel trunnion bascule bridges are logistically attractive as their machine rooms and operating houses provide on-site shelter, power, and even internet access for data acquisition equipment. The characteristics of bascule bridges provide opportunities typically unavailable on fixed bridges to develop automated damage assessment through SIDS.

1.6 Salmon Bay Bridge Testbed

The bascule bridge studied for this project is an excellent case of aging infrastructure subject to increased demand. Built in 1913, the Salmon Bay Bridge is a bascule bridge that spans a high traffic volume waterway called Lake Washington Ship Canal, or Salmon Bay. Figure 1.5 is a photograph of the Salmon Bay Bridge partially open. The bridge lies on a main railroad line for the Burlington Northern Santa Fe (BNSF) Railroad and supports two main railroad tracks. The bridge was traversed by an average of 41 trains per day in 2007 (BNSF 2007). The Salmon Bay Bridge has served as a test bed for SIDS implementation since 2009.

Figure 1.5: Salmon Bay Bridge Testbed

The bridge opens when signaled by marine vessels passing through. When fully opened, the main clearance of the bridge reaches 150 feet horizontally; while closed, the clearance is about 40 feet during the highest tide. This bridge employs a 1,500 ton counterweight to balance the 200 ft leaf.

Particularly close scrutiny is required for the Salmon Bay Bridge as its counterweight truss fractured in 1948 due to fatigue and detailing of one of the steel counterweight truss members near a panel point counterweight connection (Wilson 1948). The bridge was taken out of service in 1948 when a steel member fractured near the counterweight connection at panel point 33 as shown in Figure 1.6. The counterweight and several counterweight members were redesigned, replaced, and the bridge has since been in service. This failure was determined to be caused by stress reversal and fatigue within the counterweight truss just outside a counterweight connection (Wilson 1948).

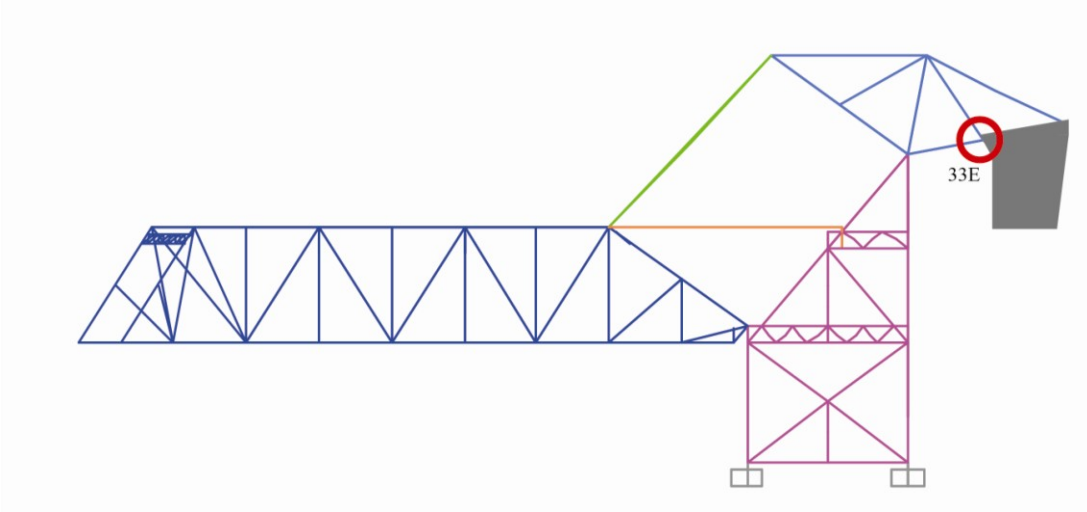

Figure 1.6: Location of 1948 Counterweight Failure

The Salmon Bay Bridge has experienced continual changes throughout its operation. Upgrades were made to the mechanical, electrical, and signal systems in 1992. Over the last decade, the retainer pins were replaced at counterweight trunnion bearings, end span locks were added, and stringers under the rail joints at the heel end of the bascule were replaced (BNSF 2007). During the monitoring effort for this project, the counterweight trunnions were replaced. Seattle is in a seismic zone and the bridge experienced earthquakes in 1949, 1965, and 2001 (BNSF 2007).

CHAPTER II
ANALYTICAL PROCEDURES

2.1 Objectives and Methodology of Analytical Work

The ultimate goal of this dissertation is to develop a competitive, neural algorithm capable of detecting structural impairments. Before designing the neural processing algorithms, several intermediate analytical tasks were completed to create training data for the neural networks. The design of data streams necessary for the development of neural processing algorithms was carried out through the analysis of the Salmon Bay Bridge, which also served as an experimental testbed. Chapter III outlines the experimental procedures associated with data collection at the testbed.

2.2 Structural Modeling of the Testbed Structure

Detecting and classifying abnormal structural behavior requires a thorough understanding of the nominal behavior of a given structure. Prerequisite knowledge of a specific structure's intended design behavior is especially important when designing data streams for the development of an impairment detection system. Quantified nominal, intended structural behavior serves as a reference with which to compare experimental results and provides an undamaged solution with which to train neural networks for impairment detection. The specific objectives of modeling the Salmon Bay Bridge are to:

1. Establish the nominal, unimpaired behavior of the bridge,
2. Identify the types and locations of impairments,
3. Identify member locations sensitive to modeled impairments that can be used to develop experimental instrumentation,
4. Verify field measurements, and
5. Create data streams representative of impairment scenarios with which to train structural impairment detection systems.

An accurate mathematical structural model provides information that is impractical or impossible to obtain in field or experimental situations. The effects of modeled impairments, connectivity of structural components, and variation of masses and geometries are easily investigated with a structural model. Altered responses of structural components caused by structural variations serve as training examples for neural algorithms; results produced with an analytical structural model are obtained safely, quickly, and inexpensively.

2.2.1 Member Designations on the Salmon Bay Bridge

Figure 2.1 indicates the panel point designation numbers for the Salmon Bay Bridge counterweight truss. The counterweight structure is composed of east and west trusses with bracing members and the reinforced counterweight providing lateral connection and stability. Member identification of the main east and west truss members consists of the panel points that bound the member and the indication of the east or west truss, (i.e E or W). For example, the east main chord from panel point 29 to panel point 33 is designated by 29-33E. Bracing members follow a similar pattern, but include an 'X' designation. For example, the bracing member running from east panel point 29 to west panel point 33 is designated by X29-33EW. Panel points are designated by their number and an indicating presence on the east or west truss line.

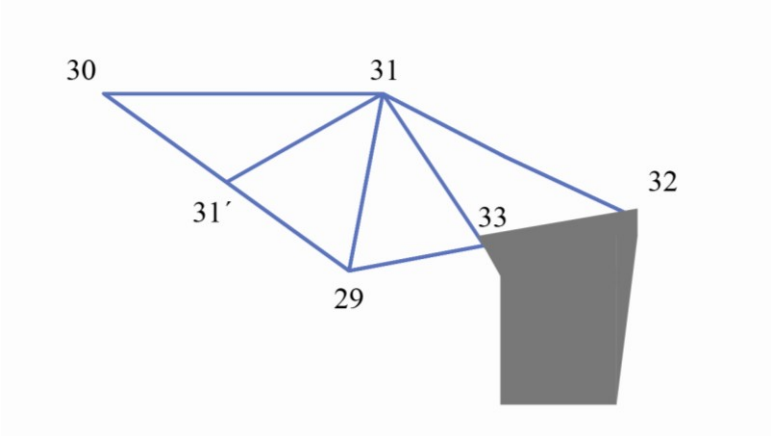

Figure 2.1: Counterweight Truss Panel Point Designations

2.2.2 Loading of the Structural Model

Bascule bridges exhibit unique dynamic behavior and present challenges in analysis, design, and evaluation. A successful analytical model should capture the important features resulting from this dynamic behavior. The dynamic nature of bascule bridges necessitates the evaluation of mechanical components that control bridge movements and consideration of the possible effects of accelerations on behavior. In normal operation, angular accelerations are assumed to be small, the bridge is essentially subject to free vibration, and is expected to oscillate about some static deflection for each angle (Frýba 1996, Chopra 2001). Under these behavioral assumptions, the Salmon Bay Bridge was modeled as a series of static models of the bridge opened to 0, 20, 40, 60, 75, and 82.5 degrees. Only self-weight dead loads were considered in the analyses.

2.2.3 Component Weight

As a bascule bridge opens and closes, counterweight truss members experience changes in stress as the counterweight rotates about its supporting trunnions. As the bridge moves through its prescribed motion, members reorient themselves in space, while the loading from the self-weight of the structure remains vertical. Laced structural members and, most significantly, the reinforced concrete counterweight are the primary sources of structural self-weight. Member weights represent the gross self-weight of the member sections, lacing weight, and rivet head weight. Finite element programs calculate member weights based on supplied cross-sectional area, length, and member density. The inclusion of lacing weight and rivet head weight was achieved by increasing the member densities by appropriate amounts. For members with significant lacing, a 10-20% increase in self-weight is observed. Rivet heads also add significantly to the weight of some structural members. Estimations of percent weight increases from rivet heads are based on member type and range from 4% for truss members up to 8% for built up column members (Ketchum 1914). Other sources of dead load on the structure include weights from the connection details at joints, operating machinery and the machine room floor, track structure, and miscellaneous balancing weight added to both the toe of the bridge and to the counterweight adjustment pockets. A summary of

component weights is given in Table 2.1. Final weights from SAP2000 models were compared to hand calculations from 1948 design documents provided by BNSF.

Table 2.1: Salmon Bay Bridge Component Weight Summary

Component	SAP2000 Weight (k)	1948 Weight (k)	% Difference
Leaf	1185.7	1159.0	2.3
CWT and CWT Frame	3525.0	3522.7	0.0
Links	88.4	96.0	-8.6
Operating Struts	41.0	40.8	0.5
Tower	709.9	n/a	n/a
Total Excluding Tower	4840.1	4818.4	0.5
Total Including Tower	5550.0	n/a	n/a

2.2.4 Counterweight Investigation

The reinforced concrete counterweight is one of the most dominant influences on the structural behavior of a bascule bridge (Hovey 1926, Hool and Kine 1923). Owing to this influence, considerable time was devoted to the creation of a detailed counterweight model in SolidWorks. The effect of the counterweight on structural behavior depends on its mass properties. Mass, mass moment of inertia, and the center of gravity (C.G.) location are all factors that affect the behavior of the bridge. The weight and location of the counterweight C.G. affects the counterweight member stresses, and the drive shaft torque is extremely sensitive to the counterweight's C.G. location. The bridge's natural frequency is affected by all mass properties. The SolidWorks mass property calculator extracted accurate mass, mass moment of inertia, and C.G. information for use in the structural model (SolidWorks 2011). Hand estimates, SolidWorks calculations, and the 1948 calculations of counterweight mass properties are shown in Table 2.2.

Table 2.2: Mass Properties of Counterweight

Calculation Method	Mass	Center of Gravity			Mass Moment of Inertia
	M_{CWT} (slug)	x (ft)	y (ft)	z (ft)	I_{CWT} (slug-ft^2)
Hand Est.	95.65	38.75	-4.60	-0.42	1.57E+08
SolidWorks	95.50	38.44	-5.95	-0.24	1.61E+08
1948 Est.	95.58	38.40	-5.70	n/a	n/a

The masses given in Table 2.2 include gross concrete and side plates, the embedded steel frame, and contents of the counterweight pockets. The C.G. coordinates are measured from the counterweight trunnion as shown in Figure 2.2. The mass moment of inertia is calculated with respect to the counterweight trunnion.

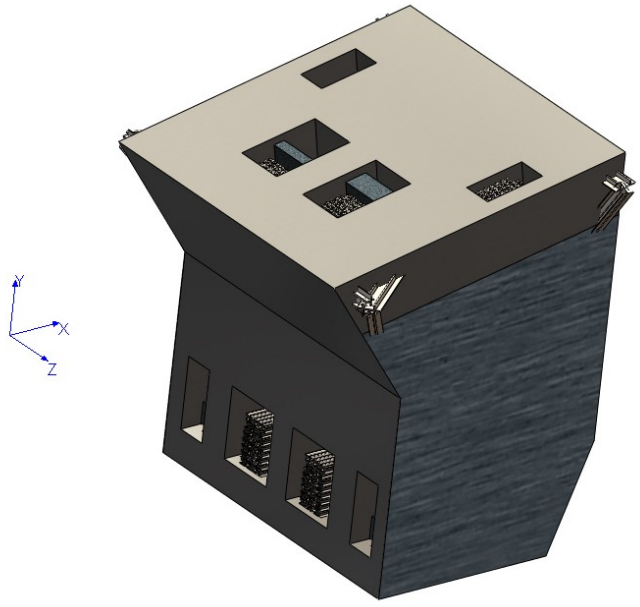

Figure 2.2: Counterweight Mass Property Coordinate System

2.3 Structural Modeling in SAP2000

The finite element analysis program SAP2000 was used to investigate the Salmon Bay Bridge. Static models provided load effects resulting from dead load acting on the structure. Figure 2.3 shows a three dimensional finite element model opened to 60 degrees. Member stresses were obtained from load effects at various locations on the structure. The analyses carried out in SAP2000 included a static and modal analysis for each angle of opening considered.

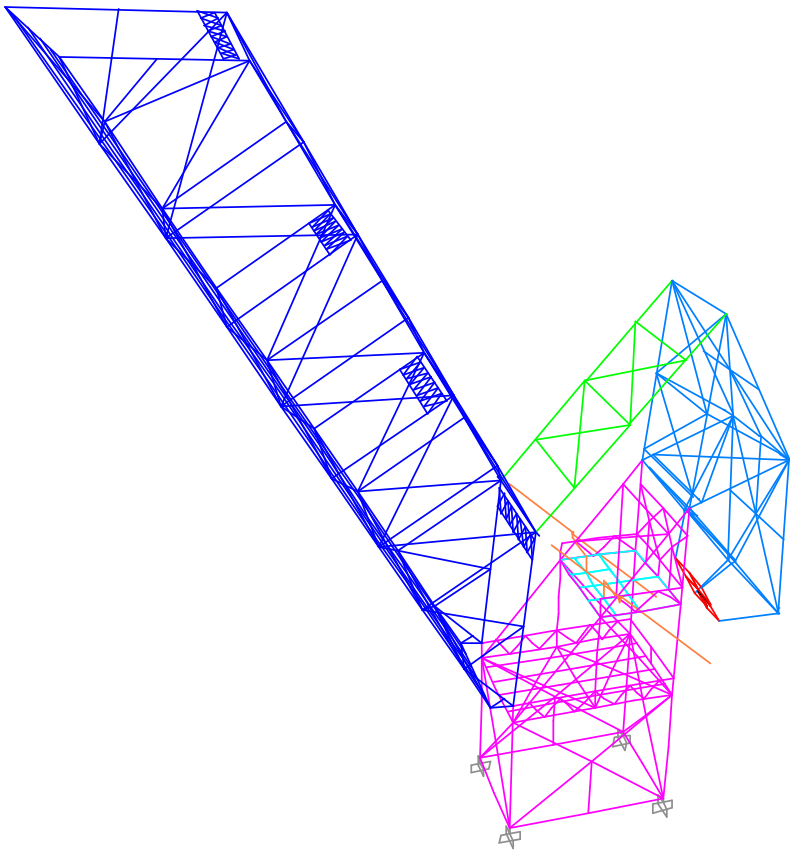

Figure 2.3: SAP2000 Model of Salmon Bay Bridge

2.3.1 Counterweight Modeling in SAP2000

The reinforced concrete counterweight was represented in SAP2000 as a rigid mass located at the appropriate C.G. The red plates in Figure 2.4 represent the rigid counterweight and are connected to members of the counterweight truss shown in blue. The varying thicknesses of the rigid plates defined the counterweight C.G.

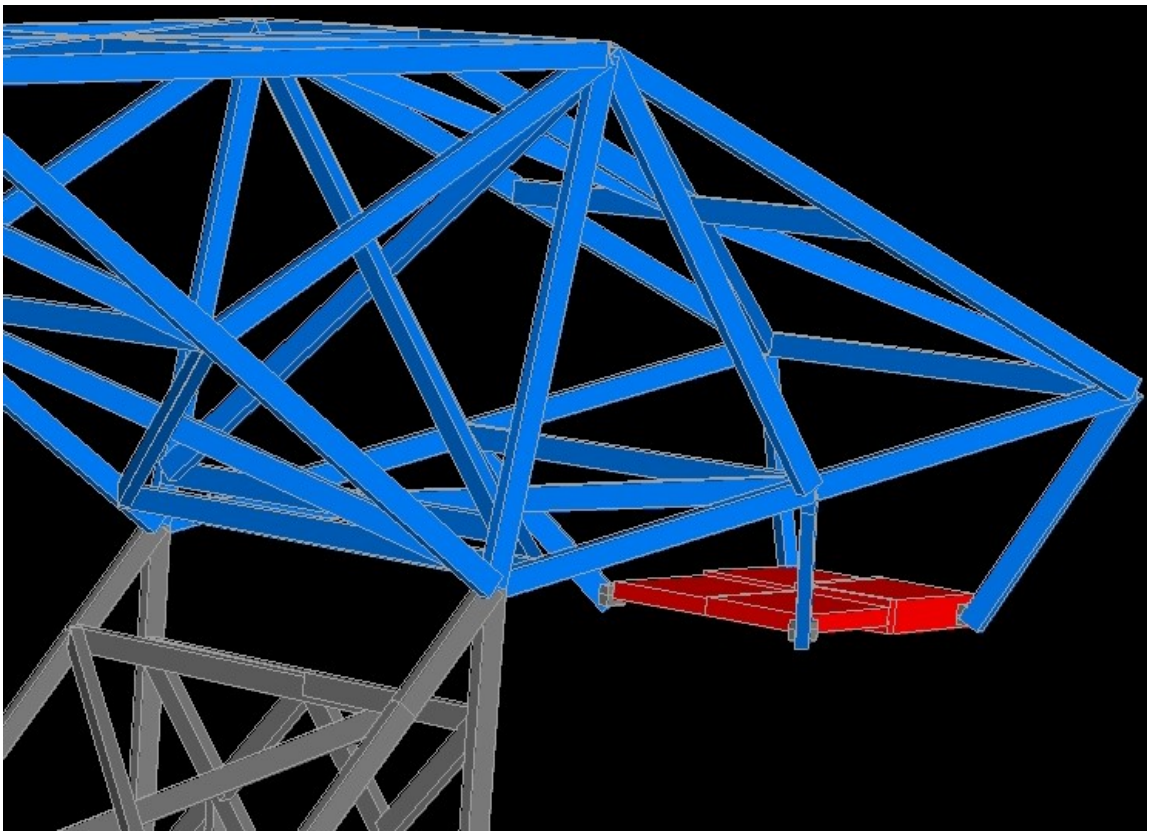

Figure 2.4: SAP2000 Counterweight Model

In reality, the four members of the counterweight truss in the model are actually embedded in concrete. A particularly challenging aspect of modeling a bascule bridge counterweight was modeling the appropriate load transfer from the counterweight to the

supporting counterweight truss members. These counterweight connections consist of fully or partially embedded counterweight truss members; the exact connectivity and bond between the steel and concrete is unknown. In an effort to capture the upper and lower bound of this connectivity, several states of connectivity for members framing into the counterweight were explored. To simulate a loss of bond between the concrete and the embedded steel frame, the stiffnesses of the counterweight frame members were varied. Figure 2.5 highlights typical areas where member connections were altered. For example, one extreme modeling case assumed that any member fully embedded in the concrete counterweight was rigid; this assumed there was a perfect bond between the steel and concrete and that the entire volume of concrete was rigid. Another case modeled assumed that some de-bonding of the concrete from the steel had occurred at the corners of the counterweight truss (33E, 33W, 32E, and 32W). Accordingly, the stiffnesses of short portions (~6 in.) of the embedded members were reduced from rigid to the actual section properties of the members. Significant variations in stress ranges in 29-33E and 29-33W were observed when embedment lengths and stiffnesses were varied. While SAP2000 was key in discovering this sensitivity, a refined analysis was completed in ABAQUS. Details of this refined analysis are given in Section 2.5.

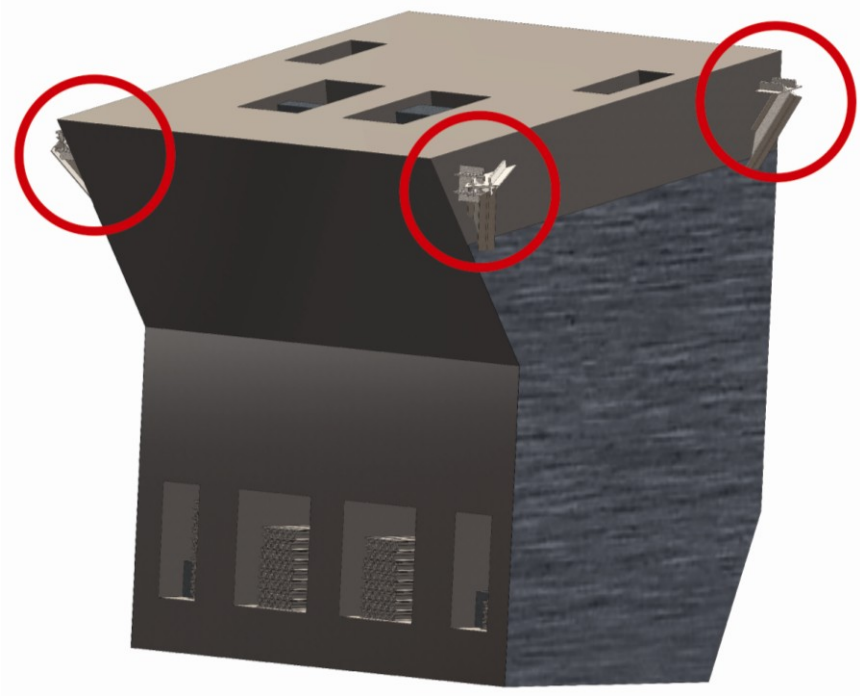

Figure 2.5: Counterweight Connection Areas

2.3.2 Structural Member Modeling in SAP2000

Members of bascule bridge truss systems undergo large movements and load redistributions that result in stress ranges significantly higher than fixed bridges (Koglin 2003). High stress ranges in steel members raise concerns about the fatigue life of the structure (Wilson 1948, Koglin 2003). The primary source of diagnostic information for fatigue concerns in counterweight truss members of bascule bridges came from the examination of the counterweight truss members' behavior. Structural members in SAP2000 models were represented by six DOF frame elements with appropriate moment releases for counterweight link members, drive shafts, and operating struts. All Salmon Bay Bridge members were modeled with cross sectional properties calculated from drawings provided by BNSF. Areas, second moments of area, and torsion constants were

extracted or calculated from the drawings and applied to frame elements in the model. In SAP2000, only gross areas were modeled, but individual member densities were altered to include the added weights of lacing and rivet heads.

Chapter I describes the kinematic motion of a bascule bridge. The pins and trunnions responsible for such movement affect the behavior of counterweight truss members and counterweight link members; moments about these axes of rotation are zero. Counterweight link members and truss members framing into these pins were modeled with moment releases in the plane of rotation. This modeling technique allowed for rotation about trunnions and link pins, and, in the absence of operating struts, rendered the model unstable. The results of SAP2000 confirmed this unstable behavior when operating struts were removed.

A simple, two dimensional truss analysis of the structure served as an additional validation of the structural the model. Nodal loads were calculated based on tributary lengths of members and all dead loads. After a static hand calculation, the results were compared to a static, two dimensional SAP2000 truss model. These results matched exactly and were compared to the three dimensional frame model and the 1948 values provided in the BNSF drawings. Table 2.3 compares these three dimensional SAP2000 model results, two dimensional hand calculations, and SAP2000 truss results. Table 2.4 compares estimations of maximum and minimum axial forces experienced by the bridge during an opening from the model and 1948 calculations. The results in Tables 2.3 and 2.4 were satisfactory as a preliminary check of the model's validity when examining axial forces in the counterweight truss.

Table 2.3: Comparison of Member Axial Force Results to Two Dimensional Truss Analyses

Member	Hand Statics (k)	SAP2000 2D Truss Model (k)	SAP2000 3D Frame Model (k)
Links	1139	1139	1178
29-31'	-1537	-1537	-1539
30-31'	-1518	-1518	-1514
30-31	2014	2014	1957
31-32	1549	1549	1510
33-32	-1417	-1417	-1700
29-33	-1825	-1825	-1840
29-31	-1342	-1342	-1389
31-33	704	704	715
31'-31	18	18	28

Table 2.4: Comparison of Maximum/Minimum Axial Force Results to 1948 Estimations

Member	SAP2000 3D Frame Model (k)		1948 Results (k)	
	Tension	Compression	Tension	Compression
Links	1143	n/a	1130	n/a
29-31'	n/a	-1764	n/a	-1706
30-31'	n/a	-1733	n/a	-1687
30-31	1910	n/a	1937	n/a
31-32	1460	-674	1625	-832
33-32	1431	-1701	1643	-1730
29-33	1679	-1798	1678	-1755
29-31	n/a	-1374	n/a	-1360
31-33	1149	n/a	1210	n/a
31'-31	27	-11	14	-8

2.3.3 Drive Shaft and Operating Strut Modeling

A unique aspect associated with modeling a heel trunnion bascule bridge was the representation of the drive shafts and operating struts. Torque values in the drive shafts were useful in validating the calculated weights and C.G. values of bridge components. The application of appropriate boundary conditions in SAP2000 models created accurate load effects in the shaft without explicitly modeling a bearing condition. The boundary conditions are labeled in Figure 2.6. The driveshaft was fixed at the point where it engages the drive machinery. The shaft was subdivided where it frames into the bearing at the truss line and torsion and bending moments were released, but deflection was constrained by the truss. Rigid links (depicted by green members in Figure 2.6) transferred torque values to the outer portion of the subdivided shaft. The pinion was represented by another rigid link with a length corresponding to the pinion gear radius. The connection between the operating strut and driveshaft forced equal displacement of the pinion link end and operating strut, but bending moments were released.

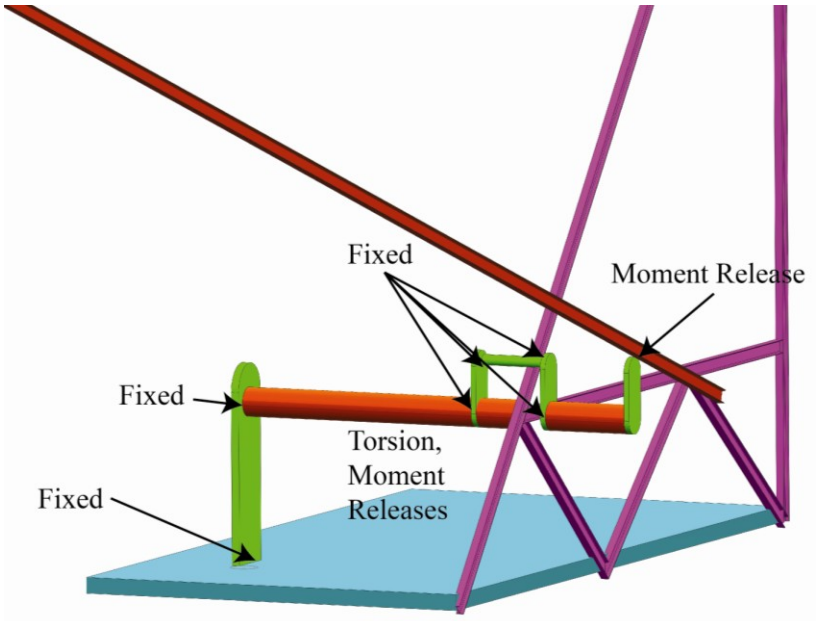

Figure 2.6: Modeling Boundary Conditions of Drive Shafts and Operating Struts

This arrangement accurately transferred the force in the operating strut into the drive shaft and created a torque in the shaft. A preliminary examination of the model's ability to transmit this force properly was verified by a simple calculation of the angle of twist experienced by the drive shaft. The torque in the drive shaft is a product of the axial force in the operating strut and the radius of the pinion

$$T = F_{\mathrm{OP}} r_{\mathrm{S}} \tag{2.1}$$

The angle of twist is expressed as

$$\varphi_{\mathrm{s}} = \frac{T L_{\mathrm{S}}}{G J_{\mathrm{S}}} = \frac{F_{\mathrm{OP}} r_{\mathrm{S}} L_{\mathrm{S}}}{G J_{\mathrm{S}}} \tag{2.2}$$

Substituting,

F_{OP}	=	53.8 k
r_{s}	=	12.5 in.
L_{s}	=	140 in.
G	=	11153.8 ksi
J_{s}	=	1437.4 in.^{4}

The rotation at the end of the drive shaft is

$$\varphi_{\mathrm{s}} = \frac{F_{\mathrm{OP}} r_{\mathrm{S}} L_{\mathrm{S}}}{G J_{\mathrm{S}}} = \frac{(53.8)(12.5)(140)}{(11153.8)(1437.4)} = 0.0059 \text{ radians} \tag{2.3}$$

The SAP2000 value for rotation at the pinion end of the drive shaft was 0.0059 radians. With confidence in the SAP2000 torque values resulting from an axial force in the operating strut, a more extensive analysis of drive shaft torque as a function of

opening angle was performed. A two dimensional analytical model was created by examining free body diagrams (FBD) of the counterweight truss, leaf, and the operating strut. Figure 2.6 depicts a schematic of the bridge and its corresponding idealization used to construct free body diagrams for the development of the torque model. The structure is idealized by masses attached to rigid links (shown in blue in Figure 2.7).

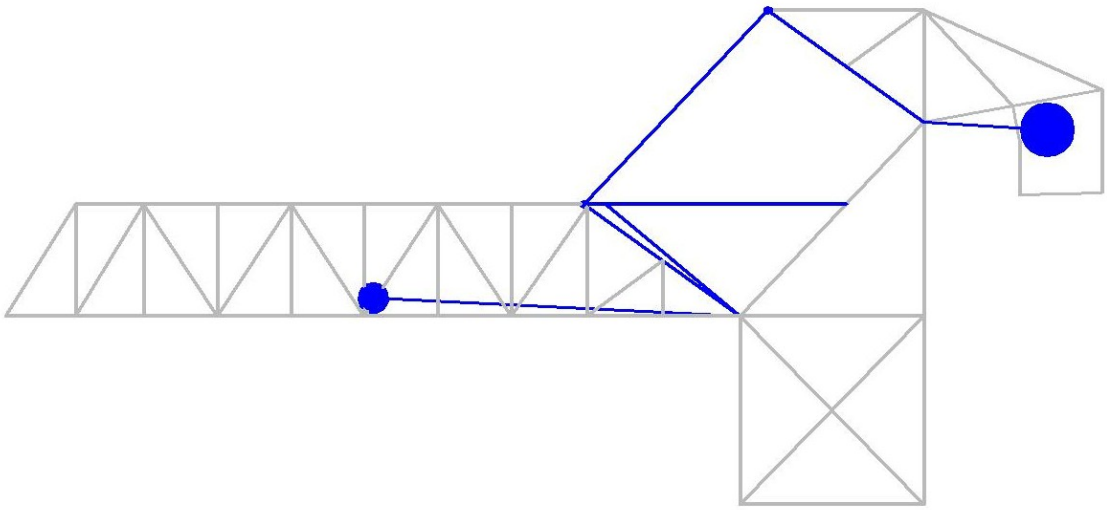

Figure 2.7: Idealized Model for Torque Analysis

Torque as a function of angle is given in Equation 2.4 and is a function of initial geometry and bridge angle. The details of the derivation are given in Appendix A. Figure 2.8 compares torque vs. angle results from Equation 2.4 and SAP2000 models.

$$T = r_s \left\{ \left[W_{LEAF} R_{LEAF} \cos(\theta_{LEAF} + \theta) + \frac{W_{LK}}{2} R_{LK} \cos(\theta_{LK} + \theta) \right.\right. \\ + (Fa_y) R_{PIN} \cos(\theta_{PIN} + \theta) + Fa_x R_{PIN} \sin(\theta_{PIN} + \theta) \\ \left.\left. - M_{LK} \right] / 2[R_{PIN} \sin(\theta_{PIN} + \theta - \beta)] \right\} \tag{2.4}$$

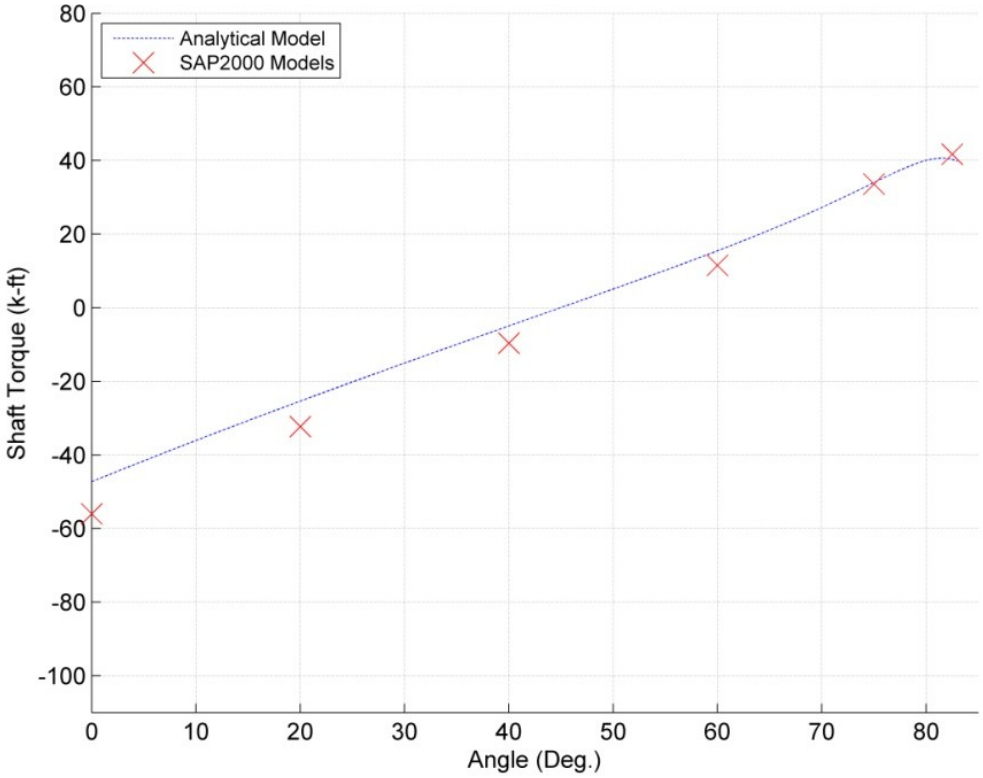

Figure 2.8: Preliminary Drive Shaft Torque Results

2.3.4 Dynamic Modeling in SAP2000

The dynamic opening of the Salmon Bay Bridge was modeled considering separate static models at various angles of opening. Because of the slow and relatively constant rate of opening during the normal operation of the bridge, inertial effects were assumed to be small, and the key dynamic feature of the bridge behavior was the vibration about some changing static deflection. Estimations of the structure's natural frequencies were ascertained by performing a dynamic modal analysis of the structure. Figure 2.9 illustrates an idealized dynamic model. The model exhibited two rotational degrees of freedom, θ_1 and θ_2, representing rotation about the counterweight trunnion and heel trunnion, respectively. The leaf and counterweight masses were lumped at the

appropriate C.G. locations, and all members were considered rigid except for the counterweight links, operating struts, and the drive shafts, which were represented as springs. The counterweight links and operating struts were modeled as linear, axial springs, and the drive shafts were modeled as linear, torsional springs. The spring representing the operating struts was modeled in series with the spring representing the drive shafts.

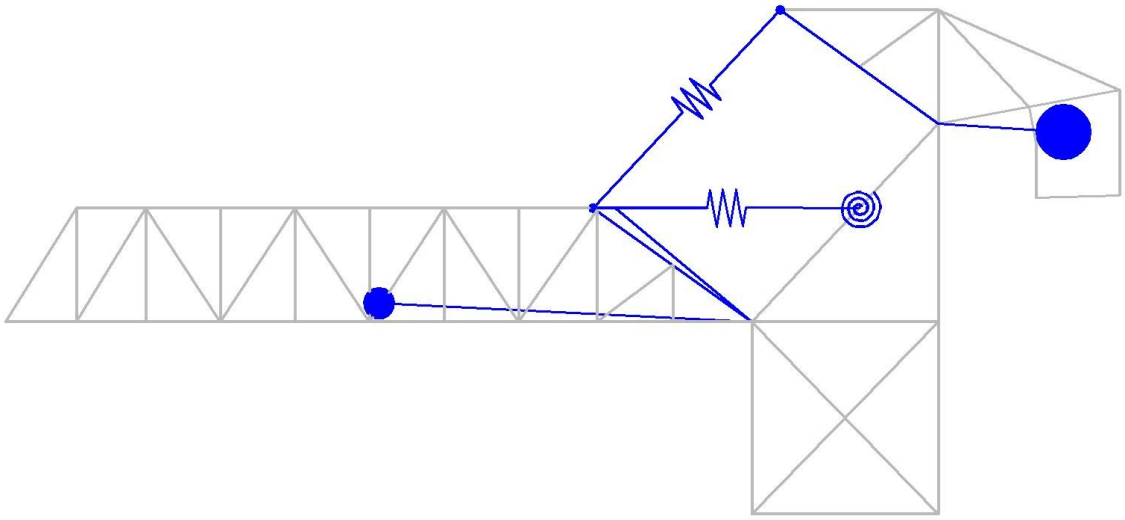

Figure 2.9: Idealized Model for Dynamic Analysis

The full analysis of the two DOF system is given in Appendix B. The resulting equations of motion are given in matrix format as

$$\begin{bmatrix} I_{\mathrm{CWT}} & 0 \\ 0 & I_{\mathrm{LF}} \end{bmatrix} \begin{Bmatrix} \ddot{\theta}_1 \\ \ddot{\theta}_2 \end{Bmatrix} - \begin{bmatrix} C_{\mathrm{CWT}} + C_{\mathrm{LK}} & -C_{\mathrm{LK}} \\ -C_{\mathrm{LK2}} & C_{\mathrm{ST}} + C_{\mathrm{LK2}} - C_{\mathrm{LF}} \end{bmatrix} \begin{Bmatrix} \theta_1 \\ \theta_2 \end{Bmatrix} = \begin{bmatrix} C_{\mathrm{CWTC}} \\ -C_{\mathrm{LF2}} \end{bmatrix} \qquad (2.5)$$

The system's natural frequencies may be calculated by solving the following eigenvalue problem

$$\left| \begin{bmatrix} C_{\mathrm{CWT}} + C_{\mathrm{LK}} & -C_{\mathrm{LK}} \\ -C_{\mathrm{LK2}} & C_{\mathrm{ST}} + C_{\mathrm{LK2}} - C_{\mathrm{LF}} \end{bmatrix} - \omega_{\mathrm{ni}}{}^2 \begin{bmatrix} I_{\mathrm{CWT}} & 0 \\ 0 & I_{\mathrm{LF}} \end{bmatrix} \right| = 0 \tag{2.6}$$

The frequency of vibration is related to the circular frequency by

$$f_{\mathrm{ni}} = \frac{\omega_{\mathrm{ni}}}{2\pi} \tag{2.7}$$

The natural frequencies calculated at 6 angles of opening are given in Table 2.5. The appropriate natural frequencies of idealized two dimensional models and the three dimensional SAP2000 models are given for comparison. Figure 2.10 shows a sample two dimensional SAP2000 model. This model includes all assumptions and parameters of the analysis used to develop Equations 2.6 and 2.7. Three dimensional natural frequency values are lower than the simplified analysis, which is consistent with the fact that more flexibility exists in the SAP2000 model. Natural frequencies were calculated in SAP2000 using a series of modal analyses; mass sources were defined from dead loads acting on the structure, and mass moments of inertia were adjusted to account for rigid body inertial effects (SAP2000 2011).

Table 2.5: Preliminary Dynamic Results

Angle (Deg.)	**f_{n1} (Hz)**			**f_{n2} (Hz)**		
	Eq. (2.7)	**SAP2000 2D**	**SAP2000 3D**	**Eq. (2.7)**	**SAP2000 2D**	**SAP2000 3D**
0	0.71	0.70	0.29	6.36	6.33	1.44
20	0.84	0.83	0.38	6.24	6.24	1.52
40	0.95	0.92	0.40	5.72	5.41	1.63
60	1.03	0.97	0.40	4.75	3.94	0.72
75	0.98	0.88	0.37	3.61	2.52	0.63

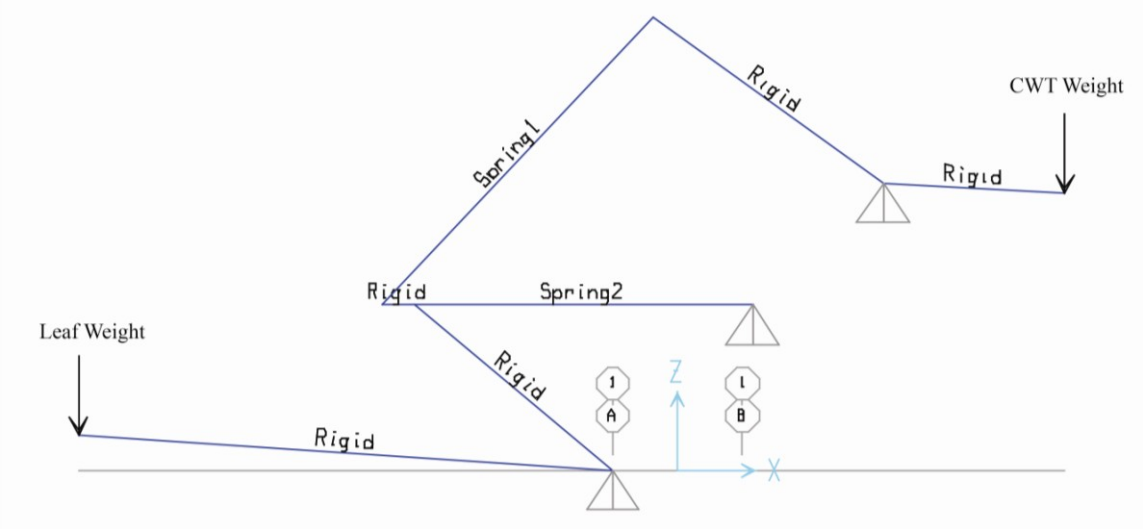

Figure 2.10: Idealized SAP2000 Model for Dynamic Analysis

2.4 Data Stream Design

Data stream design is a critical component of a structural impairment detection system. Any information necessary for the study or monitoring of a structural system should be contained within the data stream. For a structural impairment detection system, this information includes measurements of structural behavior that can be correlated to possible impairment conditions. The desired data stream determines the design of sensor networks to be installed on the structure. Transducer type, location, and number, along with data acquisition methods, were all key concerns to a successful experiment; these concerns were even more crucial for extended monitoring. While finite element models of a specific structure should be validated by field measurements, the models' results served as initial guidelines in determining possible structural impairments, modeling impairments, and identifying locations sensitive to modeled impairments.

2.4.1 Identification of Impairments

Stress reversals in counterweight truss members raise concerns for fatigue in those members (Frýba 1996, Wilson 1948). Using SAP2000 models, analyses of the bridge for six angles of opening were performed. The maximum stress ranges for members experiencing stress reversals or changes in stress in the tensile range were calculated from axial, in-plane bending and out-of-plane bending. The maximum stress ranges in 44 members, including counterweight truss members, bracing members, and the counterweight links, were identified as possible locations of fatigue. These locations of concern compare favorably to those areas considered vulnerable by BNSF engineers and those reporting previous bascule bridge failures (Wilson 1948, Graydon 1949).

2.4.2 Structural Impairment Modeling

With locations of fatigue concern identified, impairment at these locations was simulated through a reduction of cross-sectional member properties. Small (~0.1 inch) subdivisions at each of the 44 locations of concern found in Section 2.4.1 were incorporated in the SAP2000 models. Figure 2.11 illustrates a reduced section member inserted into a frame element. Impairment was simulated by reducing the cross-sectional properties (area, second moment of area, torsional constant) of each 0.1 inch reduced section member. With possible fatigue locations identified and reduced section members placed in the appropriate counterweight truss members, an automated MATLAB routine was established to systematically vary the cross-sectional properties in the appropriate counterweight truss members. The MATLAB routine produced SAP2000 input files and executed SAP2000 for each case of reduced section properties (MATLAB 2011, SAP2000 2011). Analyses were carried out for six angles of opening, 44 structural members, and two values of reduced section properties (one simulating a partial cross-sectional reduction and one simulating a full cross-sectional reduction). The total number of analyses performed (including the six undamaged cases) was 534.

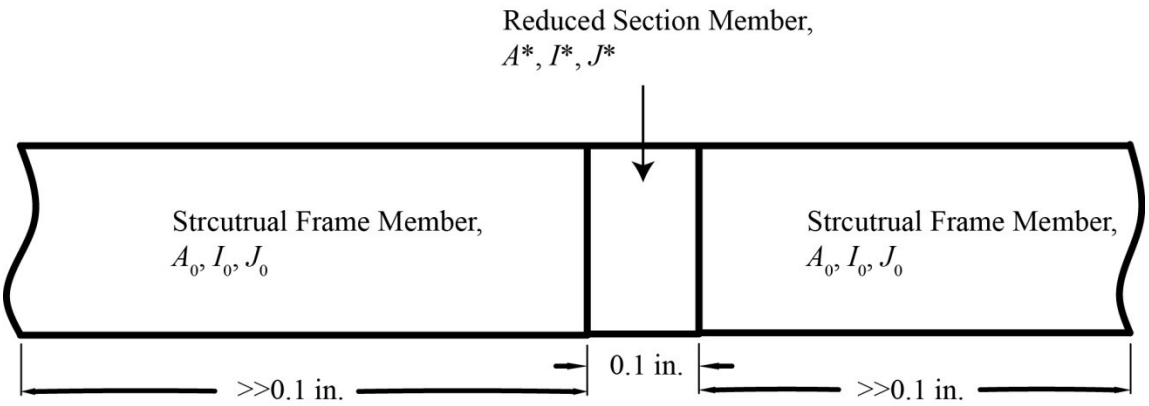

Figure 2.11: Reduced Section Member for Use in SAP2000 Analyses

2.4.3 Identification of Locations Sensitive to Structural Impairments

Locations that provide optimal impairment detection data streams exist on areas of the counterweight truss most sensitive to structural changes. The 44 locations with maximum stress ranges were logical points to examine, as they have shown sensitivity to the structural change of the bridge opening. For this reason, the stresses at each of the 44 reduced section members for each of the damaged analyses were examined and compared to the stresses in the 44 reduced section members for the corresponding undamaged results. The percent differences in change between stresses for the damaged and undamaged results were calculated for each reduced section member. The 44 locations were then ranked based on percent difference in stress range for damaged and undamaged cases. Specifically, regions that experience high stress/strain changes due to modeled impairments in other locations were selected for monitoring. Bracing members showed high sensitivity to the impairments of counterweight truss members. Sensor locations sensitive to modeled impairment are indicated by a red "X" in Figure 2.12.

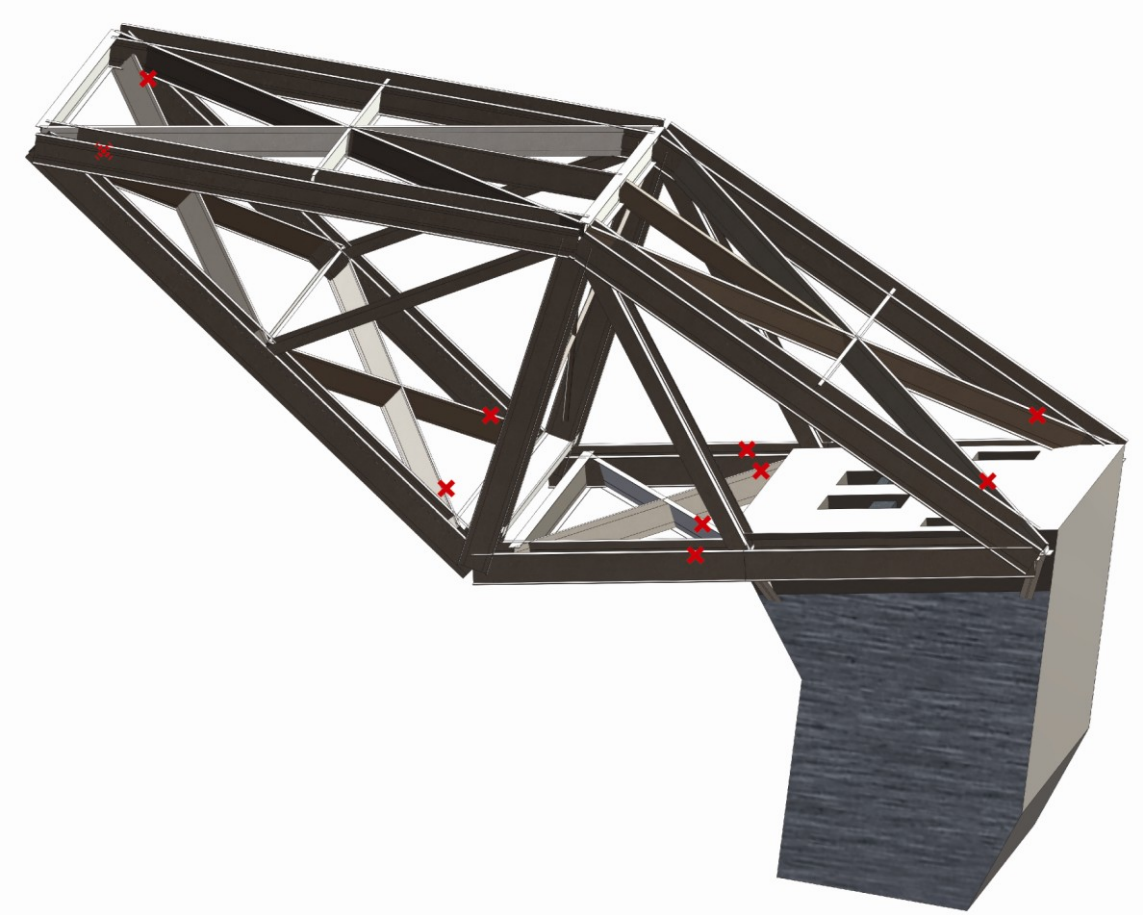

Figure 2.12: Optimal Sensor Locations Based on SAP2000 Analyses

The analyses described in Section 2.4 allowed for the systematic determination of specific data streams that contain information about impairment sensitive structural behavior. Data streams were created to serve as patterns to be used in the training of neural impairment detection algorithms.

2.5 Sub-Modeling of a Counterweight Truss in ABAQUS

Both locations of maximum stress range and locations of highest sensitivity were determined using analyses performed in SAP2000 and described in Section 2.4. While

SAP2000 was well suited for global locations of likely impairments and sensitive measurements, a more detailed finite element analysis was performed to improve key areas of the research project. A refined sub-model of the counterweight truss created opportunities to: 1) develop better estimates of counterweight truss member stresses, and 2) incorporate refined impairment scenarios.

2.5.1 Sub-Model Motivation and Definition

The complex interaction between embedded/partially embedded counterweight truss components and the concrete counterweight is difficult to capture in a finite element analysis. Counterweight truss members on the Salmon Bay Bridge are laced, built up sections that frame into the counterweight in complicated, and sometimes unknown, ways. Stresses occurring in the main chords of the counterweight truss are of particular interest, as failures of these chords have occurred and were documented in Chapter I. Sub-models of the counterweight truss and reinforced concrete counterweight allowed for a more detailed examination of stress values that occur along the main chord of the counterweight truss.

Hypermesh was used to create the geometry and finite element definitions for the analyses (Hypermesh 2011). Figure 2.13 shows the three-dimensional counterweight frame sub-model which includes counterweight truss members, counterweight link members, and the reinforced concrete counterweight. The tower that supports the counterweight at 29 was replaced with pinned boundary conditions that prevent all translations and allow rotation in the plane of rotation (about the z axis). The counterweight links were essentially two force members as they were pinned at 13, and moment about the z axis was released at 30. The specification of these boundary conditions in Figure 2.14 allowed the omission of the supporting tower and leaf in the sub-model. Table 2.6 gives a summary of axial forces in counterweight truss members and compares them to the data given in Table 2.3.

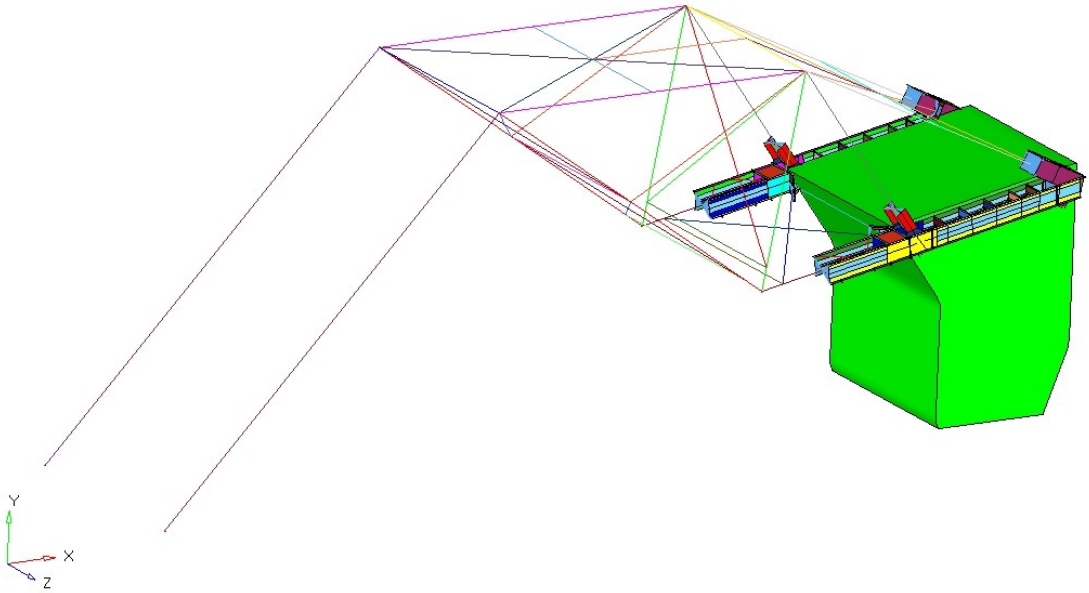

Figure 2.13: Sub-Model of Counterweight Frame

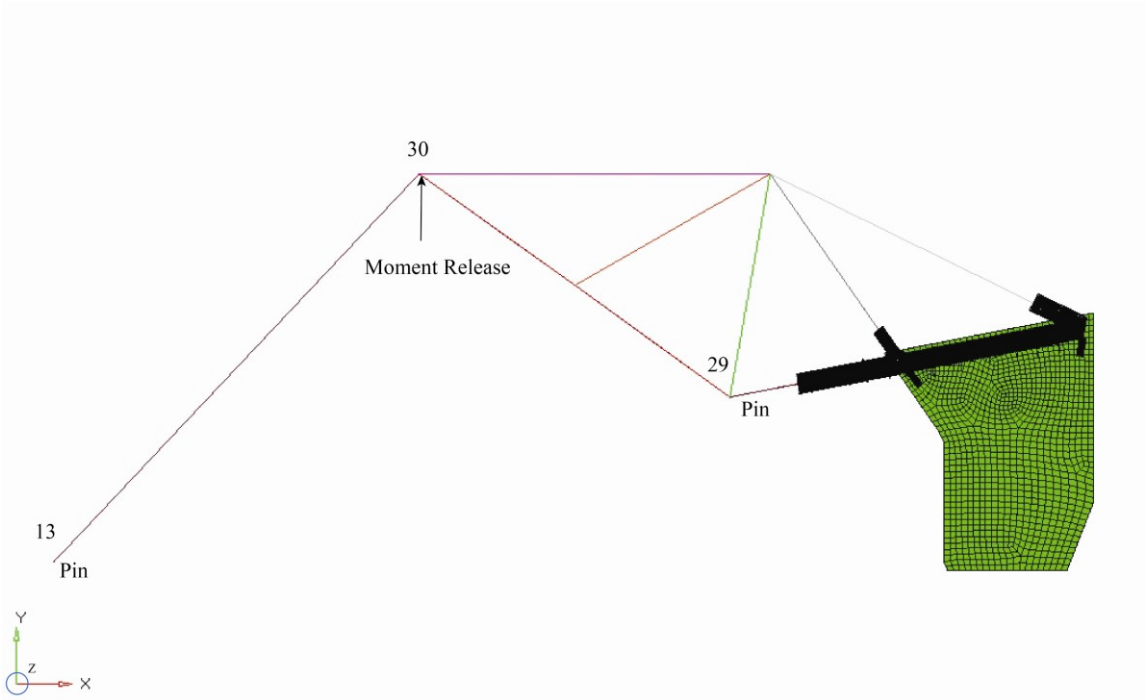

Figure 2.14: Sub-Model Boundary Conditions

Table 2.6: Summary and Comparison of Counterweight Frame Axial Forces

Member	Hand Statics (k)	SAP2000 3D Frame Model (k)	ABAQUS 3D Model (k)
Links	1139	1178	1146
29-31'	-1537	-1539	-1517
30-31'	-1518	-1514	-1489
30-31	2014	1957	1910
31-32	1549	1510	1469
33-32	-1417	-1700	-1553
29-33	-1825	-1840	-1797
29-31	-1342	-1389	-1333
31-33	704	715	696
31'-31	18	28	27

Modeling parameters such as geometry, weights, densities, and centers of gravity in the ABAQUS sub-model mimic those of the SAP2000 model. Again, six static models represent the varying angles of opening of the bridge at 0, 20, 40, 60, 75, and 82.5 degrees. As in the SAP2000 analyses, all ABAQUS analyses were linear elastic.

2.5.2 Sub-Model Details

The increased detail of the ABAQUS sub-model included the refinement of the main chord members, detailed connections to the counterweight, and modeling the full concrete counterweight. When considering main chord stresses, the benefit of ABAQUS over SAP2000 is the capability of modeling structural members in more detail as a series of shells that comprise the structural shape. Figure 2.15 shows a main chord of the counterweight truss and joint 33E that were meshed in Hypermesh. The cross section, tie plates, and connecting gusset plates were modeled with four node, linear, reduced-integration shell elements. The designation of one such element type in ABAQUS is S4R5 (ABAQUS 2011).

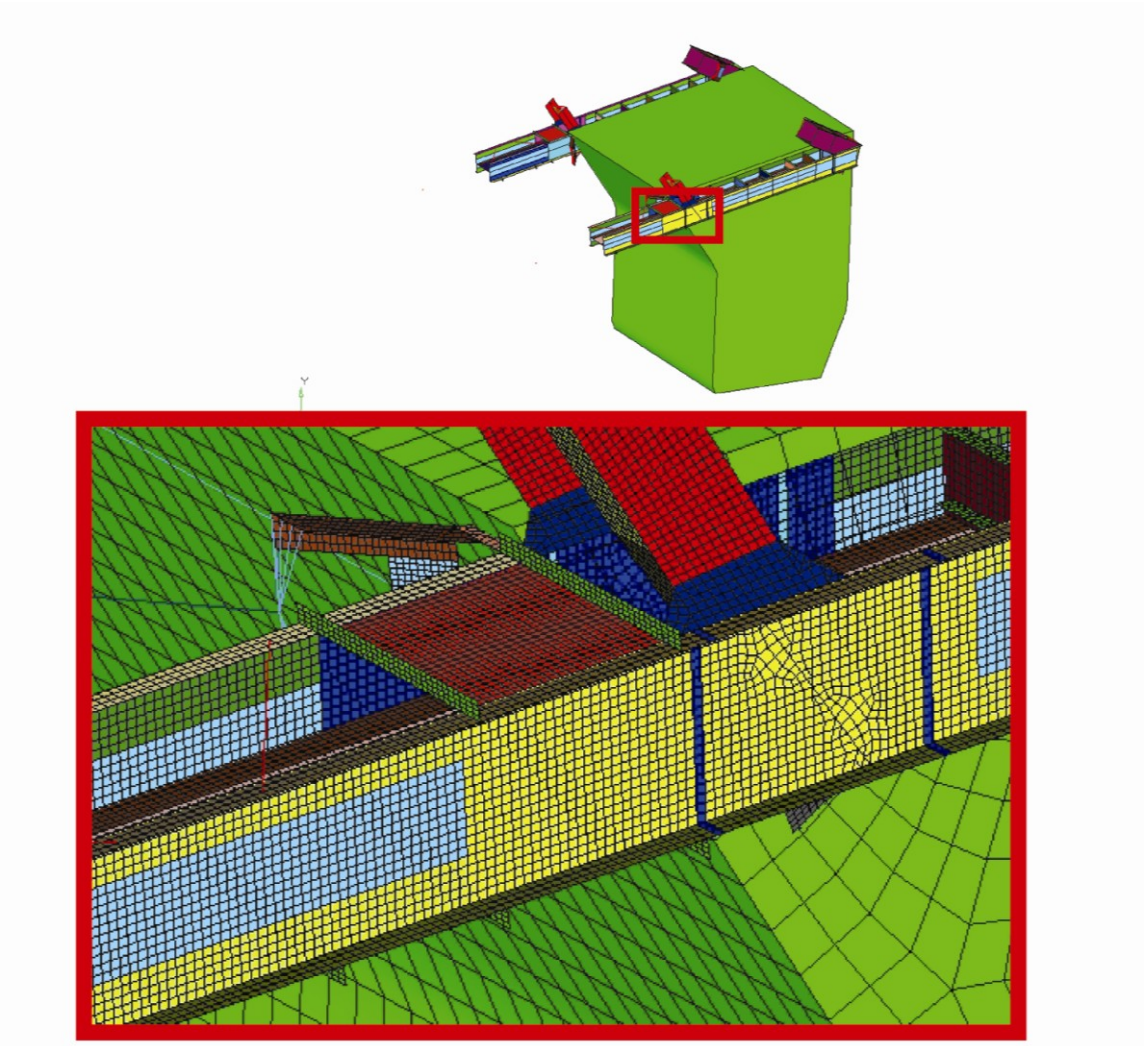

Figure 2.15: Detailed Modeling of Main Chord and Joint 33E with Shell Elements

In addition to the main chords of the counterweight truss, all counterweight truss members framing into the concrete counterweight were modeled with shell elements at their connection points. The portion consisting of shells was limited to a St. Venant distance away from the center of the joint. The remaining portions of these frame members were modeled as two node, linear frame elements indicated by B31 designation in ABAQUS. Continuity of degrees of freedom (both translational and rotational) was ensured by applying rigid constraints (BEAM constraints in ABAQUS) to the beam

node and all shell nodes in the cross section at the beam/shell interface. Figure 2.16 displays one of the beam/shell interfaces; the rigid constraints appear as blue lines. Counterweight truss members not directly framing into the concrete were modeled with B31 frame elements.

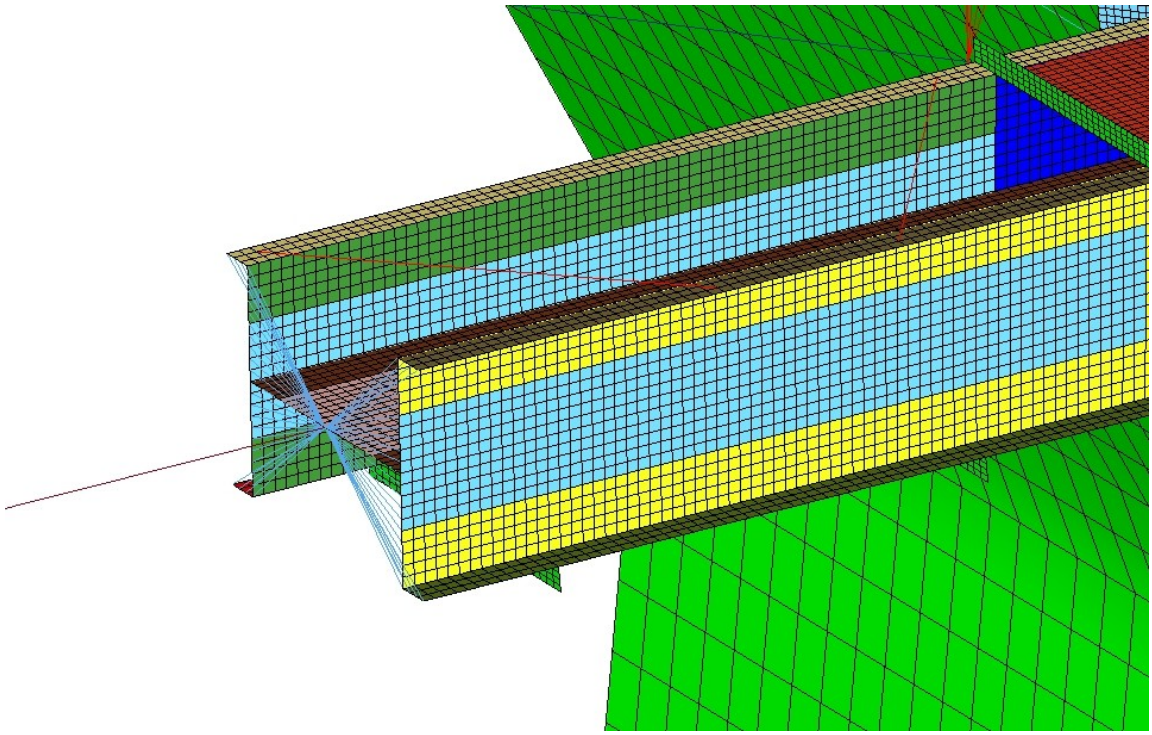

Figure 2.16: Beam-Shell Interface on Main Chord

A second desired improvement to the structural model was a more realistic model of the concrete counterweight. The concrete counterweight was modeled as an elastic solid consisting of eight noded, linear brick elements (C3D8 elements in ABAQUS). After preliminary modeling with SAP2000, the attachment of the counterweight to the counterweight frame became a concern since the complete, as-built details of the attachment were unknown. The concrete counterweight solid elements are

attached to the counterweight frame using the ABAQUS keyword *EMBEDED ELEMENT. Essentially, all translational DOF of frame elements within the solid concrete elements are constrained to the DOF of the nearest concrete solid element. Only embedded portions of the counterweight frame were attached to the concrete solid. Figure 2.17 depicts the counterweight model with and without visible solid concrete elements. The embedded steel frame was modeled with B31 elements.

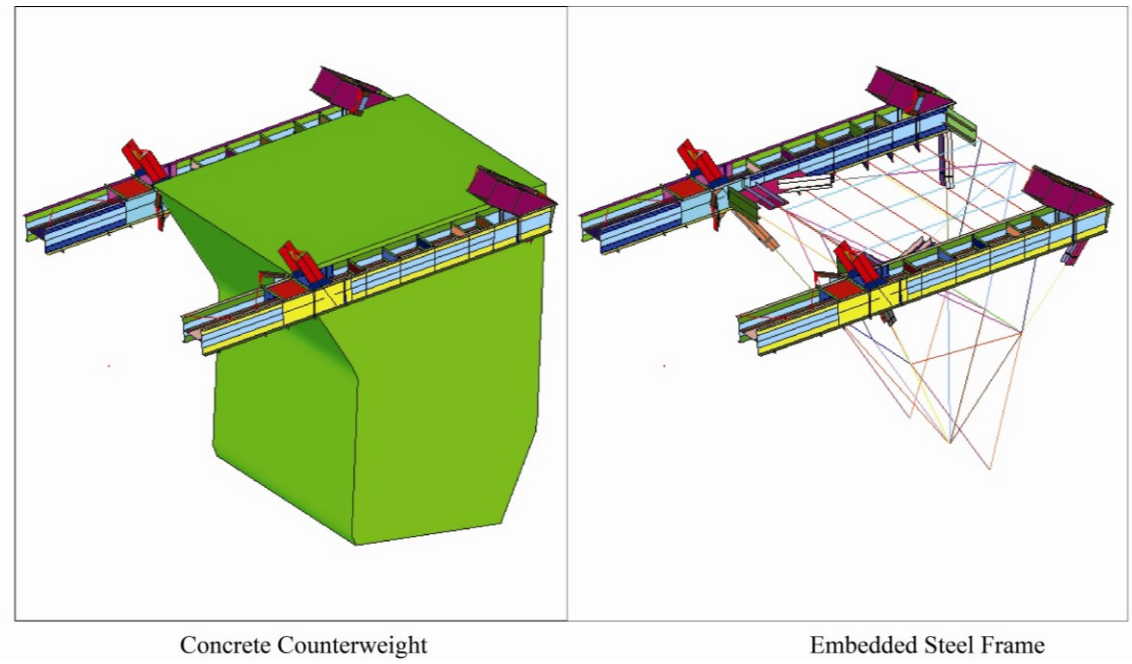

Figure 2.17: Illustrative Mesh of Concrete Counterweight and Embedded Steel Frame

2.5.3 Impairment Modeling in ABAQUS

Modeling impairment scenarios in SAP2000 and analyzing resulting data streams led to an instrumentation program likely to detect changes in the structural behavior of the Salmon Bay Bridge. Impairments modeled in SAP2000 were restricted to the reduction of section properties at specific locations. The refined structural model in ABAQUS presented an opportunity to examine other methods of modeling impairments.

Figure 2.18 displays an alternative method of representing section loss to that of section 2.4.2. Rather than reducing the numerical values of a short section of frame element to represent section loss, the individual elements belonging to a member consisting of shell elements were deleted. Elimination of the vertical column of shell elements was intended to represent a cracked portion of the main chord. This approach offered more flexibility and control over the type and severity of the impairment.

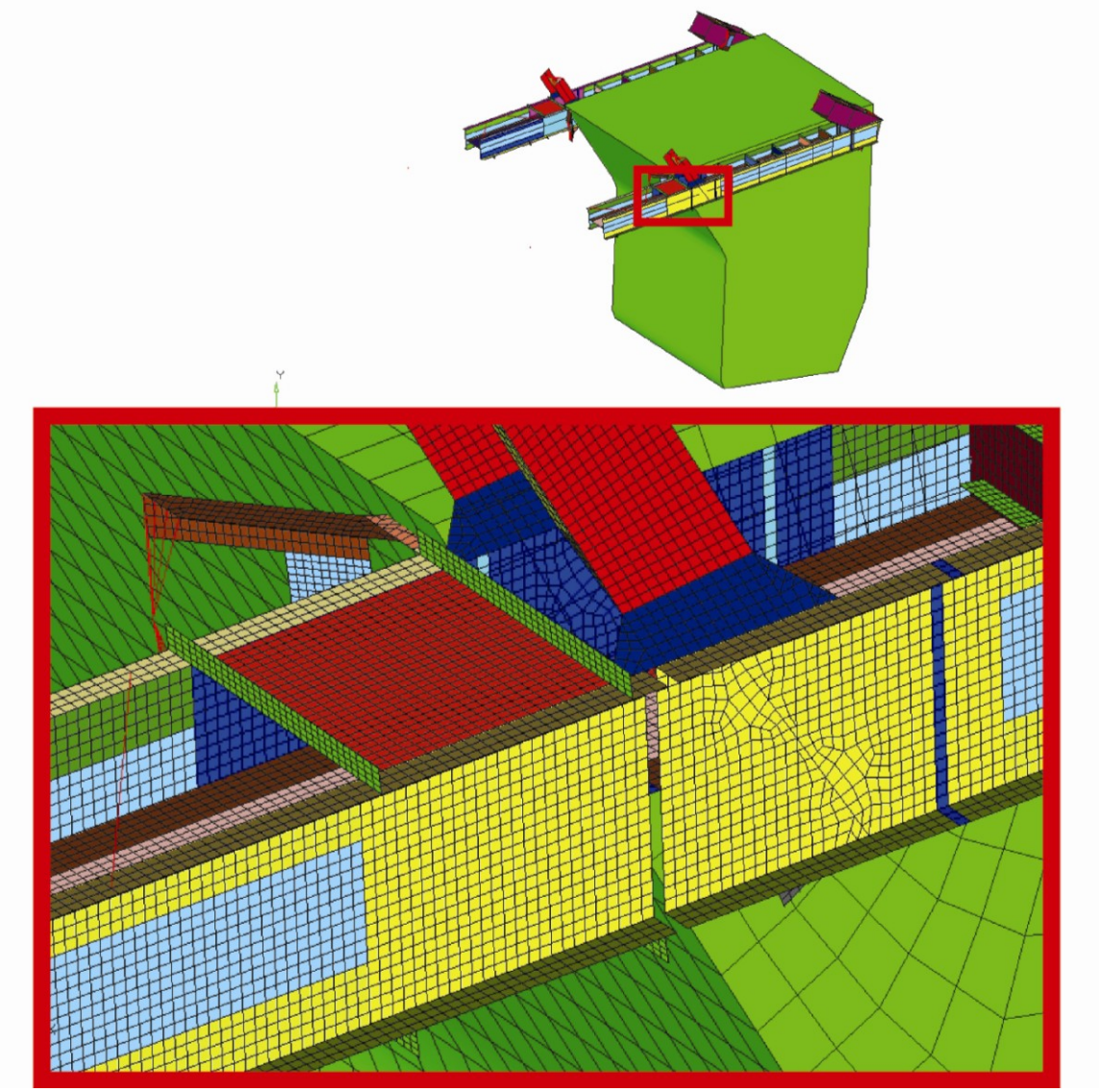

Figure 2.18: Sub-Model Impairment

In addition to more realistic section loss impairment modeling, the inclusion of solid elements representing the counterweight enabled the investigation of concrete deterioration impairments. Solid element deletion around exterior and interior frame concrete connections represented a loss of interaction between the concrete and steel.

2.6 Competitive Neural Networks

One approach to using neural networks for damage or impairment detection is the use of a competitive array of neural networks (Hyland and Fry 1999). Several neural networks competing for an opportunity to train on input data is one method of improving the efficiency and effectiveness of neural networks.

2.6.1 General Competitive Array Architecture

In a competitive array of neural networks, several neural networks were initialized with varying architectures (i.e. number of neurons, number of layers, etc.). As shown in Figure 2.19, an input (X_i) was presented to a series of untrained neural networks which simulated outputs (Y_i). The comparator examined the simulated outputs and the target output (Y_{TARGET}), identified the neural network with the best performance, and allowed only that network to train on the input by adjusting its synaptic weights.

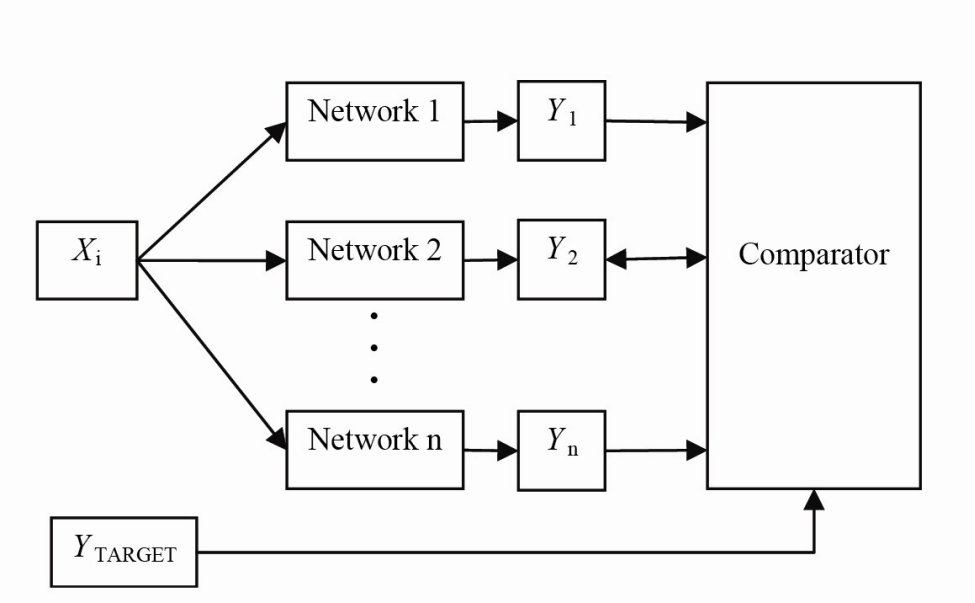

Figure 2.19: Competitive Neural Networks: Training

In Figure 2.19, Network 2 performed best and was permitted to backpropagate error (indicated by the double headed arrow) and train on X_i. No other networks were allowed to adjust their weights. The comparator, which made the determination of which competing network was worthy of receiving the input, is also a neural network that learned a relationship between the input (X_i) and the network with the best performance for that input type. The process was repeated with other input/output training pairs. Competing networks are advantageous because they can specialize themselves to learn only certain types of input pairs. The division of input groups was based solely on the performance of competing neural networks.

In simulation mode, a new input corresponding to an unknown output was presented to the trained comparator. The comparator decided which network will be best able to simulate the input, and an output was produced. Figure 2.20 illustrates the simulation mode. Appendix C presents an example that illustrates the effectiveness of competitive arrays of neural networks.

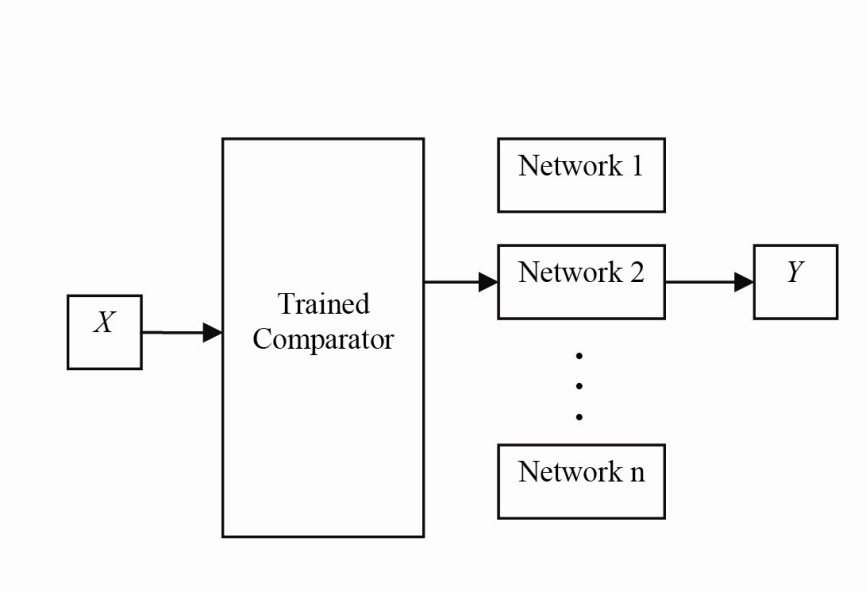

Figure 2.20: Competitive Neural Networks: Simulation

2.6.2 Format of Data Streams for Quasi Static Competitive Neural Network Development

Different structural systems have different loading conditions, types of structural responses, and different critical impairments. Accordingly, diverse tools of analysis, design, and measurement are necessary for the evaluation of specific structures. The frequency in which a structure is evaluated depends on events that produce appropriate diagnostic data streams and the data acquisition sampling rate. When examining stress ranges in counterweight truss members of a bascule bridge, events that produce data streams of diagnostic value are openings and closings of the bridge. With a sampling rate of several measurements per second, an evaluation of the bridge, consisting of structural impairment detection, may take place at multiple intervals during an opening or closing. At a given angle of opening, stresses calculated from strain gage measurements can be evaluated to determine the operational condition of the structure. The neural algorithm for this type of evaluation consisted of an array of static neural networks for each

predetermined angle of opening. Such an algorithm has been termed quasi static because arrays of static neural networks make independent evaluations at intervals of opening. For an opening event, evaluations occur at several angles of opening using static neural assessments. This method produces a series of assessments that may indicate changes in structural behavior within the timeframe of an opening event. Figure 2.21 illustrates input format and output produced by a quasi-static, competitive neural algorithm for one possible input data stream consisting of 8 evaluations at 8 angles of opening.

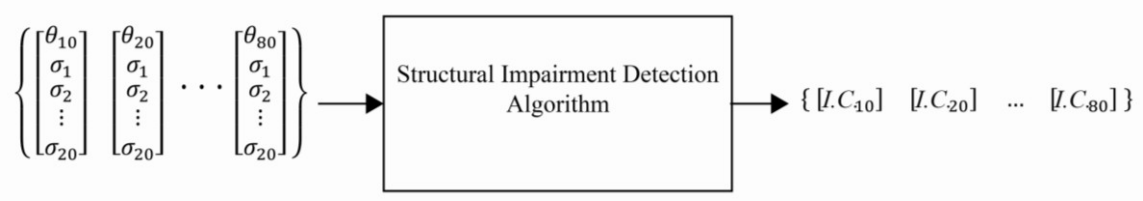

Figure 2.21: Data Format for a Neural Structural Impairment Detection Algorithm

Eight arrays of static neural networks interrogated data streams at 10 degree increments from 10 to 80 degrees. Each array contains networks that evaluate a column vector of stress values from 20 strain gage locations. The output consists of an operational state for each angle of opening. Raw output from the neural network algorithm takes the form of a [1 x *N*] vector in a one-of-*c* format where *N* is the number of possible classification. One-of-*c* coding describes the i^{th} impairment case as a [*N* x 1] vector with the i^{th} value of the vector containing unity and all other entries containing zeroes. Ultimately, the raw output vector is examined to determine which operation condition the bridge most closely resembles.

2.6.3 Operational Details of Quasi Static Neural Algorithms

After determining the appropriate data stream format, the operational details of the quasi static algorithm were developed. Each of the eight diagnostic arrays

responsible for each 10 degree angles of opening contained 20 static, single layer, backpropagation neural networks of a randomly assigned number of neurons. The individual networks were initialized using the *newff* command in MATLAB's Neural Network Toolbox (MATLAB 2011). Each input training vector was presented to each of the 20 untrained, backpropagation neural networks. The comparator evaluated the responses of each untrained network and assigned the input vector to the winning network. The winning network was allowed to train on the current input training vector. The comparator determined the winning network by determining which produced vector was most similar to the target vector. This determination was made by examining the dot product of normalized, untrained network responses and the target response. Target vectors representing impairment classifications consisted of one-of-*c* coding and were orthogonal unit vectors. Untrained network responses were normalized into unit vectors. The normalized unit vector most resembling the target unit vector identified the winning network. Dot products of the untrained, normalized unit vectors and the target vector were calculated, and result closest to unity indicated the simulated vector most similar to the target vector. This approach utilized the fact that orthogonal unit vectors follow the relationship

$$e_{\mathrm{i}} e_{\mathrm{j}} = \delta_{\mathrm{ij}} \tag{2.8}$$

where e_{i} and e_{j} are unit vectors and δ_{ij} is the Kronecker delta defined by

$$\delta_{\mathrm{ij}} = \begin{cases} 1 & i = j \\ 0 & i \neq j \end{cases} \tag{2.9}$$

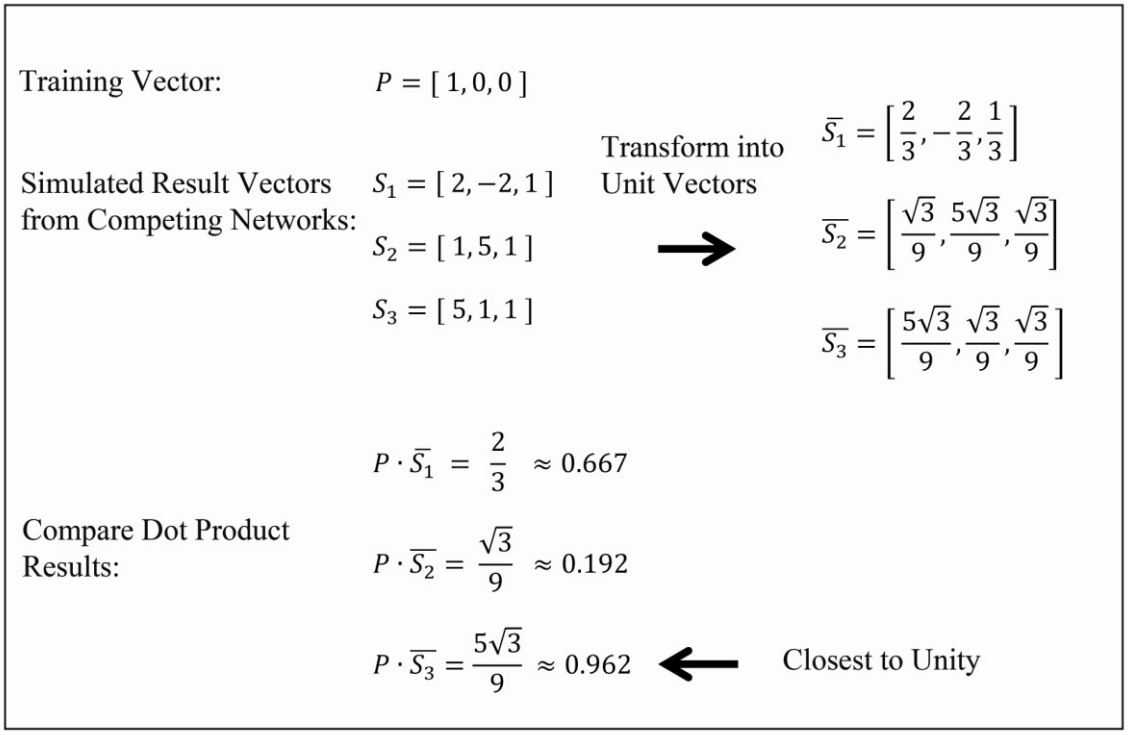

Figure 2.22: Illustration of Dot Product Evaluation for Neural Comparator

Figure 2.22 illustrates the concept by examining example output vectors produced by three competing neural networks and a target vector. The dot product resulting from the third normalized unit vector and the target vector is closest to unity, and thus the net producing the third output vector is permitted to adjust its synaptic weights. Note that other common measures of error, such as mean-squared error, would not produce the same winning network. The first vector has the lowest mean-squared error.

A neural image is produced after all of the winning diagnostic nets in each array are trained on input vectors, and the comparators assign neural networks from each array to the input vectors. This image contains winning diagnostic network indices for each input vector. Arrays are competitively trained multiple times on all input vectors until a stable neural image is produced. Then comparators are trained to recreate these neural

images by associating input vectors with winning neural networks. Successful architectures for comparator neural networks are backpropagation (*newff*) and probabilistic (*newpnn*) neural networks (MATLAB 2011). Probabilistic neural networks require no iterative training and are designed to sort training input vectors into groups for each winning net.

This process was repeated for each of the eight arrays. After training, each diagnostic array was responsible for correlating stress values at a particular angle of opening with specific impairment conditions. In field implementation, the stresses and opening angles would result from measurements taken from the bridge. Initial verifications of the system included input stresses from training cases corrupted with random noise. Values of +/- 5-15% of the maximum sensor stress were added to training signals to create validation data from training data. Figure 2.23 illustrates the simulation of a neural impairment detection algorithm for one angle of opening. An input vector of stresses and a corresponding angle of opening is analyzed by the neural structural impairment detection system. The angle of opening determines the active diagnostic array. The specific array's comparator analyzes the stresses and determines the index of the previously trained neural network (i.e. its neural image, *N.I.*) that is suited to make the determination of possible impairment. The input stresses are presented to the appropriate diagnostic neural network and the resulting impairment condition (*I.C.*) is produced.

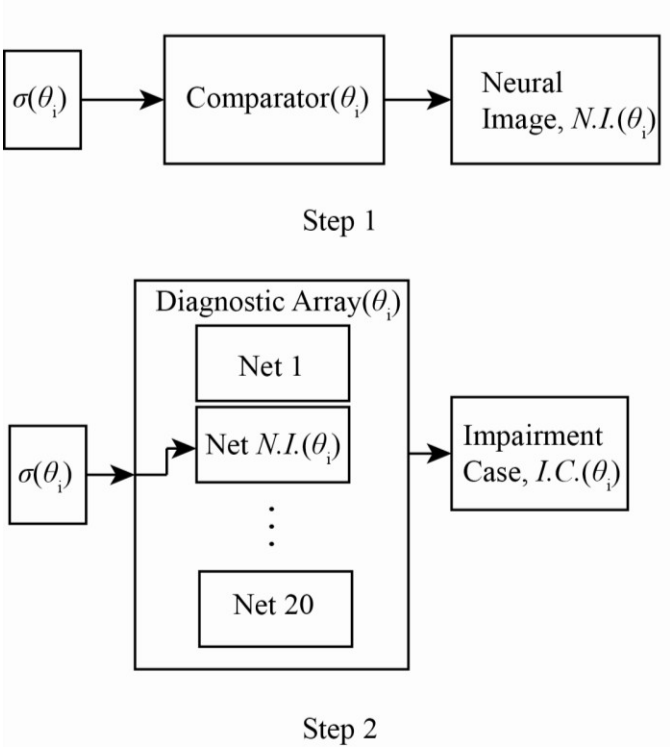

Figure 2.23: Illustration of Neural Structural Impairment Detection Algorithm

Data streams from both SAP2000 impairment scenarios and ABAQUS impairment scenarios were used to train competitive neural networks. Table 2.7 is a matrix of impairments modeled in both SAP2000 and ABAQUS. For SAP2000, 17 damage cases representing full section loss at critical counterweight truss sections were examined. ABAQUS models represented 17 damage cases including partial and full section loss at critical sections and broken members embedded in concrete.

Table 2.7: Matrix of Impairment Scenarios

Impairment Location	**SAP2000**		**ABAQUS**	
	Modeled	**I.C.**	**Modeled**	**I.C.**
Undamaged	x	1	x	1
29-33E, 33 E	x	8	x	2,3
29-33W, 33 W	x	9	x	6,7
33-32E, 33 E	x	16	x	4,5
33-32W, 33 W	x	17	x	8,9
33-32E, 32 E			x	10,11
33-32W, 32 W			x	12,13
East Link, 13 E	x	6		
West Link, 13 W	x	7		
30-31E, 31E	x	10		
30-31W, 31W	x	11		
31-32E, 32E	x	12		
31-32W, 32W	x	13		
31-33E, 33E	x	14		
31-33W, 33W	x	15		
32E,leg	x	2	x	16
32W, leg	x	3	x	17
33E, leg	x	4	x	14
33W, leg	x	5	x	15

CHAPTER III
EXPERIMENTAL PROCEDURES

3.1 Objectives and Methodology of Experimental Work

The analytical modeling methods described in Chapter II resulted in: 1) data streams for developing competitive, neural impairment detection algorithms, and 2) an instrumentation program for experimental measurements of a bascule bridge. Chapter III focuses on the implementation of an instrumentation program for the Salmon Bay Bridge testbed. Instrumentation of the bridge produced key information in the study of the structure and provided a testbed with which to implement and validate the structural impairment detection system. The methodology developed for experimental work on the testbed structure is as follows:

1. Refine transducer selection and layout via site visits and correspondence with BNSF engineers,
2. Design a data acquisition system and develop a rugged, reliable transducer schedule for installation and long-term on the Salmon Bay Bridge testbed,
3. Install and maintain transducers and data acquisition equipment on the Salmon Bay Bridge testbed, and
4. Implement a structural impairment detection system on the Salmon Bay Bridge.

3.2 Instrumentation Selection and Design

Instrumentation programs vary according to the needs of behavioral assessment and the structure being evaluated. Evaluation of the Salmon Bay Bridge testbed focused primarily on the behavior of the counterweight truss members. Specifically, counterweight truss members were examined in order to ascertain any abnormal behavior caused by impairments on counterweight frame members or impairment of concrete-steel interaction at counterweight connections. Strain gages, inclinometers, quadrature encoders, and a weather station provided the diagnostic data streams used in assessing the operational state of counterweight truss members.

3.2.1 Refinement of Measurement Areas

While the detailed analyses described in Chapter II suggested an optimal array of measurement locations for purely diagnostic considerations, refinements to the array were made prior to installation. The final locations were chosen considering the safety of installation crews, accessibility, and the preference of BNSF engineers. Preliminary analyses from Chapter II suggested that bracing members might provide the best diagnostic data used to classify the structure's behavior; thus several bracing members of the counterweight truss were chosen for instrumentation. In addition to instrumenting areas sensitive to changes in structural behavior, BNSF engineers were interested in monitoring behavior at regions of high stress. For this reason, the main chords of the counterweight truss were also selected for extensive measurement. In addition to areas of high stress ranges, several locations corresponding to locations examined in an instrumentation and analysis conducted in 1952 were included in the instrumentation program. These locations provided an opportunity to corroborate and compare results for the main chords of the counterweight truss after almost 6 decades of operation (BNSF 1952). A combination of detailed structural models, input from field engineers, and independent instrumentation results from 1952 resulted in a refined, complete transducer placement.

3.2.2 Primary Diagnostic Transducers

Structural impairments caused by the fatigue of counterweight truss members motivated the selection of strain range measurements as a function of the bridge's angle of opening as the primary measurement for the development of a structural impairment detection system. Two transducer types were required to observe the relationship of strain (and stress) as a function of angle. Strain gages located on counterweight truss members and clinometers mounted to the counterweight truss provided the primary structural data streams used in detecting and classifying structural impairments.

Structural members experiencing significant stress ranges are of great interest to structural engineers concerned about strength and fatigue resistance. While stress is a common indicator of structural behavior, it cannot be measured directly. Stress

estimations were calculated from strain measurements in the field. An effective method of obtaining strain ranges on structural members is through the use of electrical resistance strain gages. A wide range of strain gage parameters exist (types, orientations, etc.), and researchers should exercise care when designing a measurement setup for a particular problem. Two strain gages were installed at each measurement location on the counterweight truss. Gage pairs were installed 18-24 in. from tie plates at connections on the counterweight truss in the half bridge, perpendicular orientation shown schematically in Figure 3.1. Four pairs of strain gages were installed on main chord members and counterweight links, and one or two pairs of strain gages where installed on bracing members.

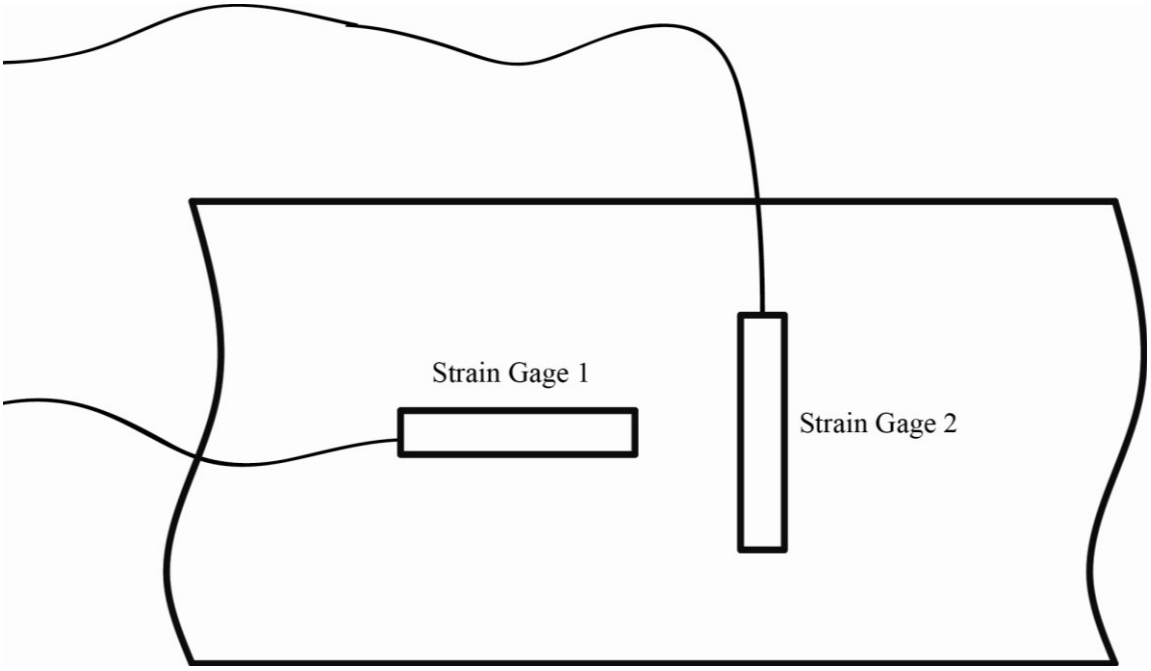

Figure 3.1: Half Bridge, Perpendicular Strain Gage Orientation

Weldable strain gages were utilized on the Salmon Bay Bridge for their durability, reliability, and relative ease of installation over traditional adhesive strain

gages. The gages were installed on counterweight members under load, and thus only changes in strain, not absolute strains, were measured.

In order to accurately relate strain ranges in counterweight truss members to the bridge's angle of opening, clinometers were installed to measure the absolute angle of opening on the Salmon Bay Bridge. Two clinometers were mounted under stairs located on the counterweight truss.

3.2.3 Auxiliary Transducers

In addition to counterweight truss strain gages and clinometers, three other transducer groups were included in the instrumentation program for the Salmon Bay Bridge. Full bridge strain gages on the drive shafts, quadrature encoders on the drive shafts, and a weather station provided redundancy and auxiliary measurements with which to evaluate the bridge and the primary data acquisition system.

A full bridge strain gage was installed on each of the east and west drive shafts. Full bridge strain gages oriented at a 45 degree inclination and installed on the drive shafts measured changes in strain which were related to torque values in the drive shafts. The torque measurements were extremely useful in refining values of component weights and centers of gravity. Figure 3.2 illustrates the installation location of drive shaft strain gages.

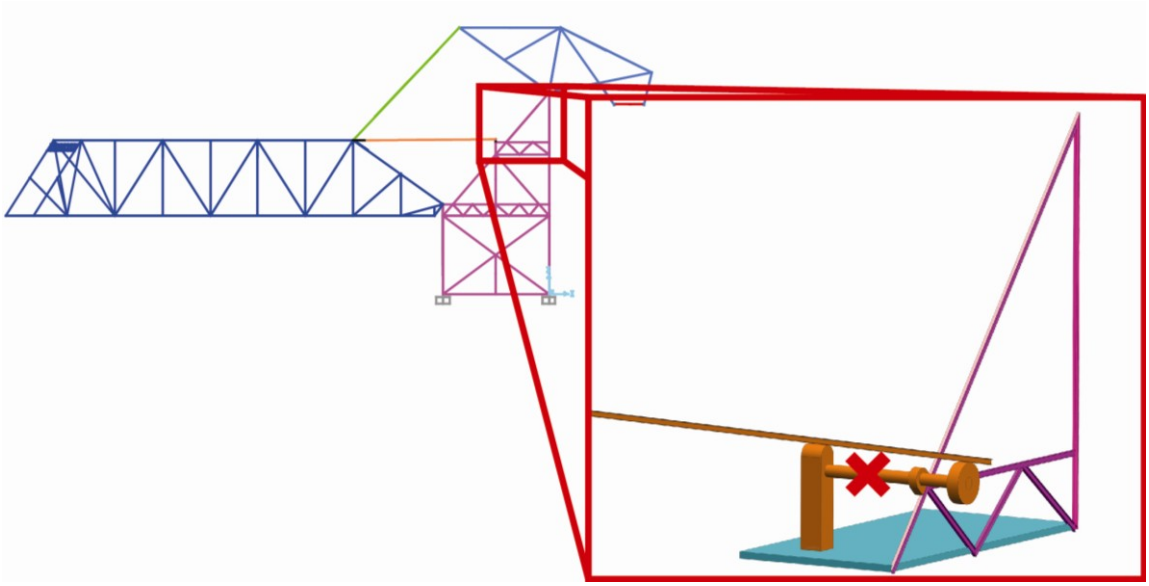

Figure 3.2: Location of Drive Shaft Strain Gages

Rotary quadrature encoder wheels were mounted as shown in Figure 3.3. The encoder wheels rotated with the shaft as it operated. Rotary quadrature encoders relate the number of physical rotations to counts produced by the transducer. The angle of opening of the bridge was related to the number of turns of the driveshaft (and counts transmitted by the encoders) and served as a redundant measurement of angle of opening.

Figure 3.3: Photograph of Drive Shaft Instrumentation

Finally, a weather station was installed to monitor environmental conditions such as temperature, wind speed, and rainfall at the testbed. Of its many capabilities, temperature measurement was the primary interest. Temperature changes can significantly affect measurements of strain. Sub-section 3.3.1 and Appendix D outline the steps taken to reduce the effect of temperature on strain measurements. The weather station installed at the testbed is a Davis Vantage Pro2.

3.2.4 Final Transducer Selection and Layout for Installation

Final decisions concerning transducer selection and placement incorporated: 1) results from finite element analyses to determine areas sensitive to changes in structural behavior, 2) requests from BNSF engineers to monitor areas of suspected large stress ranges, and 3) the accessibility of measurement locations that could be safely installed by BNSF work crews. Figure 3.4 shows the final counterweight transducer location

scheme on the Salmon Bay Bridge testbed. Clinometers and strain gages are represented by red “X” and green “O” shapes, respectively. The number of strain gage pairs is also indicated on Figure 3.5.

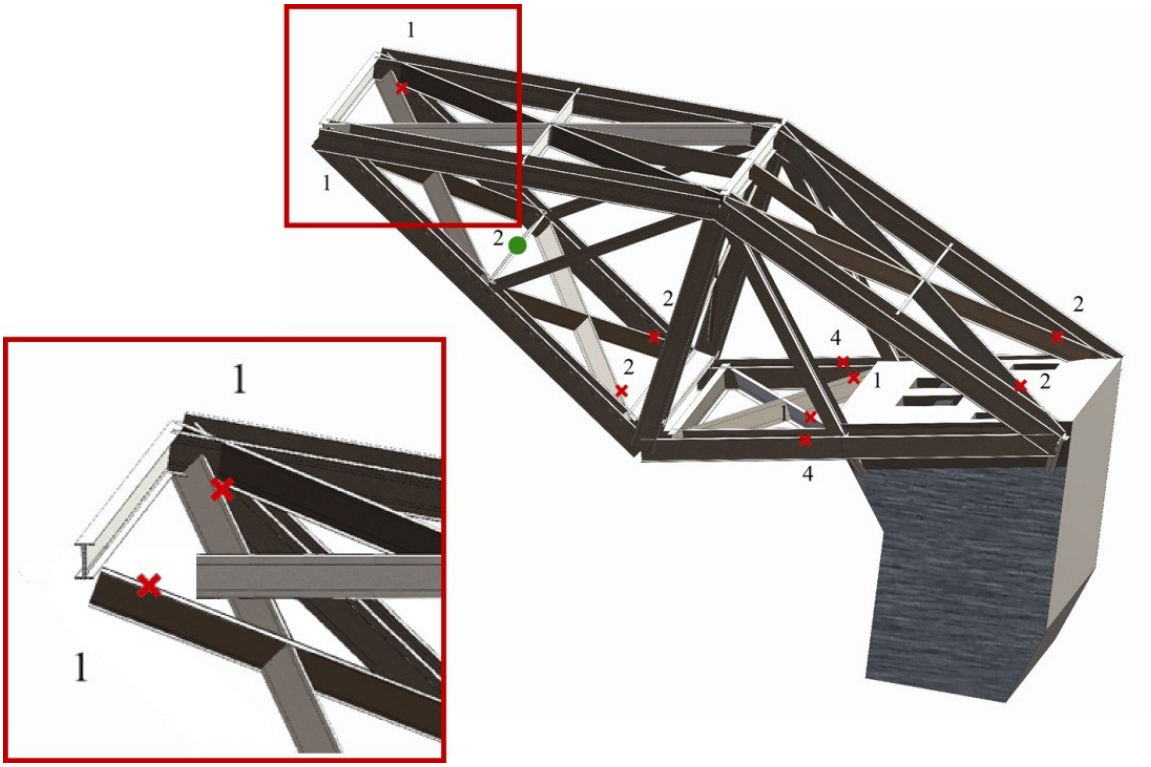

Figure 3.4: Final Counterweight Transducer Layout of SIDS Development

3.3 Data Acquisition Design

While high quality transducer selection was an important factor in ensuring successful data acquisition, the design of data acquisition components was paramount in the implementation of a long-term monitoring effort. The data acquisition design included the selection of data acquisition modules to receive signals from transducers, the design of specific transducer circuitry, and transducer data file management.

3.3.1 Data Acquisition Hardware

Figure 3.6 shows the data acquisition station at the Salmon Bay Bridge testbed. Several IOTech data acquisition models were used as receivers and processors of signals produced by transducers during measurements. The primary data acquisition module is the StrainBook/616 module on the bottom of the stack in Figure 3.5. The StrainBook/616 is attached directly to the data acquisition laptop and supports 8 channels of input (IOtech 2005). One StrainBook/616 also supports and synchronizes up to 7 additional expansion modules. Expansion modules at the testbed include 5 WBK16 modules and 1 WBK17 module. WBK16 modules support 8 bridge circuit strain gage channels, and WBK17 modules receive counter signals and support quadrature encoders (IOtech 2005). Each strain gage module contains bridge completion circuitry and analog to digital conversion. Data acquisition modules measure changes in voltage and relay voltage values to the data acquisition laptop. The laptop responsible for display, recording, and storage of transducer measurements is a Dell E6400 ATG research computer.

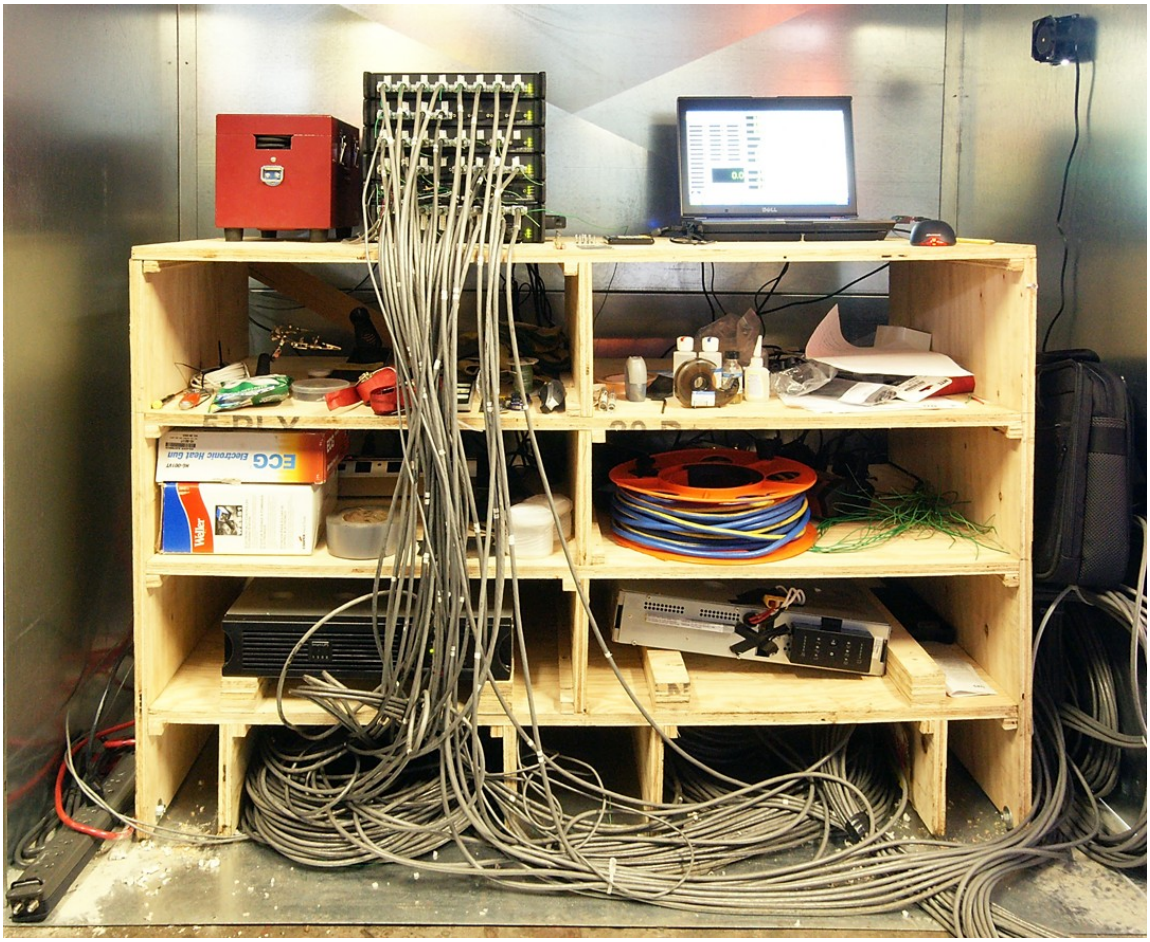

Figure 3.5: Photograph of Data Acquisition Equipment

3.3.2 Data Acquisition Software

The data acquisition software used on the Salmon Bay Bridge testbed is DASYLab Pro Version 11. DASYLab is a data acquisition program that uses a graphical, block/wire programming style to organize the input of signals coming from data acquisition modules as shown in Figure 3.6. Signals are imported into DASYLab as voltages and are then conditioned appropriately to display engineering quantities of interest (i.e., strain, stress, torque). Readings are displayed in engineering units, but all

signals are saved as voltage data streams and later converted to appropriate engineering units.

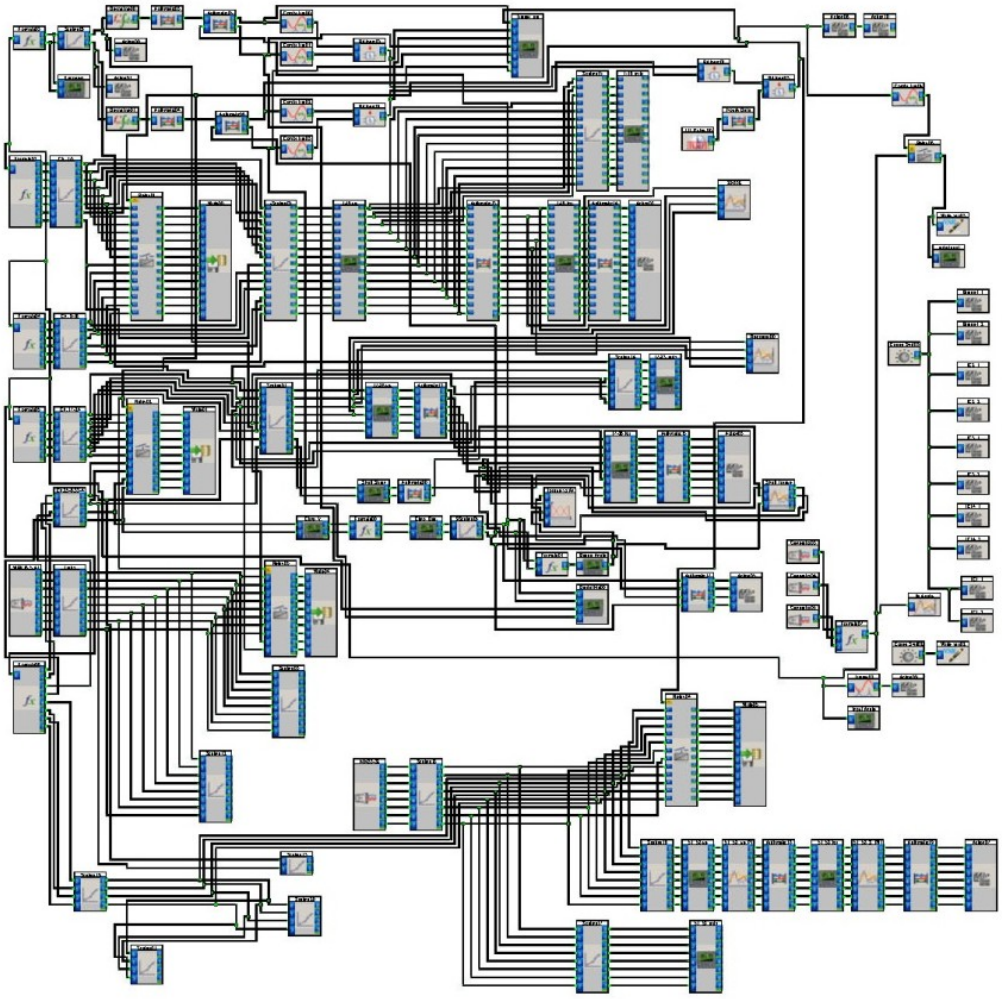

Figure 3.6: DASYLab Worksheet

Observed signals from transducers depend on the rate at which data is sampled. In Chapter II, preliminary dynamic evaluations produced natural frequencies of vibration of 1.03 Hz and 6.36 Hz for first and second modes, respectively. In order to avoid signal

destruction by aliasing, the sampling rate should be at least twice the expected signal frequency; such a sampling rate is called the Nyquist rate (Kamen and Heck 2000). Because the expected frequency of vibration was much lower than the sampling capabilities of the StrainBook/616 (125 kHz per channel), a sampling rate of 20 Hz was selected (IOTech 2005). This is approximately 3 times the estimated maximum frequency of vibration resulting from analytical models, and 1.5 times the Nyquist frequency.

Data from the bridge is constantly received and displayed on the data acquisition laptop, but data streams most relevant to structural impairment detection are produced only when the bridge is opening and closing. A trigger system was created to determine when the bridge was opening or closing, and data was recorded and written to text files for the duration of an opening or closing. The trigger activates when both drive shafts are rotating with a rate of 0.02 counts per second and the bridge's angle of opening is more than 1 degree. A pre-trigger and post-trigger of 5 and 20 seconds ensures that data immediately preceding and following an opening or closing of the bridge is captured.

3.3.3 Strain Measurement

Electrical resistance strain gages relate changes in voltage to changes in resistance, which are then related to changes in known gage length. This strain can be related to stress through Hooke's Law. Tiny variations in voltage due to small changes in resistance are accurately measured with a Wheatstone Bridge circuit. Figure 3.7 indicates the configuration of a typical Wheatstone bridge circuit.

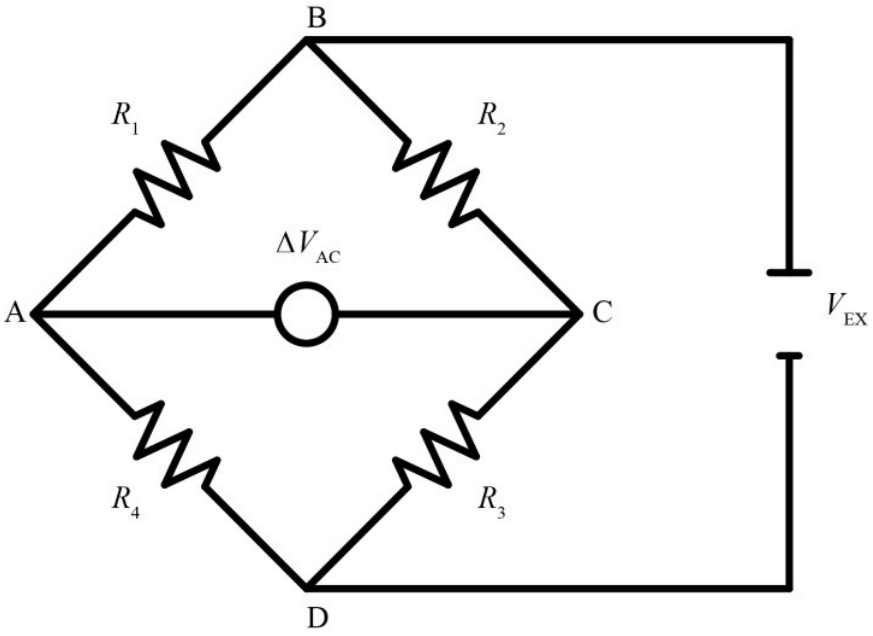

Figure 3.7: Wheatstone Bridge Circuit

The arms (1-4) of such a circuit consist of up to four strain gages; arms without active strain gages contain completion resistors. Strain gages used on the Salmon Bay Bridge are 120 Ω, TML AWC-88 strain gages shown in Figure 3.8. For strain measurements on counterweight truss members, half bridge, perpendicular strain ("T-Bone") configurations are used. This half bridge configuration compensates for changes in temperature and increases the sensitivity of the measurement by a factor of 1.29 over a single quarter bridge configuration.

Figure 3.8: Weldable Strain Gage Installed on Counterweight Truss Members

The linearized equation for axial strain as a function of measured output voltage for the half bridge T-Bone configuration is

$$\varepsilon = k_1 V_{OUT} \tag{3.1}$$

Where,

k_1 = -0.303998$\left(\frac{\text{in./in.}}{\text{V}}\right)$

Full bridge strain gages were used on drive shafts. 350 Ω Vishay CEA-250US-350 strain gages are specialized for torque measurements and are shown in Figure 3.9. Full bridge configurations are temperature compensated and 4 times more sensitive than a single gage.

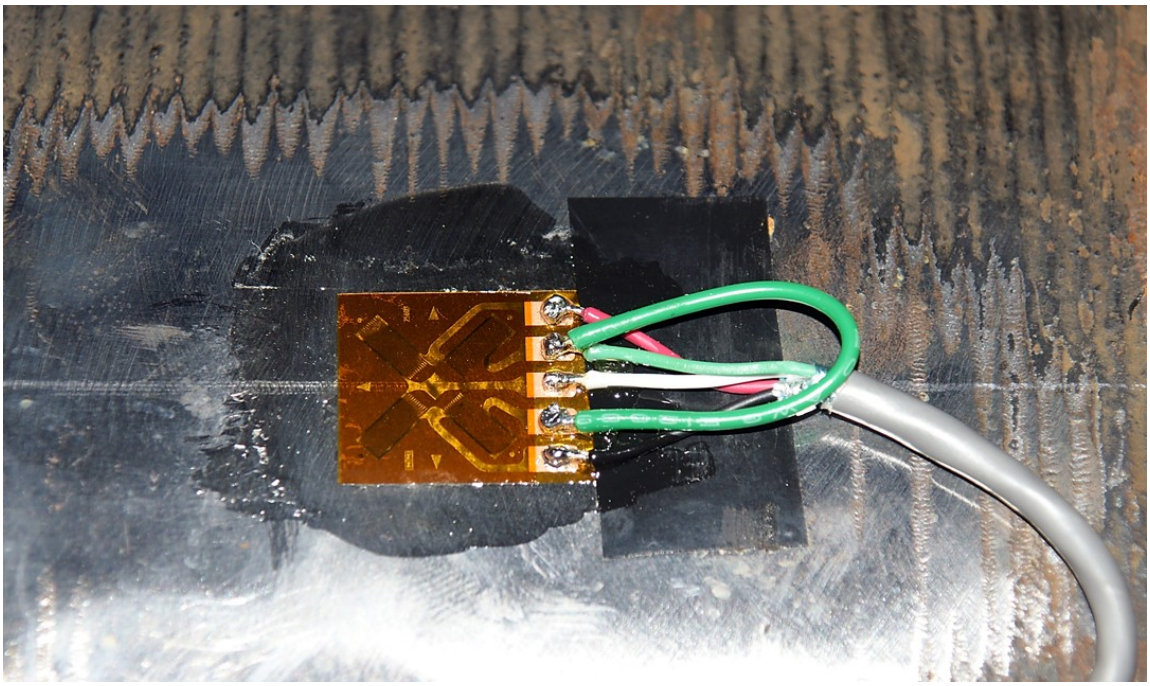

Figure 3.9: Full Bridge Strain Gage Installed on Drive Shafts

The linearized equation for torque as a function of measured output voltage for the full bridge torque configuration is

$$T = k_2 \, V_{OUT} \tag{3.2}$$

Where,

$k_2 =$ $-3.08 \times 10^7 \left(\frac{\text{lb-ft}}{\text{V}}\right)$

Appendix D presents Wheatstone Bridge circuitry and sensitivity calculations for quarter bridge, half bridge, and full bridge configurations. While full and half bridge configurations compensate for temperature variation, lead wire resistance changes affect strain gage measurements (Beckwith et al. 1995). The location of several transducers required cable lengths of over 200 ft; resistances in wires of such length vary along the length of the cable because of temperature and material variations. IOTech strain gage modules have a remote sense feature continuously ensuring that the voltage provided by the module is such that the appropriate excitation voltage reaches the instrument. Figure 12 shows the basic wiring of the remote sense feature. Excitation voltage from the module is increased by an amount equal to the voltage drop between the module and strain gage location. This loss is the difference between V_{EX} and V_S in Figure 3.10.

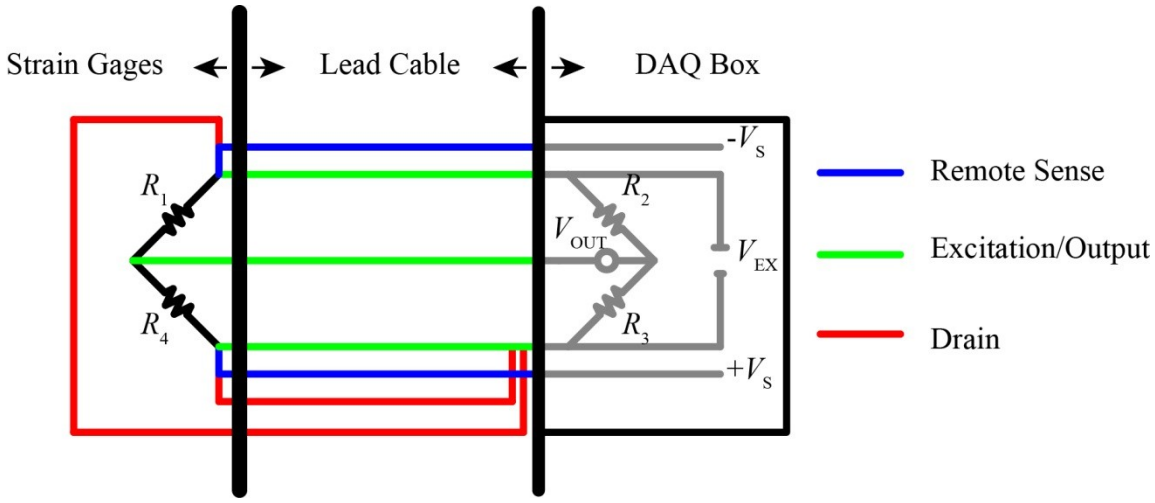

Figure 3.10: Wiring Diagram for Half Bridge Configuration with Remote Sense

3.3.4 Angle Measurement

Two methods of angular measurement have been utilized to estimate the Salmon Bay Bridge's angle of opening. Clinometers provide the primary angle measurements,

and rotary encoder wheels provide auxiliary angle measurements. The clinometers mounted on the counterweight truss are Penny and Giles STT280. These clinometers relate changes in position about an axis (relative to the direction of gravity) to an output voltage through a quarter bridge configuration similar to that of the electrical resistance strain gage. STT280 clinometers have a weather rating of IP68 which indicates water resistance in up to two meters for 24 hours (Penny and Giles 2010). Equation 3.3 represents the cubic function that approximates data from a calibration of one of the clinometers. The clinometers were mounted at an initial angle of 37.43 degrees.

$$\theta_{\mathrm{EAST}} = \left[k_3 + k_4 V_{\mathrm{OUT}} + k_5 {V_{\mathrm{OUT}}}^2 + k_6 {V_{\mathrm{OUT}}}^3\right] + k_7 \tag{3.3}$$

Where,

k_3 = -0.353 Deg.

k_4 = $23.970 \left(\frac{\text{Deg.}}{\text{V}}\right)$

k_5 = $0.235 \left(\frac{\text{Deg.}}{V^2}\right)$

k_6 = $1.474 \left(\frac{\text{Deg.}}{V^3}\right)$

k_7 = 37.43 Deg.

Rotary quadrature encoders were installed on the drive shafts of the Salmon Bay Bridge. Rotary quadrature encoder wheels relate rotation (angular position and angular velocity) of the wheel to a pair of electrical pulses which consist of square waves (EPC 2009). Data collected by DASYLab from the rotary encoders is collected in units of counts based on the number of square waves detected as the device rotates. Counts (*CTS*) were related, through calibration with the clinometers, to the bridge's angle of opening through the following equation

$$\theta_{EAST} = k_8 CTS \tag{3.4}$$

Where,

$$k_8 = \quad -8.807 \times 10^{-4} \left(\frac{\text{Deg.}}{\text{Counts}}\right)$$

3.4 Installation of Transducers on Salmon Bay Bridge Testbed

The initial installation of the data acquisition system occurred in September of 2009. All components necessary for monitoring the Salmon Bay Bridge were included in this installation. The first installation lasted three days. The first two days consisted of running lead cables to strain gages attached to counterweight truss members. The BNSF crew completed this task quickly, professionally, and safely. The third day was spent installing the weather station, installing torque strain gages on drive shafts, assembling the data acquisition system, and fine tuning the data acquisition trigger mechanisms. By the end of the third day, the monitoring system was autonomously recording strain, angle, and torque data for each opening and closing.

Three additional installations were performed from September 2009 to November 2010. During each installation, any malfunctioning transducers were repaired or replaced. Table 3.1 summarizes the chronology of installation, and Table 3.2 summarizes the final transducer details.

Table 3.1 Installation Schedule

Date	Installed Transducers	Repaired Transducers	Installation Crew
September 2009 (3 Days)	40 Weldable Strain Gages 2 Drive Shaft Strain Gages 2 Clinometers 2 Encoder Wheels 1 DAQ System Weather Station	n/a	Dr. Gary Fry Steven Rogers Dr. Stefan Hurlebaus Brett Story BNSF Crew
November 2009 (2 Days)	16 Weldable Strain Gages	West Drive Shaft Strain Gage	Dr. Gary Fry Steven Rogers BNSF Crew
June 2010 (2 Days)	2 Clinometers	1 CWT Strain Gage	Dr. Gary Fry Steven Rogers Brett Story BNSF Crew
November 2010 (2 Days)	16 Weldable Strain Gages	4 CWT Strain Gages	Dr. Gary Fry Steven Rogers Brett Story BNSF Crew

Table 3.2 Final Transducer Details

Description	Quantity	Manufacturer	Model(s)
Weldable Strain Gages	72	TML	AWC-88
Full Bridge Strain Gages	2	Vishay	CEA-250US-350
Clinometers	2	Penny and Giles	SST-280
DAQ Boxes	7	IOTech	(1) StrainBook 616 (5)WBK 16 (1) WBK 17
Weather Station and Control Panel	1	Davis	Vantage Pro2
DAQ Laptop	1	Dell	Latitude E6400 ATG

Cable management on the Salmon Bay Bridge was a primary concern from both the instrumentation and installation perspectives. Each strain gage pair, both clinometers, both rotary encoders, and both torque strain gages required a lead cable to transmit a signal back to the data acquisition system. Cables were routed along structural members to facilitate installation and protection of the cables and connections. Cables were fastened to angles or lacing of members. Some cable lengths of 280 ft. were required for counterweight truss strain gages. In total, 8900 ft. of cable was installed on the Salmon Bay Bridge.

3.5 Monitoring and Structural Impairment Detection

The focus of this dissertation is the development and implementation of a structural impairment detection algorithm. Once the transducer selection, instrumentation schedule, and data acquisition programs were completed and installed, monitoring of the Salmon Bay Bridge testbed began. Once values of typical strain ranges for transducers were observed, an alert system was created in DASYLab that would send an email if an abnormal reading was taken. This system provides constant evaluation of transducer integrity and notifies responsible parties of abnormal changes in structural behavior. The messages contain information about which channel is receiving an abnormal signal and if the signal is high or low. This alert feature alone has provided valuable information for engineers interested in monitoring the Salmon Bay Bridge testbed; a successful SIDS would provide not only an alert to abnormal signals, but streamlined information on what is causing abnormal signals.

In parallel with monitoring the test bed during opening/closing events, maintenance, rebalancing, and counterweight trunnion replacement, data streams were recorded and used to develop a simulated testbed environment with which to develop and refine the algorithms, software, and logistics associated with an autonomous SIDS. A DASYLab environment simulating typical testbed behavior was created with which to evaluate and integrate the SIDS.exe structural impairment detection software application.

The Windows based application SIDS.exe evaluates data streams recorded from an opening or closing of the Salmon Bay Bridge. A self-contained installation package created with MATLAB's Complier Toolbox contains all files necessary to perform a structural impairment detection analysis with trained neural networks; MATLAB installation is not necessary on the data acquisition laptop (MATLAB 2011). Figure 3.11 illustrates the operational details of the SIDS applied to the Salmon Bay Bridge testbed. A DASYLab action module was set to execute the outside application, SIDS.exe, which opens written data files, analyses the data with competitive neural arrays, and produces a text file that reports an operational classification for each angle of opening.

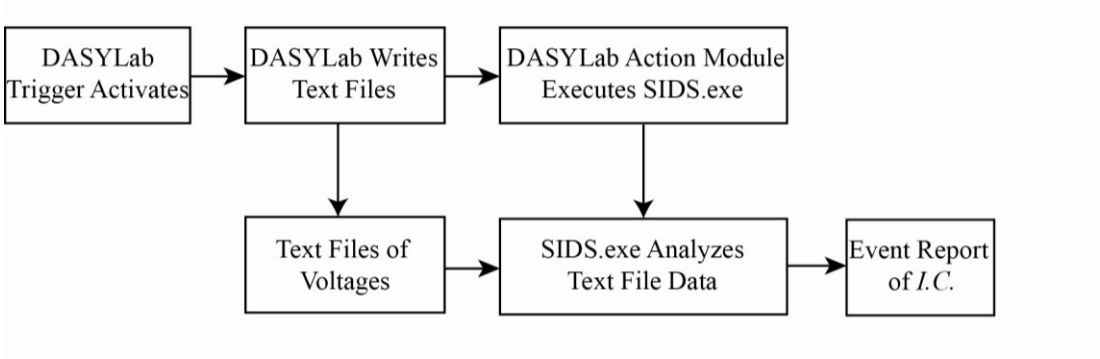

Figure 3.11: SIDS Operational Flowchart

The mock Salmon Bay Bridge environment provided an opportunity to simulate openings and closings under any desired conditions. The opening rate and stress ranges were linearly approximated to reflect the appropriate known time histories for each channel. An additional feature available in the mock environment was the ability to "impair" the simulated bridge as it opened or closed. Impairment was specified with a switch that altered data streams for specified impairment cases. Figure 3.12 illustrates the operation of the mock environment that has just experienced an impairment change.

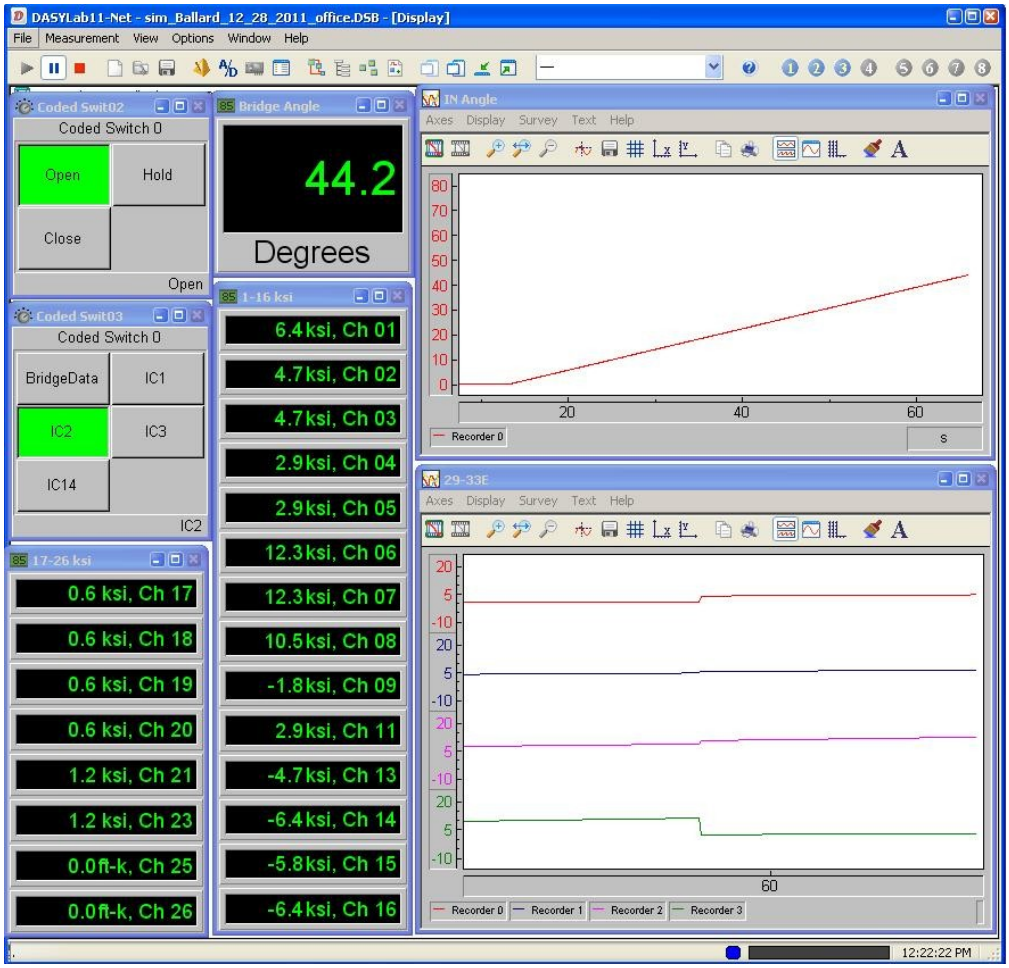

Figure 3.12: Simulated Opening of Salmon Bay Bridge Testbed

CHAPTER IV
RESULTS

4.1 Scope of Results

The results presented for this project stem from the procedures outlined in Chapter II and Chapter III. The results encompass two regimes: 1) the analytical and experimental evaluation of the Salmon Bay bridge testbed via finite element models and instrumentation, and 2) structural impairment detection via competitive neural networks.

4.2 Analytical and Experimental Results from the Salmon Bay Bridge

This section highlights key results from analytical and experimental procedures performed while analyzing the Salmon Bay Bridge. The behavior of the bridge was estimated and quantified. The structural response of counterweight truss members, torque results from drive shafts, and dynamic characteristics of the bridge are key behavioral features of the Salmon Bay Bridge.

4.2.1 Stress Range Measurements from the Salmon Bay Bridge

The primary diagnostic data streams for the development of a structural impairment detection system are stress ranges in counterweight truss members. Figure 4.1 reports stress range data for the west main chord 29-33W for a typical full opening of the bridge.

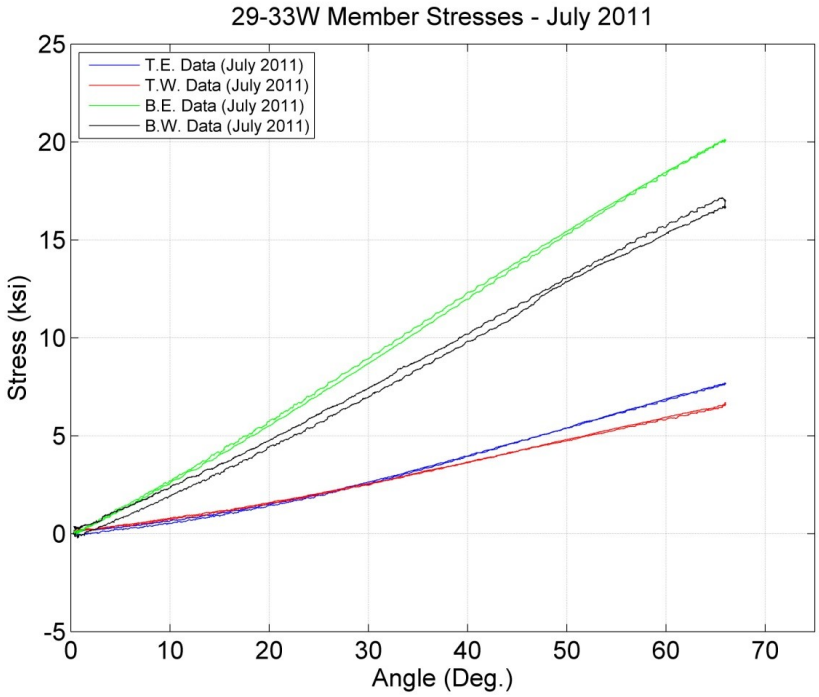

Figure 4.1: Main Chord Stress Ranges vs. Angle of Opening

Stresses in the bottom flanges of member 29-33W increase by 20 ksi and 16 ksi for the east and west flanges, respectively. The top flanges increase by 7.5 ksi and 6 ksi for the east and west flanges. Comparisons of stress range for several counterweight truss members can be made between experimental data collected during the current monitoring effort, experimental data from instrumentation in 1952, analytical data from SAP2000, and refined analysis results from ABAQUS. A comparison of these results for member 29-33W is shown in Figure 4.2.

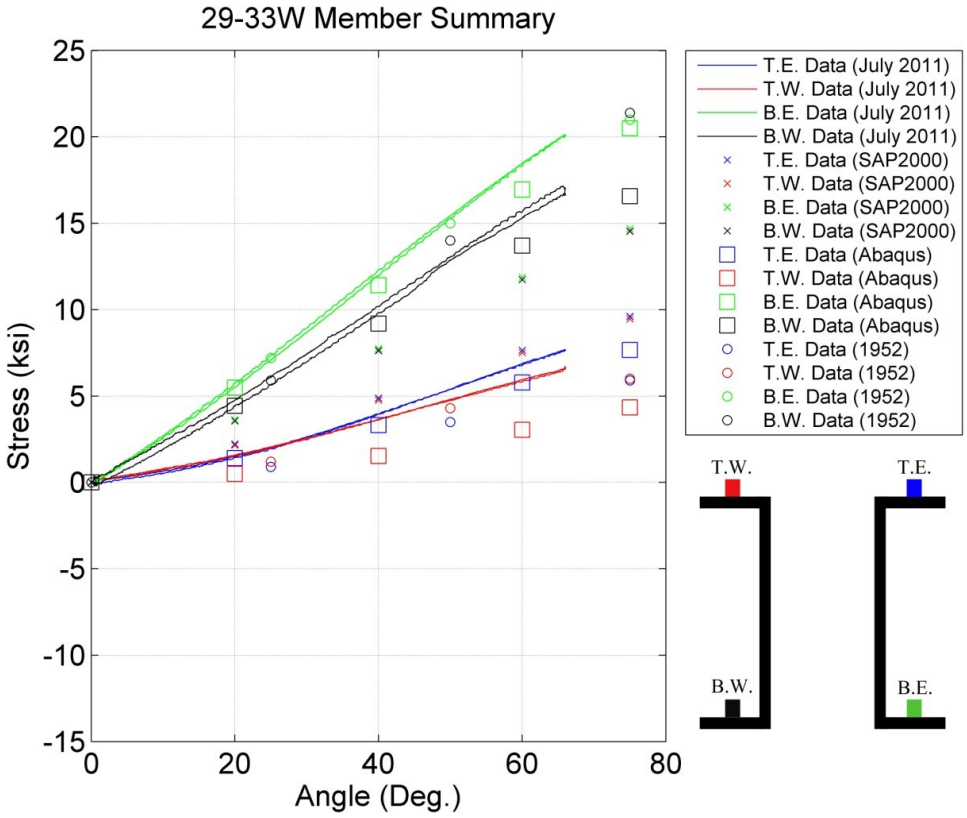

Figure 4.2: Summary of Stress Ranges for Member 29-33W

Continuous data represents data recorded from July 2011. The discrete circles represent readings from the 1952 instrumentation. SAP2000 data and ABAQUS data are represented by colored "X" and square shapes, respectively. The experimental data from 2011 and 1952 match favorably. Since 1952, an increase in separation has occurred between the bottom east and west flange curves. Top flange results from 2011 are consistently higher than 1952 results. Analytical calculations exhibit trends similar to those observed in experimental measurements. The SAP2000 data underestimate the bottom flange stress ranges and overestimates the top flange stresses; SAP2000 results do not capture the same amount of separation between the bottom flange stress range curves and top flange stress range curves seen in the experimental results. ABAQUS

results are an improvement over SAP2000 results in both the magnitude of stress range values and the overall behavior of the flanges. A separation between curves is present representing the top and bottom east and west flanges. Appendix E contains member summaries for all instrumented members of the counterweight truss.

4.2.2 Vibration Results for the Salmon Bay Bridge

Vibration characteristics were extracted from the time histories of clinometers and strain gage output. Figure 4.3 displays the angle of opening vs. time for a typical opening of the Salmon Bay Bridge. Figure 4.4 shows a closer examination of the data at 20 and 60 degrees as the bridge opens.

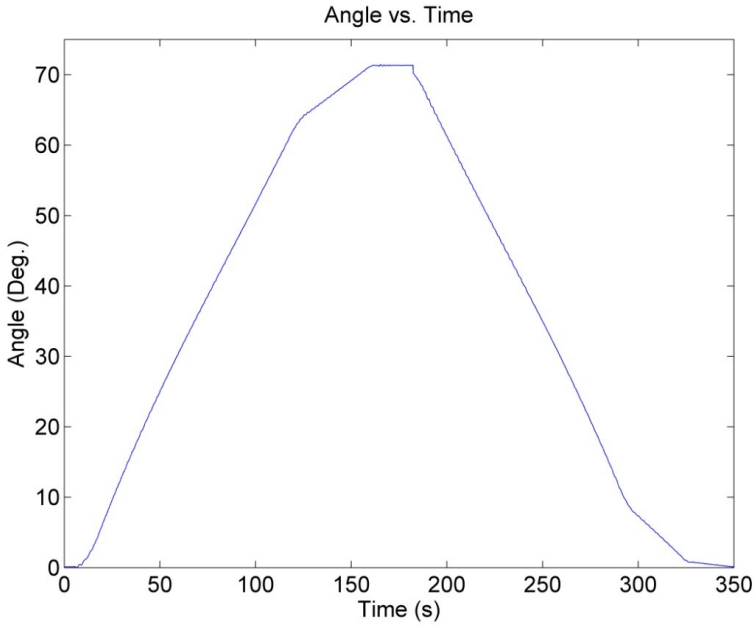

Figure 4.3: Angle of Opening vs. Time

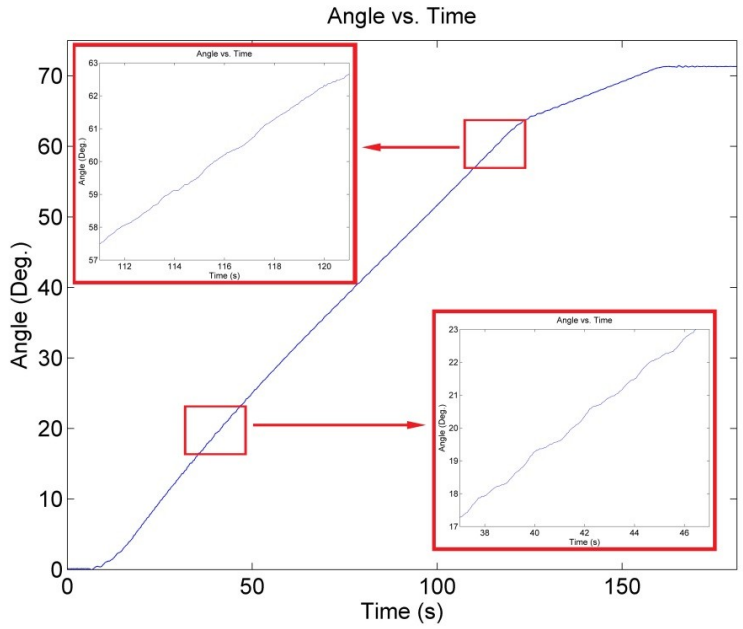

Figure 4.4: Detailed Measurements from Clinometers

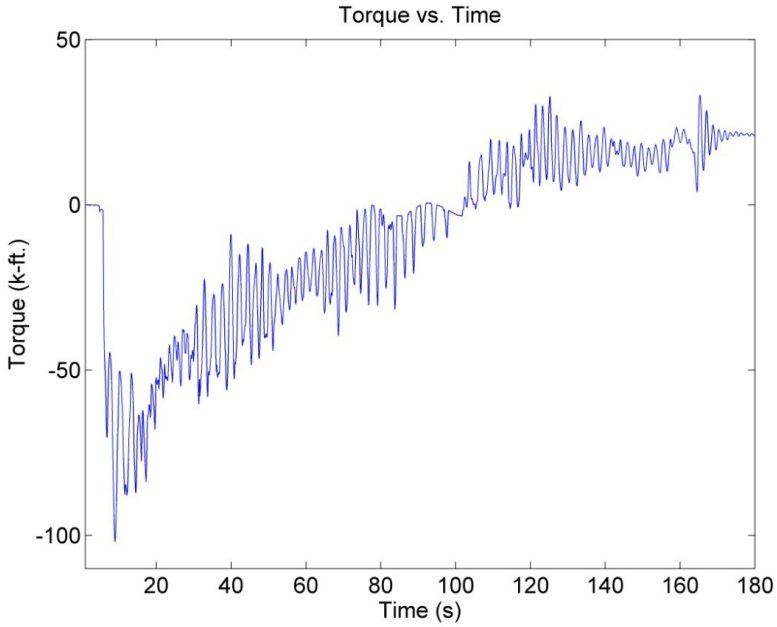

Figure 4.5: Torque vs. Time for an Opening

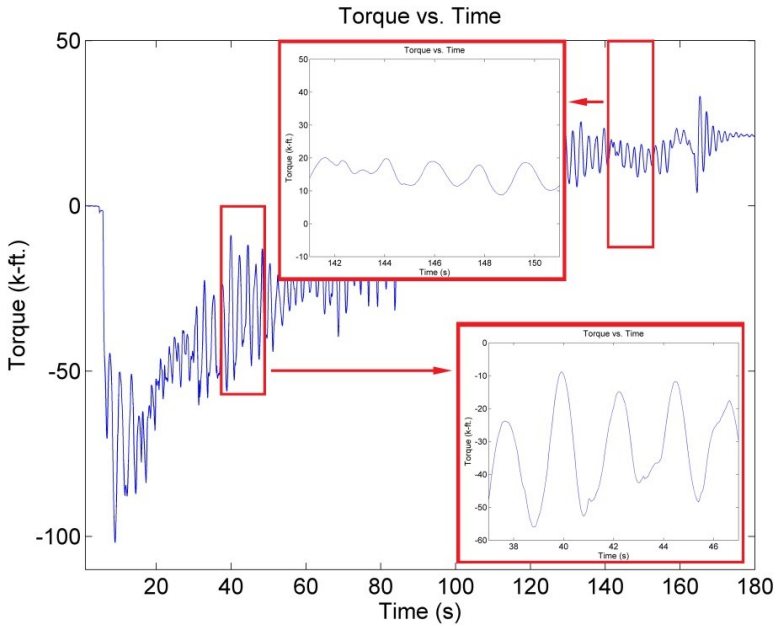

Figure 4.6: Detailed Measurements from Drive Shaft Strain Gages

Figures 4.5 and 4.6 present the time histories of drive shaft torque data from the east drive shaft. The frequency content in clinometer data and drive shaft strain gage data is very similar. By inspection, a 1.6-2.5 second period, or 0.40-0.60 Hz frequency, can be seen in the clinometer data and drive shaft data as the bridge is opening.

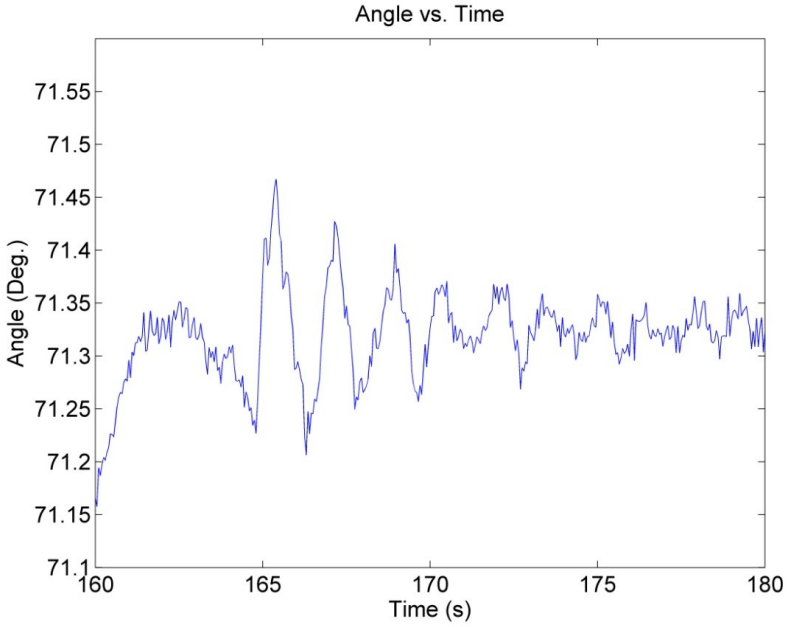

Figure 4.7: Free Vibration Data at Full Open

When the bridge reaches its peak opening angle, a damped, free vibration response occurs. Figure 4.7 illustrates this behavior at 71 degrees. By examining the opening data from near 20, 40, 60, and 75 degrees, a comparison of observed vibration characteristics can be made with the predictions presented in Chapter II. Table 4.1 contains calculated and observed vibration data from the Salmon Bay Bridge. The observed frequency of vibration follows the same trends as Equations 2.6-2.7 and the SAP2000 models; observed frequencies are larger than results from the SAP2000 3D models and smaller than results from Equation 2.7 and SAP2000 2D models.

Table 4.1: Natural Frequency Results

Angle (Deg.)	f_{n1} (Hz)			f_n, Observed (Hz)
	Eq. (2.7)	SAP2000 2D	SAP2000 3D	
0	0.71	0.70	0.29	n/a
20	0.84	0.83	0.38	0.54
40	0.95	0.92	0.40	0.56
60	1.03	0.97	0.40	0.60
75	0.98	0.88	0.37	0.56

4.2.3 Drive Shaft Torque vs. Angle of Opening

The behavior of the Salmon Bay Bridge drive shafts is captured in Figure 4.8. Experimental results from July 2011, a friction compensated average of experimental results, values from SAP2000 analyses, and the analytical model described by Equation 2.4 are reported for comparison.

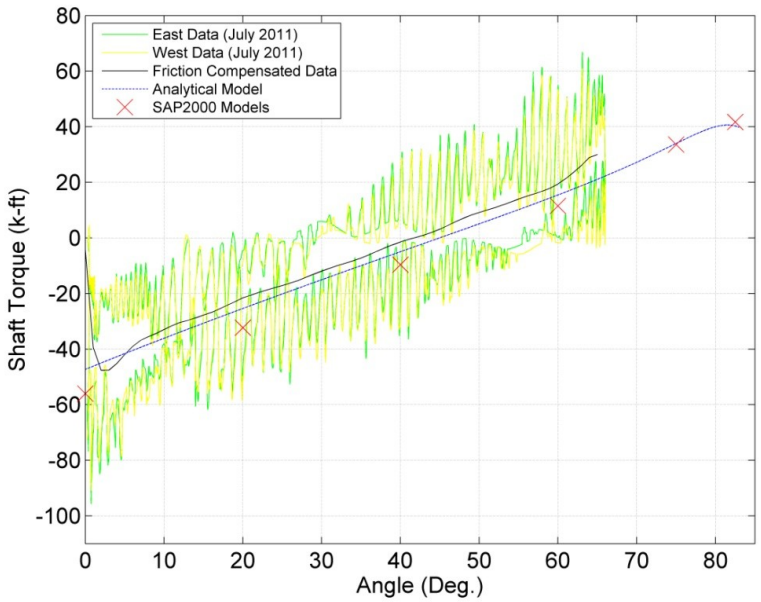

Figure 4.8: Drive Shaft Torque vs. Angle of Opening

A hysteresis loop can be seen in the experimental data. The lower path of the east and west drive shafts represents the drive shaft torque as the bridge opens; the upper path results from the bridge closing. Here, a negative torque value tends to rotate the drive shaft towards the leaf while a positive torque value tends to rotate the drive shafts toward the counterweight. The maximum negative torque, -95.6 k-ft. and -90.8 k-ft., occurs when first opening the bridge for the east and west shafts, respectively. The maximum positive torque, 66.8 k-ft. and 63.1 k-ft., respectively, occurs when the bridge begins to close at 63 deg. The friction compensated curve represents an average of the opening and closing paths for the drive shafts. The balance point where no torque exists in the drive shafts occurs at 55-62 deg. while opening and at 27-38 deg. while closing.

4.3 Structural Impairment Detection Results

This section presents results pertaining to structural impairment detection. Developing an effective structural impairment detection system using neural networks requires training data with which to develop the necessary relationships for impairment detection and behavior classification. Structural impairments were modeled in SAP2000 and ABAQUS. The comparison of impaired and unimpaired data streams, classification results of impaired data streams from neural networks, and results from simulated bridge operation under various impairment scenarios are presented.

4.3.1 Structural Impairment Detection System Trained on SAP2000 Data Streams

Impairment modeling in SAP2000 consisted of the reduced section properties of beam elements as discussed in Chapter II. Figure 4.9 illustrates impaired and unimpaired data streams from the east main chord member for partially and fully reduced sections of the east main chord member. Figure 4.10 illustrates the response of a bracing member to the same impairments. While the results from a fully reduced section are distinguishable from the unimpaired results, the response results of a partial section reduction are negligibly different than the unimpaired response. Appendix F provides complete numerical data of differences and percent differences between impaired and unimpaired results.

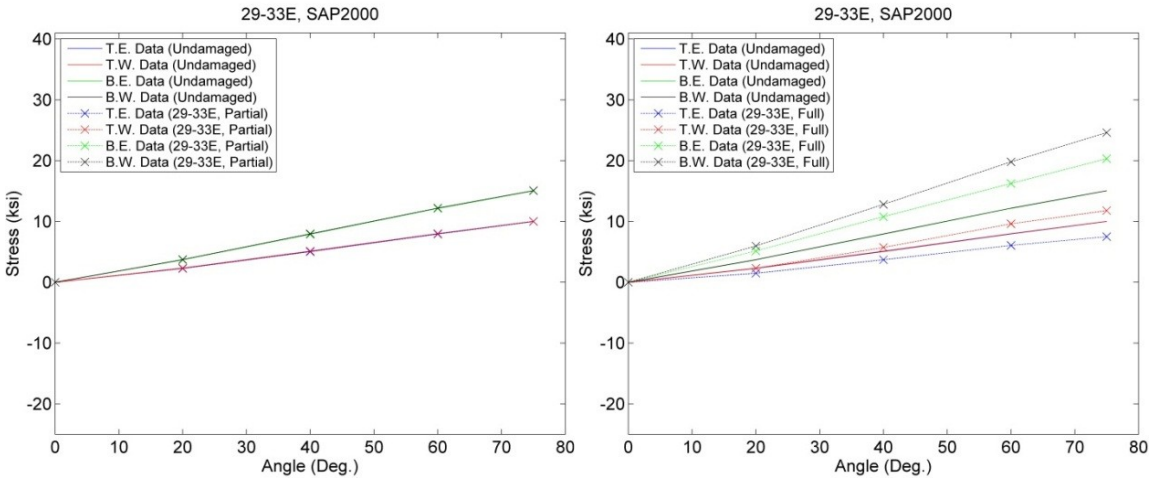

Figure 4.9: SAP2000 Impaired Data Streams of 29-33E

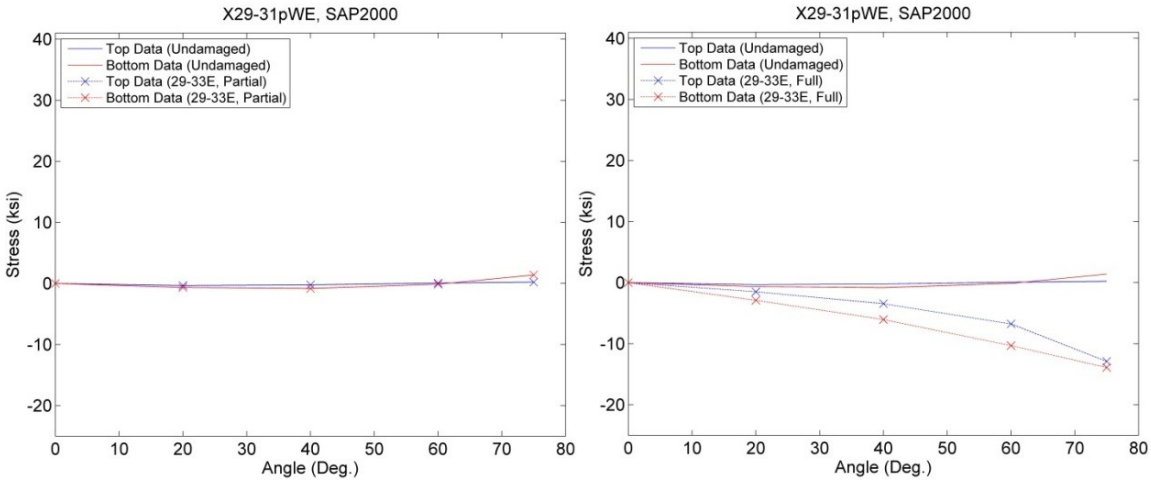

Figure 4.10: SAP2000 Impaired Data Streams of X29-31WE

An array of competitive neural networks was trained for each 10 degree angle of opening from SAP2000 data streams. Each impairment data stream was presented to the trained neural networks, and an impairment classification was made. Simulated data streams consisted of training data with added noise. Table 4.2 displays results from each

angle of opening (row) and each damage case (column). Correct classifications result in the number of the impairment case; incorrect classifications are indicated in red. The structural impairment detection system trained on SAP2000 data correctly classifies 95.6% of data streams. If the mode of each column is used as the impairment result, the networks correctly predict all impairment cases.

Table 4.2: Neural Network Classification Based on SAP2000 Data Steams

Angle	I.C. 1	I.C. 2	I.C. 3	I.C. 4	I.C. 5	I.C. 6	I.C. 7	I.C. 8	I.C. 9	I.C. 10	I.C. 11	I.C. 12	I.C. 13	I.C. 14	I.C. 15	I.C. 16	I.C. 17
10	1	2	3	4	5	5	7	8	9	10	11	12	13	14	15	2	3
20	1	2	3	4	5	6	7	8	9	10	11	12	13	14	15	16	17
30	1	2	3	4	5	6	7	8	9	10	11	12	13	14	15	16	17
40	1	2	3	4	5	6	7	8	9	10	11	12	13	14	15	16	17
50	1	2	3	4	5	6	7	8	13	10	11	12	13	14	15	16	17
60	1	2	3	4	5	6	7	8	9	10	11	12	13	14	15	16	17
70	1	2	3	4	5	6	7	8	9	2	11	12	13	14	15	16	17
80	1	2	3	4	5	6	7	7	9	10	11	12	13	14	15	16	17

4.3.2 Structural Impairment Detection System Trained on ABAQUS Data Streams

Impairment modeling in ABAQUS focused on improved section reduction modeling in the main chords and broken embedded members. Figures 4.11 and 4.12 show impaired and unimpaired results for the same members and impairments displayed in Figures 4.9 and 4.10. A significant departure from the unimpaired response can be seen in the results representing a partially reduced section. Appendix F provides the complete numerical data of differences and percent differences between impaired and unimpaired results.

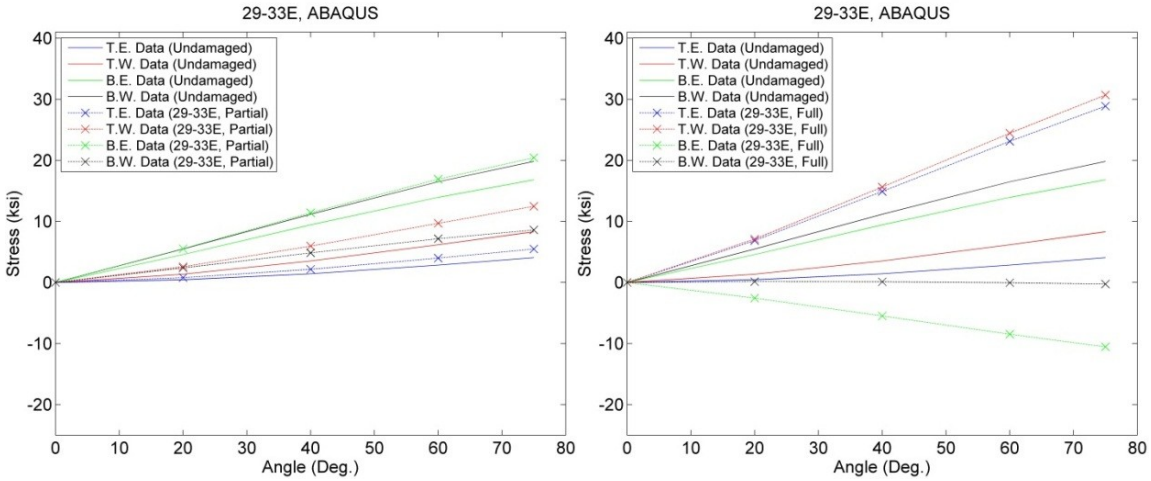

Figure 4.11: ABAQUS Impaired Data Streams of 29-33E

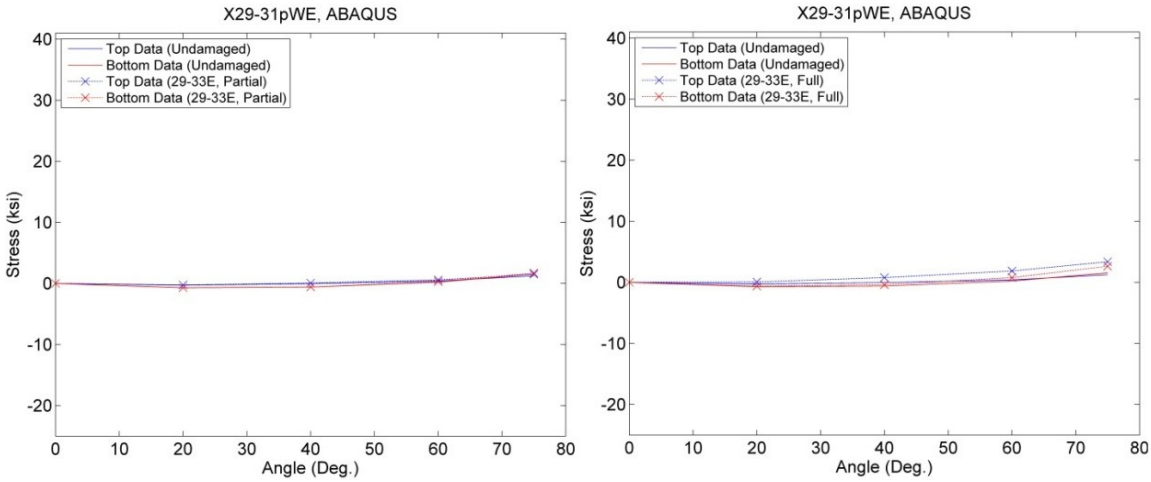

Figure 4.12: ABAQUS Impaired Data Streams of X29-31WE

In addition to a structural impairment detection system trained on SAP2000 data, a separate group of neural arrays were trained on results from ABAQUS. Table 4.3 displays impairment classifications resulting from the analysis of ABAQUS data streams. Correct classifications are indicated by the numerical value of impairment case;

incorrect classifications are indicated in red. The structural impairment detection system trained on ABAQUS data correctly classifies 94% of data streams. If the mode of each column is used as the impairment result, the networks correctly predict all impairment cases.

Table 4.3: Neural Network Classification Based on ABAQUS Data Steams

Angle	I.C. 1	I.C. 2	I.C. 3	I.C. 4	I.C. 5	I.C. 6	I.C. 7	I.C. 8	I.C. 9	I.C. 10	I.C. 11	I.C. 12	I.C. 13	I.C. 14	I.C. 15	I.C. 16	I.C. 17
10	1	2	3	2	5	6	7	8	9	10	11	12	13	14	15	10	12
20	1	2	3	4	5	6	7	8	9	10	11	12	13	14	15	16	17
30	1	2	3	4	5	6	7	8	9	10	11	12	13	14	15	16	17
40	1	2	3	4	5	6	7	8	9	10	11	12	13	14	15	16	17
50	1	4	3	4	5	6	7	8	9	10	11	12	13	14	15	10	17
60	1	2	3	14	5	6	7	8	9	10	11	12	13	14	15	8	17
70	1	2	3	4	1	6	7	8	9	10	11	12	13	14	15	16	17
80	1	2	3	4	5	6	7	8	9	10	11	12	13	14	15	16	17

4.3.3 Impairment Detection of Salmon Bay Bridge Data

Data streams from the Salmon Bay Bridge were analyzed with structural impairment detection systems trained on ABAQUS data. Table 4.4 shows results from openings throughout this project's monitoring effort.

Table 4.4: Impairment Case Classifications by SIDS on Salmon Bay Bridge Data

Angle of Opening (Deg.)	Nov. 2009	Mar. 2010	July 2010	Nov. 2010	Mar. 2011	July 2011	Nov. 2011
10	14	14	1	1	1	14	14
20	14	14	1	1	1	14	14
30	1	1	1	1	1	1	1
40	1	1	1	1	1	1	1
50	14	n/a	1	1	1	1	1
60	14	n/a	1	1	1	14	n/a
70	14	n/a	1	14	n/a	n/a	n/a

Most results from the Salmon Bay Bridge indicate data that most closely resembles I.C. 1 (nominal behavior). Occasionally, the SIDS reports that data resembles I.C. 14, which represents impairment to the embedded member at the 33 E joint. A preliminary version of SIDS identified the opening from March 2011 as I.C. 6, which represents a partial section loss of the west main chord member at 33W. Two strain gages were malfunctioning during March 2011. Chapter V addresses training improvements to account for transducer malfunction.

4.3.4 Impairment Detection of Simulated Impairments of the Salmon Bay Bridge

To examine the effectiveness of the complete structural impairment detection system, simulated impaired data streams were analyzed with the SIDS.exe application as executed by DASYLab. The simulated impairment was a section loss of the east main chord just south of the connection at 33 (impairment cases 2 and 3 from the ABAQUS analyses). An opening of 70 degrees is simulated with a partial loss of section (I.C. 2) occurring at 25 degrees and a full section loss (I.C. 3) occurring at 55 degrees. Figure 4.13 shows the angle-time history and the stress-time history of the simulated opening; regions of impairment are labeled and separated by vertical lines. Jumps in stress indicate changes in impairment conditions.

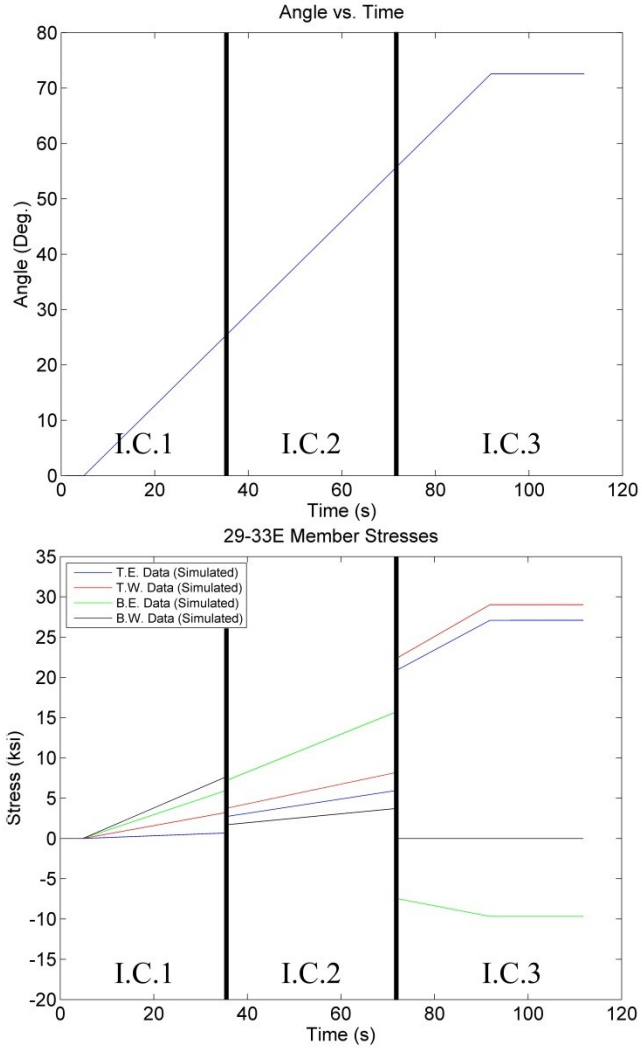

Figure 4.13: Parameters for Simulated Impairment of the Salmon Bay Bridge

The output from the text file created by the SIDS application is displayed in Figure 4.14. The prediction is correct for each angle of opening.

```
Angle :   10  20  30  40  50  60  70
I.C. :    1   1   2   2   2   3   3

I.C. Codes:

1 - Unimpaired
2 - Joint 33 East, South, Partial Section Loss
3 - Joint 33 East, South, Full Section Loss
4 - Joint 33 East, North, Partial Section Loss
5 - Joint 33 East, North, Full Section Loss
6 - Joint 33 West, South, Partial Section Loss
7 - Joint 33 West, South, Full Section Loss
8 - Joint 33 West, North, Partial Section Loss
9 - Joint 33 West, North, Full Section Loss
10- Joint 32 East, Partial Section Loss
11- Joint 32 East, Full Section Loss
12- Joint 32 West, Partial Section Loss
13- Joint 32 West, Full Section Loss
14- Joint 33 East, Impaired Embedded Member
15- Joint 33 West, Impaired Embedded Member
16- Joint 32 East, Impaired Embedded Member
17- Joint 32 West, Impaired Embedded Member
```

Figure 4.14: Output File Produced by the SIDS

CHAPTER V
DISCUSSION

5.1 Scope of Discussion

The discussion of results from Chapter IV consists of observations and commentary on each aspect of the project. Analytical and experimental results are examined; assumptions are addressed, verified, and results are validated. The performance of neural impairment detecting algorithms is evaluated, and key findings are discussed. Additionally, comments and suggestions for future work in the area of structural impairment detection are included.

5.2 Analytical and Experimental Results from the Salmon Bay Bridge

This section comments on results analytically and experimentally obtained from the study of the Salmon Bay Bridge. A clear understanding of these results was critical in generating data streams on which to train neural structural impairment detection algorithms. Stress ranges, dynamic behavior, and drive shaft operation were considered.

5.2.1 Stress Ranges in Salmon Bay Bridge Counterweight Truss Members

The diagnostic data streams used in training neural algorithms for structural impairment detection comprise stress ranges as functions of bridge angle. The success of simulating impaired data streams depends on the ability to accurately predict stress ranges in the counterweight truss members of interest. Figure 4.12 compares predictions from SAP2000 and ABAQUS with observations made during this project (2011) and in 1952. ABAQUS results captured the essential features of stresses in the west main counterweight chord better than SAP2000 results. Specifically, ABAQUS reported a separation of stress ranges for both sets of top and bottom flanges; this behavior was not captured in the SAP2000 results. This separation between east and west flanges indicates the presence of significant out of plane bending. ABAQUS models slightly underestimated the stress ranges for all flanges.

When considering counterweight truss members that serve as bracing members, the SAP2000 and ABAQUS results were quite similar and agree well with observed field results. These members were more easily modeled and have smaller internal bending effects; axial load is the primary load effect.

The refinement of geometry (i.e. shell cross-sections) and improvements in concrete counterweight modeling in ABAQUS produced an analytical model that behaved more realistically than the simpler frame analysis model used in SAP2000. Results from SAP2000 analyses provided excellent indications of impairment locations and locations sensitive to impairment. Indeed, data streams created with SAP2000 may be used to detect severe impairments such as the full section loss of a critical member. The refined analyses performed in ABAQUS served as a complete and final analysis of the Salmon Bay Bridge, and produced a more accurate representation of subtle impairments such as partial section loss and impairment of embedded members.

An estimate of total stress in the west main chord of the counterweight truss is shown in Figure 5.1. The initial stresses at 0 degrees were calculated from the unimpaired ABAQUS model; analytical (ABAQUS) and experimental stress ranges are shown.

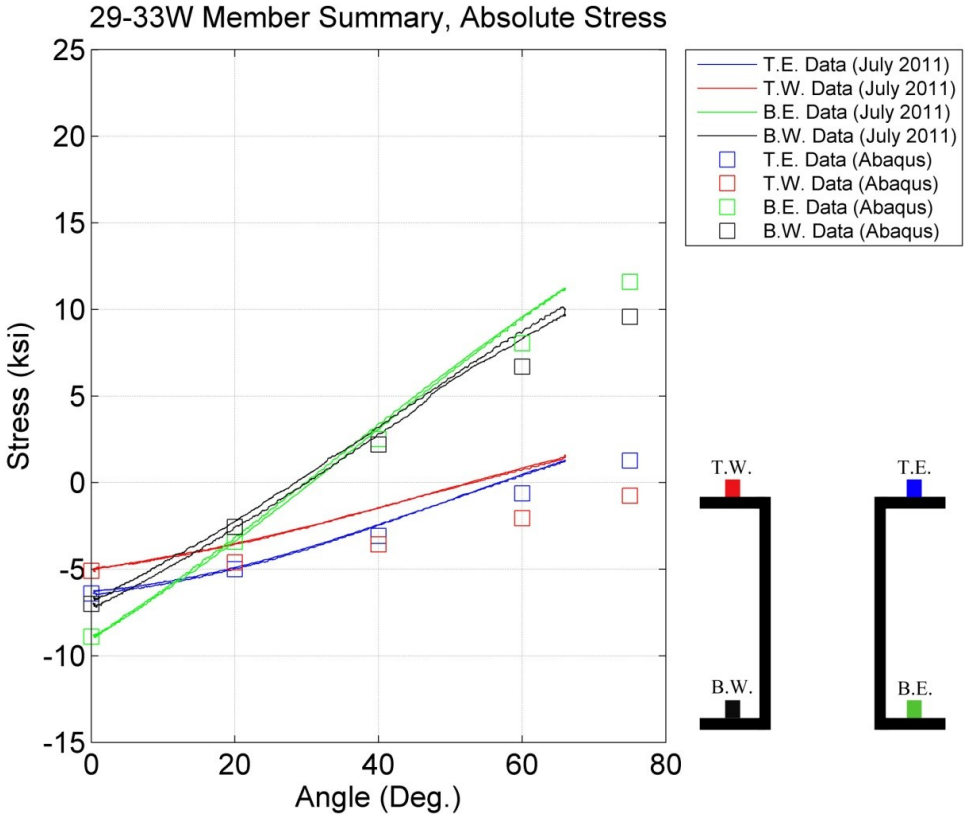

Figure 5.1: Absolute Stress Estimates in Counterweight Main Chords

The initial stresses in all flanges are compressive and the final stresses are tensile. This indicates that the main chords of the counterweight truss experience stress reversals. For member 29-33W, the critical flange is the bottom east flange which experiences a stress range of 20.1 ksi (for an opening of 66 degrees) with maximum compressive and tensile values of -8.9 ksi and 11.2 ksi, respectively.

5.2.2 Dynamic Behavior of the Salmon Bay Bridge

Results featuring the dynamic characteristics of the Salmon Bay Bridge revealed important aspects of its behavior from the perspective of developing a structural impairment detection system. Analytical modeling used to produce data streams was carried out under the assumption that inertial effects on counterweight truss members

caused by the angular motion of opening and closing the bridge were small. If the inertial effects are small, the bridge vibrates about a static equilibrium position. Specifically, this assumption required that the accelerations of the masses produce forces in the counterweight truss members that were insignificant compared to the self weight of the structure. These inertial forces may be approximately quantified by considering the accelerations acting on the counterweight center of mass. Equations 5.1 and 5.2 represent the acceleration in the radial and tangential directions on the counterweight mass.

$$a_r = R_{\mathrm{CWT}}\omega^2 \tag{5.1}$$

$$a_\theta = R_{\mathrm{CWT}}\alpha \tag{5.2}$$

The angular velocity, ω, and angular acceleration, α, were approximated by taking first and second time derivatives of data presented in Figure 4.3. Figure 5.2 displays angular displacement (filtered to remove vibration), angular velocity, and angular acceleration as functions of time.

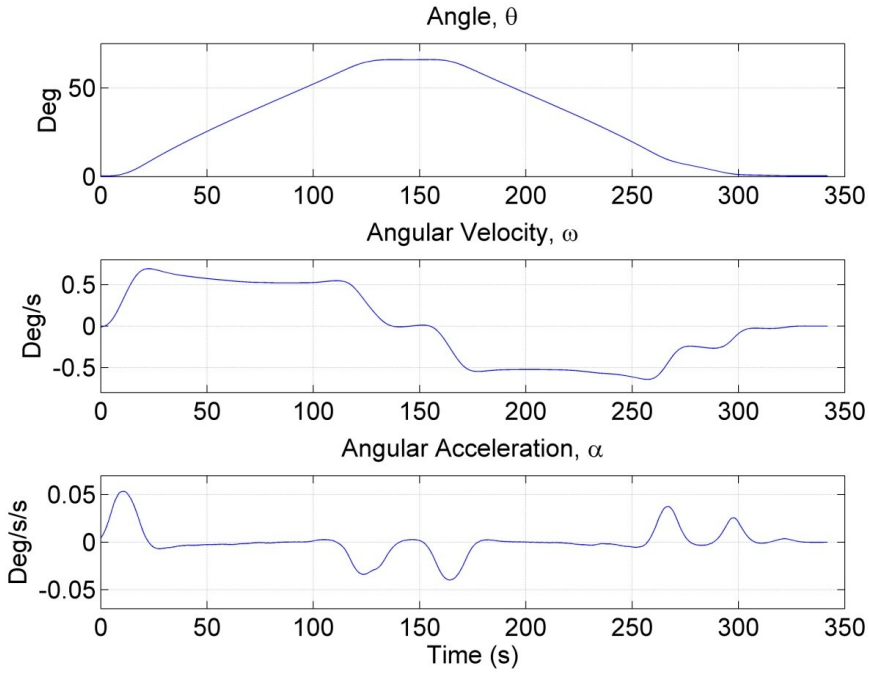

Figure 5.2: Angular Data for a Typical Opening and Closing of the Salmon Bay Bridge

In Figure 5.2, the slope of the angle vs. time curve is essentially piecewise linear, the angular velocity resembles a constant step function with a maximum value of 0.7 degrees/second, and angular acceleration is essentially zero except for a few regions and reaches a maximum of 0.054 degrees/second^2. Inertial forces resulting from accelerations caused by rotational motion are given in Equations 5.3 and 5.4.

$$F_{\mathrm{r}} = M_{\mathrm{CWT}} R_{\mathrm{CWT}} \omega^2 \tag{5.3}$$

$$F_{\theta} = M_{\mathrm{CWT}} R_{\mathrm{CWT}} \alpha \tag{5.4}$$

Substituting,

M_{CWT} = 93167.7 slug

R_{CWT} = 39 ft

ω = 0.7 deg/s =0.012 rad/s

α = 0.054 deg/s^2 =0.00094 rad/s^2

Estimates for the radial and tangential inertial forces are 0.52 k and 3.42 k, respectively. The magnitude of this inertial force is 3.45 k, which amounted to only 0.1% of the total counterweight self weight. The assumption of using a series of static models to recreate stress data streams is clearly valid. Figure 5.3 further illustrates the validity of the assumption; no appreciable increase or decrease in stress (beyond the vibration occurring in the member) occurred in the transition from opening to free vibration.

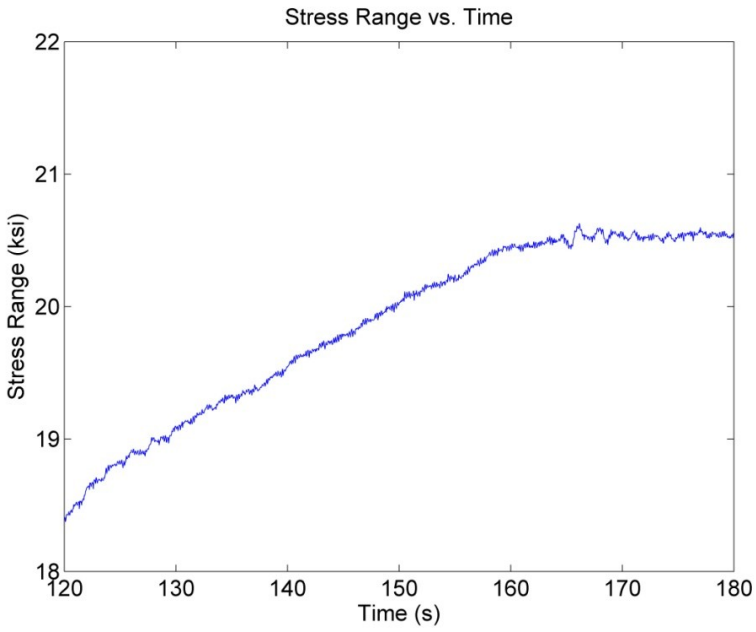

Figure 5.3: Transition from Steady Opening to Free Vibration in Main Chord Stress

The vibration response observed from the Salmon Bay Bridge, reported in Table 4.1, matched closely with the calculated first natural frequencies and was dependent on the angle theta as predicted by Equations 2.6, 2.7, and the SAP2000 models. The frequencies increase as the bridge opens to 60 degrees, then decrease at 75 degrees. The magnitudes of vibration frequency are lower than Equations 2.6, 2.7, and SAP2000 2D models but are higher than SAP2000 3D models. These results imply that the Salmon Bay Bridge testbed is less stiff than the two dimensional models and equations but more stiff than the three dimensional model.

5.2.3 Behavior of Salmon Bay Bridge Drive Shafts

Torque in the drive shafts was one measurement used to refine and calibrate analytical models used in data stream creation. Torque at the beginning of each opening is zero because, between openings, the drive shafts are mechanically disengaged from the driving machinery. This creates a unique opportunity to begin each measurement with the drive shafts in a state of zero strain and thus zero torque. This was the only absolute strain measurement available on the Salmon Bay Bridge; all strain measurements on the counterweight truss members were relative to some initial, unknown strain value caused by the self weight of the structure. Analytical models were calibrated through iterative adjustments of component weight estimates and component centers of gravity. The accuracy of estimations for weight and center of gravity of some components (i.e. leaf, operating struts, and counterweight truss structure) was higher than that of other components (i.e. reinforced concrete counterweight). Exact establishment of the content and placement of components embedded in the concrete was impossible, but a logical estimate of mass and center of gravity was obtained by examining their effects on torque values in the modeled drive shafts. Comparisons between torque values from strain measurements and several analytical models were used to establish estimates of counterweight properties. Analytical models were adjusted through logical and systematic variations of counterweight property information until the friction compensated result of observed torque values from the Salmon Bay Bridge aligned well with the results from Equation 2.4. Figure 5.4 illustrates the effect of

altering the counterweight mass and the location of its center of gravity on the torque vs. angle plot produced by Equation 2.4.

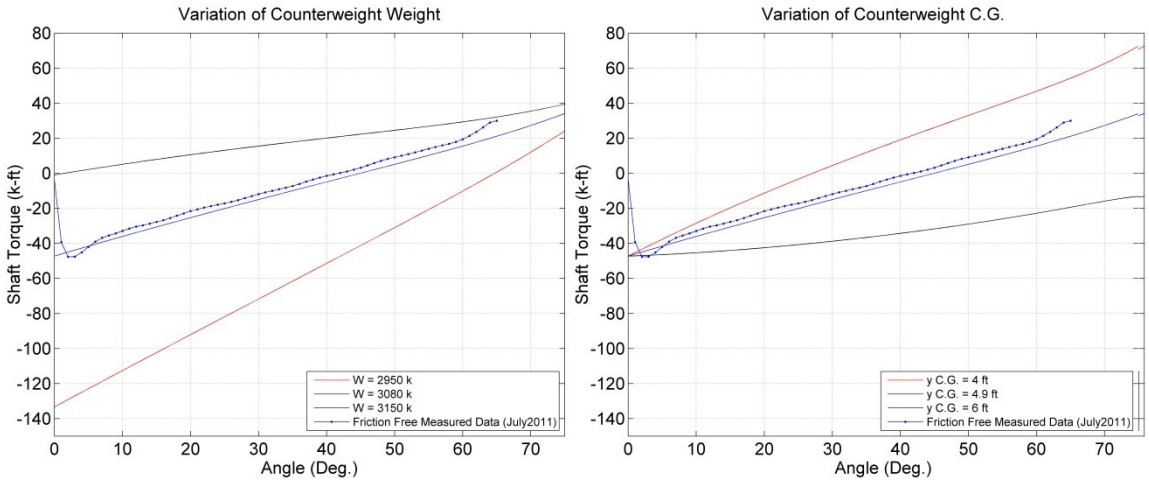

Figure 5.4: Effect of Varying Counterweight Properties on Drive Shaft Torque Values

The effect of varying the counterweight weight on drive shaft torque was most prominent near the closed position. A weight of 3080 k most closely matched the observed data. Increasing the weight of the counterweight decreased the magnitude of the average drive shaft torque, while decreasing the weight created a significant increase in negative torque. In practice, bridge engineers prefer a slightly leaf-heavy bridge so that the bridge will tend to close (near zero degrees) and remain closed while not in operation (Malvern et al. 1982, Koglin 2003). This is the case with the Salmon Bay Bridge.

Variation of the initially vertical distance between the counterweight C.G. and the counterweight trunnions greatly affected the drive shaft torques while the bridge is near full opening. When the bridge has rotated 70 degrees and is fully opened, the weight of the counterweight is acting vertically and has a moment arm nearly equal to the initial vertical C.G. location. A difference of 2 ft. in this moment arm determines if

the bridge behaves in a leaf-heavy or counterweight-heavy manner. The experimental data indicates that the bridge is indeed counterweight-heavy at full open.

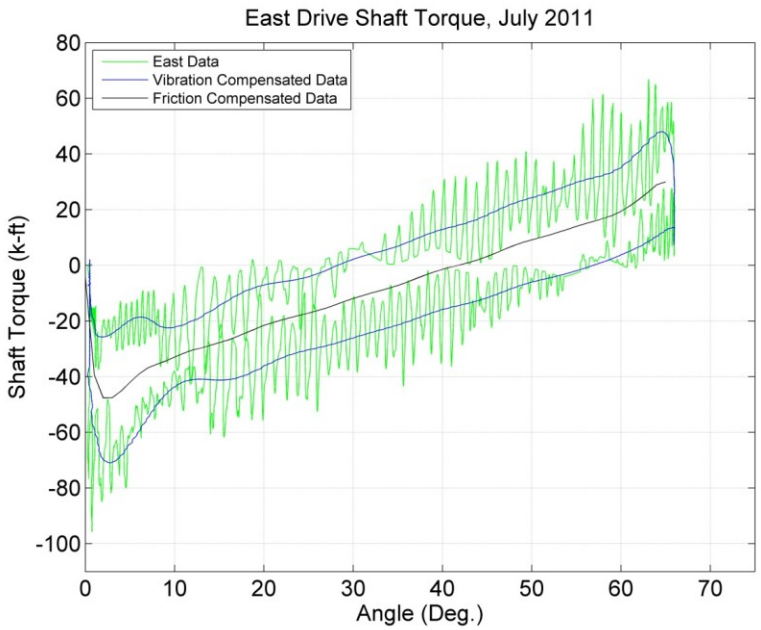

Figure 5.5: Salmon Bay Bridge East Drive Shaft Torque Data

Figure 5.5 includes average values of the torque in the east shaft and eliminates the vibration response in the shafts. Figure 5.5 indicates that the torque in the drive shafts is negative when the bridge begins to open (~2-5 degrees). This indicates that the bridge is "leaf-heavy" and will tend to lower when it is nearly closed. As the bridge opens, it remains leaf-heavy until approximately 55 degrees; beyond 55 degrees, as the bridge opens, the torque becomes positive and the bridge is "counterweight-heavy." While closing, the point between counterweight-heavy and leaf-heavy behavior shifts to approximately 28 degrees. As the bridge closes, it is leaf-heavy under 28 degrees and counterweight heavy over 28 degrees. The balance point where the average torque is

zero, as given by Figure 5.5, is 42 degrees (45 degrees by Equation 2.4); friction in the system is responsible for the shift in balance points as the bridge opens and closes.

The hysteresis loop in Figure 5.5 indicates that friction is present in the Salmon Bay Bridge. Friction forces and moments always oppose the motion of a mechanical system. As the bridge opens, the drive shafts must overcome the leaf-heavy torque imbalance and must also overcome the friction in the system. Operating struts are in tension during this portion of the opening. At the theoretical balance point shown in Figure 5.5, the observed torque is -14.8 k-ft. Once the bridge enters the counterweight heavy regime of the opening, the torque in the drive shaft becomes positive, operating struts experience compression, and the observed opening torque is actually less than the average torque. As the bridge begins to close, the behavior changes. The counterweight-heavy bridge is pushed downwards and torque from friction must be overcome. When the bridge is less than 28 degrees open, the observed torque is once again less than the average torque, indicating that the friction is reducing the demand on the system.

Torque caused by friction in the system is calculated as half of the vertical distance between the opening and closing path of Figure 5.5. Equation 5.5 represents an expression for friction torque.

$$T_{\mathrm{F}} = \frac{T_{\mathrm{CLOSE}} - T_{\mathrm{OPEN}}}{2} \tag{5.5}$$

The value of this quantity at the balance point is 14.8 k-ft and is nearly constant over the majority of the opening as shown in Figure 5. 6.

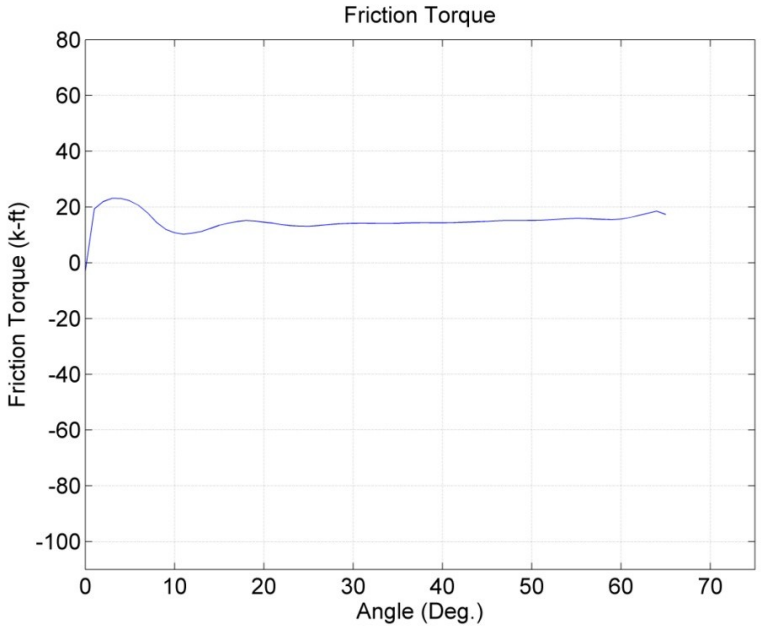

Figure 5.6: Friction Torque in the Salmon Bay Bridge System

Friction torque arises from friction in bridge components such as main trunnions, counterweight trunnions, and operating struts and their guides. The total torque in the drive shafts is expressed in Equation 2.4 with the inclusion of a non-linear friction term is given in Equation 5.6. The sign of the angular velocity determines if the magnitude T_{F} is added or subtracted from the torque caused by component weights.

$$T_{\mathrm{ADJ}} = T - \mathrm{sgn}\left(\dot{\theta}\right)|T_{\mathrm{F}}| \tag{5.6}$$

The plot resulting from Equation 5.6 is given in Figure 5. 7.

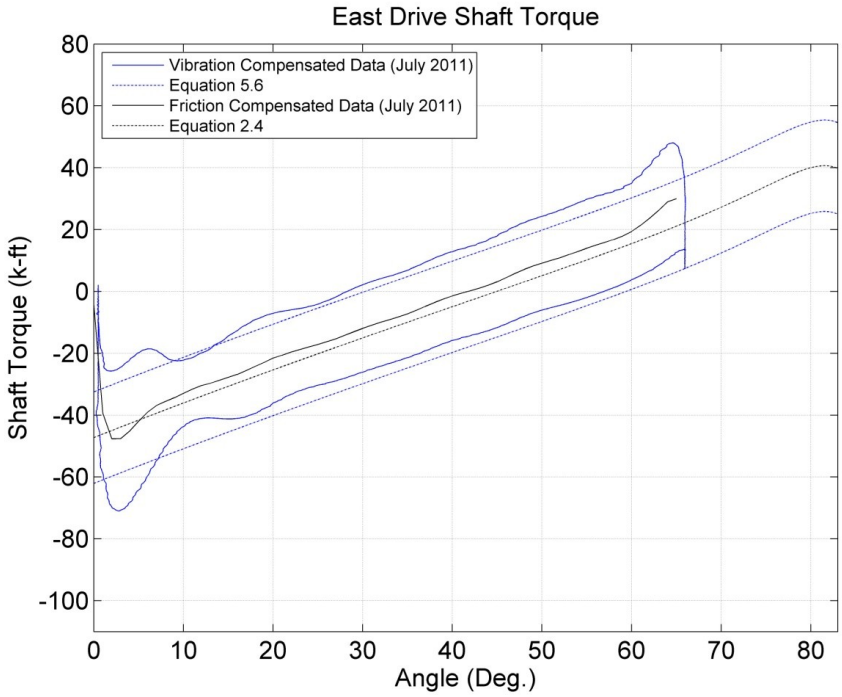

Figure 5.7: Comparison of Vibration Compensated Analytical and Experimental Drive Shaft Torque

5.3 Structural Impairment Detection Results

This section comments on results obtained from comparisons of nominal, impaired, and observed data streams from the Salmon Bay Bridge. Observations from impairment detection and classification performed with trained neural arrays are discussed.

5.3.1 Structural Impairment Data Streams

SAP2000 and ABAQUS models vary significantly in their capability to represent impairments. Figures 4.9 and 4.10 illustrate the inability of SAP2000 frame elements to capture partial section loss over a 0.1 in. region. A reduction in area of a short impaired frame element will produce significantly different stresses locally at the reduction, but the overall deformation of the member to which the impaired element belongs remains

relatively unaffected. This behavior becomes apparent when considering a simply supported beam loaded at midspan with a short portion of reduced area in the middle. Moment distribution, maximum bending stress along the beam, and deflection are illustrated in Figure 5.8.

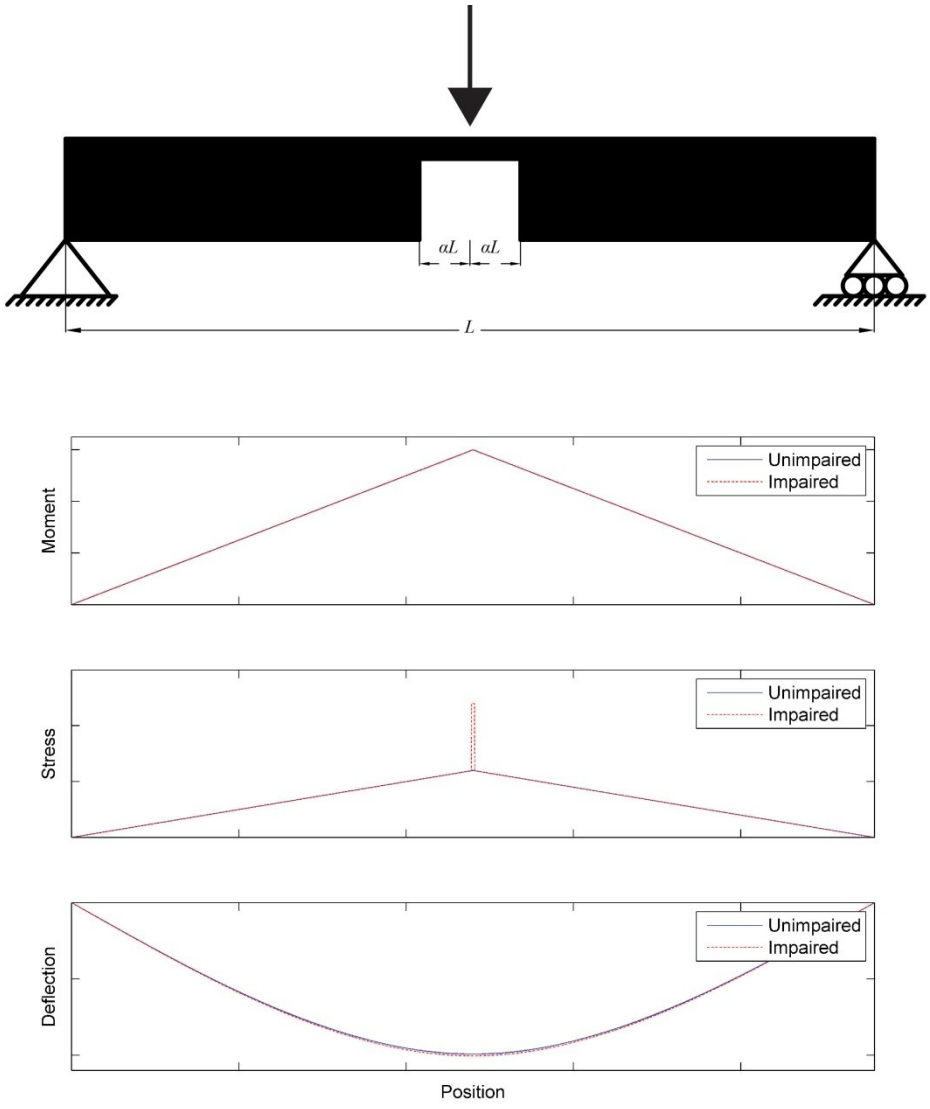

Figure 5.8: Behavior of Impaired Frame Member

Bending stress increases sharply at the reduced section, but the overall deflection is relatively unchanged. Moment area theorems illustrate the effect of a short, reduced section on deflection. The moment area theorem states that the difference between two tangents to the deflection curve can be found by finding the first moment of the bending moment curve. Symmetry implies that the slope at midspan is zero, and thus the deflection at midspan can be found through the moment area expression in Equation 5.7.

$$\Delta_{\mathrm{C}} = \int_0^{\frac{L}{2}} x \frac{M(x)}{EI} dx \tag{5.7}$$

Specifically for the beam in Figure 5.8,

$$\Delta_C = \int_0^{\frac{L}{2}-\alpha L} \frac{Px^2}{2(EI)_{\mathrm{FULL}}} dx + \int_{\frac{L}{2}-\alpha L}^{\frac{L}{2}} \frac{Px^2}{2(EI)_{\mathrm{PARTIAL}}} dx \tag{5.8}$$

If $n_{(EI)}$ defines the ratio of full EI_{FULL} to partial $EI_{PARTIAL}$, then the equation for the maximum deflection reduces to

$$\Delta_{\mathrm{C}} = \frac{PL^3}{48(EI)_{\mathrm{FULL}}} \left[4(1-2\alpha)^3\left(1-n_{(\mathrm{EI})}\right) + n_{(\mathrm{EI})}\right] \tag{5.9}$$

Normalizing Equation 5.9 by dividing by the unimpaired deflection gives

$$\frac{\Delta_{\mathrm{C}}}{\Delta_{\mathrm{FULL}}} = \left[4(1-2\alpha)^3\left(1-n_{(\mathrm{EI})}\right) + n_{(\mathrm{EI})}\right] \tag{5.10}$$

Figure 5.9 displays a normalized deflection in Equation 5.10 for various values of $n_{(\mathrm{EI})}$.

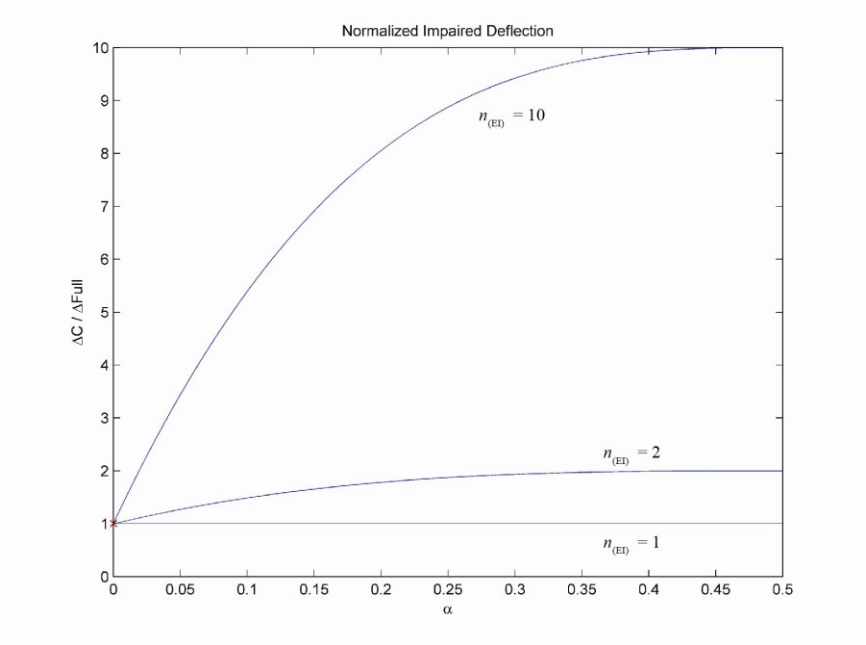

Figure 5.9: Normalized Deflection of Simple Beam with an Impaired Section

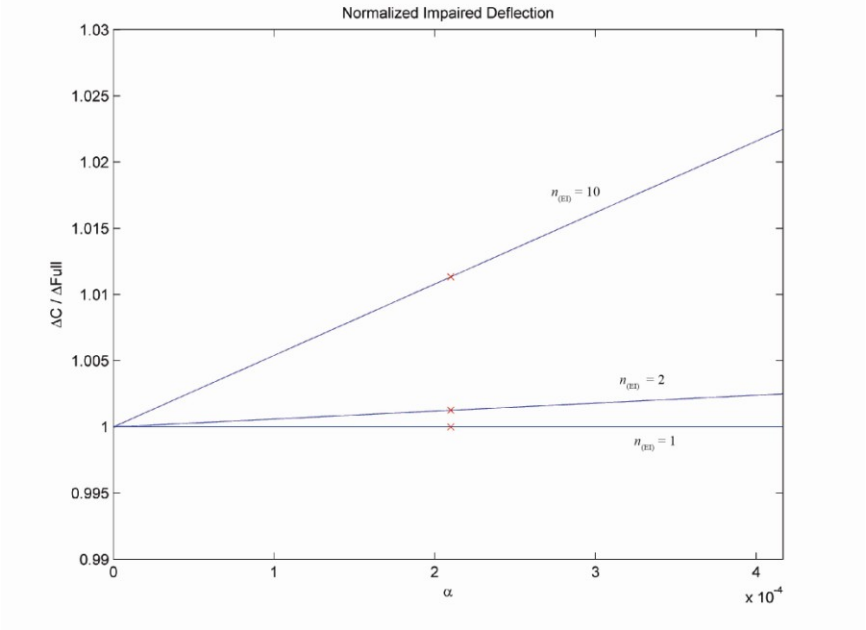

Figure 5.10: Region of Applicability of Equation 5.10 in SAP2000 Analyses

Figure 5.10 illustrates that for small values of α_0 (such as ~0.0002 for SAP2000 models), this result is close to unity and signifies little change in deflection from the fully intact section result. Such small changes in deflection result in small changes in calculated load effects. Dramatic changes in the geometry of finite element models can produce ill-conditioned stiffness matrices and erroneous results. To ensure valid results, an analysis was carried out in which all short impairment members were assigned full section values. The results from analyses with and without short, full section properties yielded identical results; no numerical errors were encountered while examining SAP2000 results.

Fully reducing the section of a short impairment frame element is akin to changing the boundary conditions of the problem, and the results from this scenario are significantly different from the results of an unimpaired condition. Owing to these behaviors of frame elements, SAP2000 was used only in creating data streams representing full section loss.

Figures 4.11 and 4.12 depict impaired and unimpaired data streams from ABAQUS results using shell elements to represent built-up main counterweight truss members. Shell elements comprise the main counterweight chords and explicitly model the built up components of the member including diaphragm, webs, flange, and tie plates.

Instead of estimating cross sectional properties for a frame element, the detailed member components and thicknesses of structural plates were modeled explicitly in ABAQUS. The deflection profile of the main chord also varies dramatically in a frame member and a built-up shell cross section. Each component of a cross section modeled with shells can deform independently of another; in a frame member, the entire cross section deflects the same amount at any location along the member. The refinement from frame elements in SAP2000 to shell elements in ABAQUS allows for the modeling of more subtle impairment scenarios such as partial section reduction. Results from a partial reduction of the main member section were noticeably different from unimpaired results. Neural networks require data streams representing different classification regimes to be unique. The refinement in geometry and subsequent improved impairment data streams resulting from ABAQUS analyses provided unique, representative, and realistic classification signatures on which neural network arrays could be trained. For this reason, ABAQUS data streams were chosen as the primary training data for structural impairment detection algorithms. Neural networks trained on both ABAQUS and SAP2000 data streams

5.3.2 Impairment Detection of Observed and Simulated Salmon Bay Bridge Data

Presenting data streams from a typical opening of the Salmon Bay Bridge results in one of two diagnoses: I.C. 1 (unimpaired) and I.C. 14 (impaired embedded member at 33 E). Figure 5.11 illustrates the I.C. 14 which represents the fracture of the embedded counterweight leg at 33E.

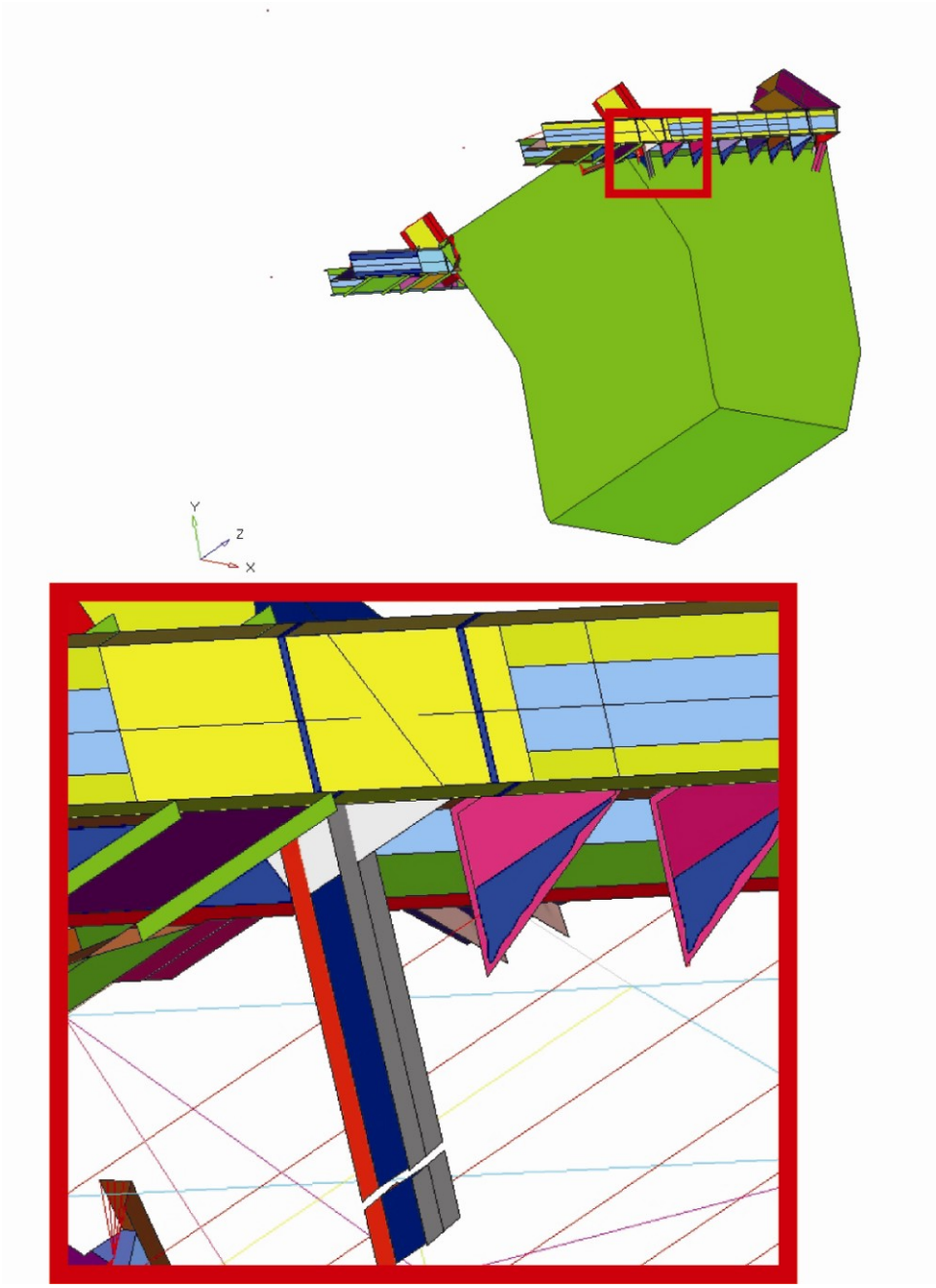

Figure 5.11: Impairment Case 14

Figure 5.12 compares data streams at 60 degrees for I.C. 1, I.C. 14, and the Salmon Bay Bridge testbed in July 2011. Upon a visual inspection of Figure 5.12, the Salmon Bay data streams resemble both I.C.1 and I.C. 14 for most transducers. Figure 5.12 illustrates the difficulty faced by a neural network classification algorithm, and explains why the I.C. 14 classification is often produced in testbed diagnoses. Based on modeled impairments, it is likely that the Salmon Bay Bridge was operating nominally, but that an impairment of some unknown degree may have been present at joint 33E.

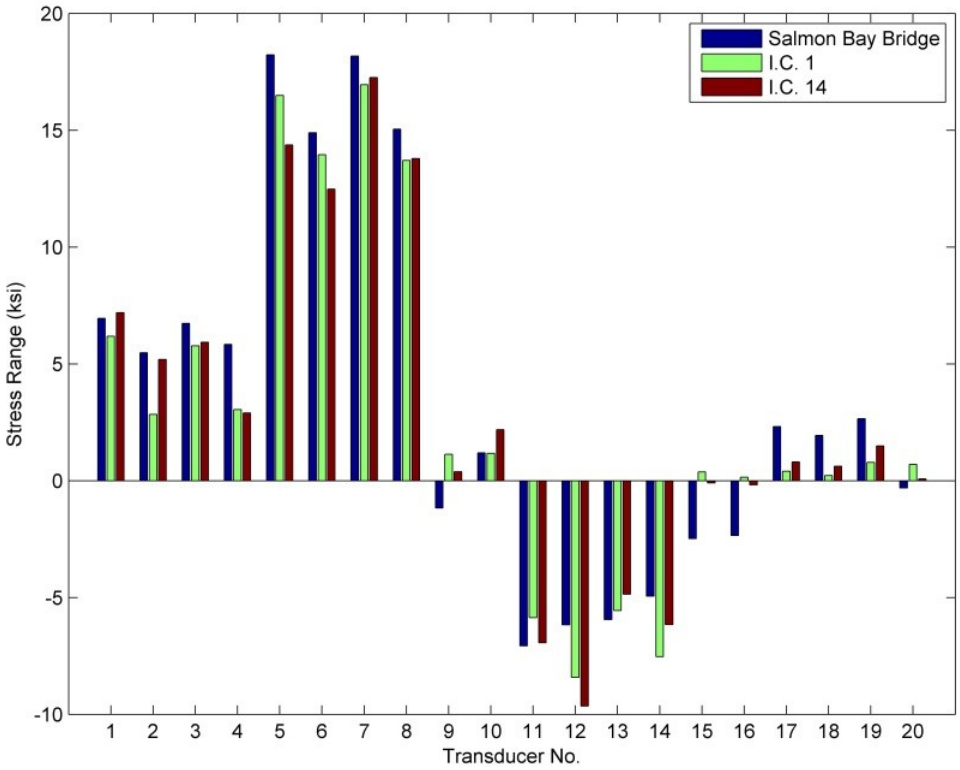

Figure 5.12: 60 Degree Opening Data Streams for I.C.1, I.C. 14, and the Salmon Bay Bridge

One issue that arose in the evaluation of testbed data was the effect of malfunctioning transducers on the data streams and thus impairment detection algorithms. Initially, neural algorithms were trained on data streams consisting of responses from fully functioning transducers; Table 5.1 displays the output from these networks for Salmon Bay Bridge openings throughout the monitoring effort.

Table 5.1: Impairment Case Classification without Malfunctioning Transducer Information

Angle of Opening (Deg.)	Nov. 2009	Mar. 2010	July 2010	Nov. 2010	Mar. 2011	July 2011	Nov. 2011
10	14	14	14	1	6	14	14
20	14	14	1	1	6	14	14
30	1	1	1	1	6	1	1
40	1	1	1	1	6	1	1
50	1	n/a	1	1	6	1	1
60	1	n/a	1	1	6	1	n/a
70	14	n/a	1	14	n/a	n/a	n/a

Results from March 2011 indicate that the bridge was operating under I.C. 6 (partial section loss at 33W). A close examination of the data from that opening revealed that two transducers (one near joint 33W) were malfunctioning. Figure 5.13 displays visual representations of the data streams from March 2011 and July 2011. Transducers 7 and 15 were reporting zero strain for all angles of opening. When functioning, transducer 7 reported stress ranges up to 20 ksi. The data streams from March 2011 and July 2011 look significantly different with abrupt drops to zero stress range for transducers 7 and 15 in March. An array of neural networks trained only on fully functioning, complete data mistakenly reported an impairment case most closely resembling the data stream featuring the erroneous data.

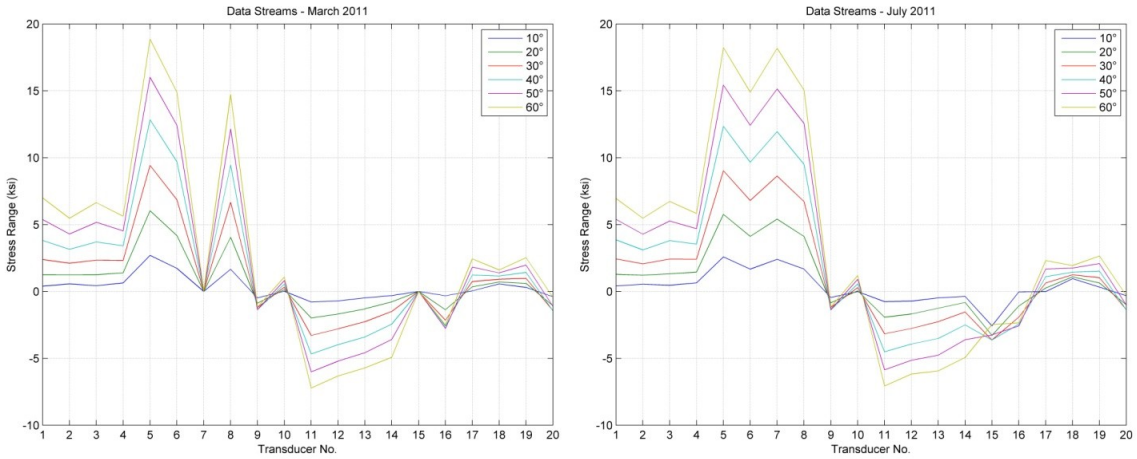

Figure 5.13: Data Streams from March 2011 and July 2011

Final neural network arrays were trained with fully functioning data and data representing up to three randomly assigned malfunctioning transducers. A system in which multiple transducers are malfunctioning has less diagnostic capability. Some indication of transducer integrity is necessary to avoid incorrect diagnoses.

Results from the detection efforts of a mock SIDS on simulated bridge data were conclusive. In each simulated opening, a report was produced and successfully detected all simulated impairments.

5.4 Future Work

The results of this dissertation study were produced from methodical efforts consistently focused on developing both an applicable SIDS, as well as a general, logical methodology for developing such a system. Opportunities for additional refinements and improvements exist.

Several likely impairments specific to the Salmon Bay Bridge testbed structure were represented in analytical models, and these models were used to produce data streams on which to train competitive neural algorithms. While the selection and representation of the presented modeled impairments were sound, data streams resulting

from physical experiments on impaired specimens would be beneficial. Such data would provide premium data streams for neural network training, impaired model validation, or improvement. This type of impairment data would benefit the development of a SIDS on any structure or mechanical system. In the case of studying the impairment of a bascule bridge, one area of further investigation is the effect of concrete/steel interaction on the global structure. Generally, a threshold of detectable impairments and their classifications could be developed for a specific structure and specific impairments.

Another feature of an impairment detection system that could be improved is the event log structure and report structure for a SIDS. An event log is defined as information saved from a specific defined event, and a report is some communication to a decision maker such as a bridge engineer or researcher. Some variables concerning this feature are report frequency, report content, and report delivery method; additionally, event log specifications and report log specifications should likely be considered separately. For the case of the Salmon Bay Bridge testbed, the event log frequency was well defined as an opening/closing event. Data from each event was saved and analyzed by SIDS software which produced an event log. Not every event warrants a report to a decision maker. In fact, too many reports may reduce the effectiveness of a SIDS; too much information increases the likelihood that important information is unnoticed or ignored.

Tailoring a SIDS to a specific structure necessitates tailoring a report structure. In general, different structures may have more ambiguous event and report frequencies than the Salmon Bay Bascule Bridge. Professional expertise by practicing engineers is essential in determining the parameters of a successful SIDS report.

CHAPTER VI
CONCLUSIONS

Research completed during the development of a Structural Impairment Detection System on the Salmon Bay Bridge testbed resulted in several relevant conclusions concerning the development of competitive neural network algorithms, implementation of a structural impairment detection system on the Salmon Bay Bridge testbed, and general analysis of heel trunnion bascule bridges.

6.1 Competitive Artificial Neural Networks for Structural Impairment Detection

- Competitive arrays of artificial neural networks outperformed individual neural networks. Performance was increased by providing an array of networks with varying architectures rather than forcing a single network architecture to develop needed relationships.
- Neural impairment detection algorithms benefit from training data that is sensitive to specific impairments.
- A series of static neural networks responsible for impairment detection for a series of angles of opening is suitable for the implementation of a SIDS on a bascule bridge.
- Competitive neural impairment detection algorithms benefit from training data streams representing structural impairments and instances of transducer malfunction. Classifications resulting from such algorithms are less affected by imperfect data streams.
- The evaluation of orthogonality characteristics of simulated result vectors is a successful competitive error measure.

6.2 Implementation of a SIDS on the Salmon Bay Bridge Testbed

- Bascule bridges are well suited as experimental testbeds. Features such as a power source, internet access, and data acquisition shelter are conducive to monitoring efforts. Openings and closings provide frequent, reproducible excitation useful in evaluating the bridge's performance.
- The instrumentation program designed, produced, and implemented is capable, with infrequent maintenance, of autonomously recording data streams for use in structural impairment detection.
- Based on results from neural algorithms, the Salmon Bay Bridge produced data streams similar to one of two operational conditions: unimpaired or impairment to an embedded member at the southeast corner of the counterweight.

6.3 Modeling and Behavior of the Salmon Bay Bridge

- Torque values in the drives shafts are extremely sensitive to weights and bridge component centers of gravity.
- The tendency of the bridge to open or close is dependent on its angle of opening.
- Dynamic inertial effects of the Salmon Bay Bridge operating under normal conditions are small. Static finite element models are sufficient to estimate essential features of the structural behavior.
- Counterweight truss members of the Salmon Bay Bridge experience significant stress ranges that may be accurately represented by a series of static finite element models.
- Increased differences in stress range between east and west flanges of both main chords of the counterweight truss have occurred since 1952.
- Increased refinement in finite element models improves the accuracy of modeling of the main chords of the counterweight truss. Modeling the main chords with shell elements, rather than beam elements, more accurately captures

the behavior of individual member flanges. Increasingly refined analysis facilitates the modeling of increasingly subtle impairment.

- Bracing members in the counterweight truss are sensitive to the presence of modeled impairments.

REFERENCES

AAR (2008). "Railroad Facts", Association of American Railroads, Office of Information and Public Affairs, Washington, D.C.

ABAQUS (2011). Version 6.9. Providence, RI: SIMULIA.

Alwash, M.B. (2010). "Excitation Sources for Structural Health Monitoring of Bridges," Ph.D. Dissertation, Univ. of Saskatchewan, Saskatoon, Canada.

Barai, S.V. and Pandey, P.C. (1997). "Time-Delay Networks in Damage Detection of Railway Bridges," *Adv. in Engr. Software* 28, 1-10.

Beckwith, T.G., Marangoni, R.D., Lienhard V, J.H. (1995). *Mechanical Measurements*, Addison-Wesley Publishing Co., New York, NY.

Bishop, C.M. (1994). "Neural Networks and Their Applications," *Rev. Sci. Instrum.* 65 (6), 1803-1832.

BNSF (2007). Bridge 6.3 Fact Sheet. Burlington Northern Santa Fe Railroad, Unpublished.

BNSF (1952). "Great Northern Railway Br. 4-Salmon Bay Bridge," Internal Report of Instrumentation Results from 1952 Monitoring Effort, Burlington Northern Santa Fe Railroad.

Catbas, F.N., Mustafa, G., Zaurin, R., Terrell, T., Dere, Y., Ansley, M.H., Frangopol, D.M., and Grimmelsman, K.A. (2009). "Structural Health Monitoring of Bridges: Fundamentals, Appplication Case Study and Organizational Considerations," *Proc., Structures Congress*, ASCE, Austin, TX, 108-118.

Chang, C.C., Chang, T.Y.P. and Xu,Y.G. (2000). "Structural Damage Detection Using an Iterative Neural Network ," *J. of Intelligent Mat. Sys.and Struct.,* 11, 32-42.

Chopra, A.K. (2001). *Dynamics of Structures.* Prentice Hall, Upper Saddle River, NJ.

DelGrego, M.R., Culmo, M.P., and DeWolf, J.T. (2008). "Performance Evaluation through Field Testing of Century-Old Truss Bridge," *J. Bridge Engr.,* 13(2), 132-138.

Doebling, S. W., Farrar, C.R., and Prime, M. B. (1997). "A Summary Review of Vibration-Based Damage Identification Methods," Technical Report, Los Alamos National Laboratory.

EPC (2009). "Model Tr1 – Tru-Trac™," Datasheet, Sagle, ID: Encoder Products Company.

Fang, X., Luo, H. and Tang, J. (2005). "Structural Damage Detection Using Neural Network with Learning Rate Improvement," *Comp. and Struct*., 83, 2150-2161.

Fausett, L. (1994), *Fundamentals of Neural Networks,* Prentice Hall, Englewood Cliffs, NJ.

FHWA (2009). "Deficient Bridges by State and Highway System," Federal Highway Administration, Office of Bridge Technology.

FRA (2010). "Bridge Safety Standards," Final Rule, Federal Railroad Administration, Washington D.C.

Frýba, L. (1996). *Dynamics of Railway Bridges*, T. Telford, London.

Graydon, E.R. (1949). "Counterweight Replacement on the Cherry Street Bascule Bridge." *The Engr. J*., 32(3), 126-129.

Hagan, H.T., Demuth, H.B., and Beale, M. (1996). *Neural Network Design*, PWS Publishing Co., Boston, MA.

Hambley, A.R. (2005). *Electrical Engineering*, Pearson Education, Inc., Upper Saddle River, NJ.

Haykin, S. (1999). *Neural Networks*, Macmillian Publishing Co., Englewood Cliffs, NJ.

Hool, G.A., and Kinne, W.S. (1923). *Moveable and Long-Span Steel Bridges*, McGraw-Hill Book Company, Inc., New York, NY.

Hovey, O.E. (1926). *Movable Bridges*, J. Wiley & Sons, Inc., New York, NY.

Hyland, D.C. and Davis, L.D. (2002). "Toward Self-Reliant Control for Adaptive Structures," *Acta Astronautica* 51(1-9), 89-99.

Hyland, D.C. and Fry, G.T. (1999). "A Neural-Genetic Hybrid Approach for Optimizing Structural Health Monitoring Systems," *Proc. 2nd Int. Workshop on Structural Health Monitoring*, Stanford, CA., pp. 800-811.

Hyland, D.C. and King, J.A. (1992). "Neural Network Architectures for Stable Adaptive Control, Rapid Fault Detection and Control System Recovery," *Proc,. 15th Annual AAS Guidance and Control Conference*, Keystone, CO.

Hypermesh (2011). Version 10. Troy, MI: Altair.

IOTech (2005). StrainBook/616 User's Manual, Cleveland, OH: IOTech.

Kamen, E.W., and Heck, B.S.(2000). *Fundamentals of Signals and Systems*, : Prentice Hall,Inc., Upper Saddle River, NJ.

Ketchum, M.S. (1914). *Structural Engineers' Handbook*, McGraw-Hill Book Company, Inc., New York, NY.

Koglin, T.L. (2003). *Movable Bridge Engineering*, John Wiley & Sons, Inc., Hoboken, NJ.

Kortesis, S., and Panagiotopoulos, P.D. (1993). "Neural Networks for Computing in Structural Analysis: Methods and Prospects of Applications." *Int. J. for Num. Meth. in Engr.,* 36, 2305-2318.

Lee, J.W., Kirikera, G.R., Kang, I., Schulz, M.J., Shanov, V.N. (2006). "Structural Health Monitoring Using Continuous Sensors and Neural Network Analysis." *Smart Mat.and Struct.,* 15, 1266-1274.

Leighty III, C.A., Laman, J.A., and Gittings, G.L., (2004). "Heavy Axle Study: Impact of Higher Rail Car Weight Limits on Short-Line Railroad Bridge Structures," *Civil Engr. and Envirn. Sys.,* 21(2), 91-104.

Li, H.N., Sun, H.M., and Song, G. B. (2004). "Damage Diagnosis of Framework Structure Based on Wavelet Packer Analysis and Neural Network," *Smart Struct. and Mat.,* 533-542.

Liu, M., Frangopol, D.M., Kim, S. (2009). "Bridge System Assessment from Structural Health Monitoring: A Case Study," *J. Struct. Engr.,* 135(6), 733-742.

Malvern, L.E., Lu, S.Y., and Jenkins, D.A. (1985). "Bascule Bridge Balancing and Diagnostic Techniques," Final Report, State of FL Department of Transportation.

MATLAB (2010). Version 7.10. Natick, MA: The MathWorks Inc.

Minsky, M.L., and Papert, S.A. (1969). Perceptrons. MIT Press, Cambridge, MA.

Paine, C.E. (1929). "Analysis of Dynamic Stresses in Hackensack Bascule." *Engineering News Record*, 103(9), 340-344.

Pandey, P.C., and Barai, S.V. (1995). "Multilayer Perceptron In Damage Detection of Bridge Structures." *Comp. and Struct.,* 54(4), 597-608.

Penny and Giles (2010). "SST280 Sealed Tilt Sensor," Technical Specifications, City of Industry, CA: Penny and Giles.

Reichmann, A. (1924). "American Bridge Type Bascule Bridge." *J. of the Western Society of Engineers*, 24(9), 177-181.

Rosenblatt, F. (1958). "The Perceptron: A Probabilistic Model for Information Storage and Organization of the Brain." Psych. Rev. 654, 386-408.

Rumelhart, D.E., and Mclleland, J.L. (1986). Parallel Distributed Processing: Explorations in the Microstructure of Cognition, Vol. 1. MIT Press, Cambridge, MA.

Rytter, A. (1993). "Vibration Based Inspection of Civil Engineering Structures," Ph. D. Dissertation, Aalborg University, Denmark.

Salawu, O. S. (1997). "Detection of Structural Damage Through Changes in Frequency: A Review," *Engr. Struct*., 19(9), 718-723.

SAP2000 (2010). Version 14.0.0 Berkely, California: Computers and Structures Inc.

Sohn, H., Farrar, C.R., Hemez, F.M., Shunk, D.D., Stinemates, D.W., Nadler, B.R., and Czarnecki, J.J. (2001). "A Review of Structural Health Monitoring Literature: 1996–2001," Technical Report, Los Alamos National Laboratory.

SolidWorks (2006). Version 2006 SP4.1. Concord, MA: SolidWorks Corporation.

Soyoz, S. and Feng, Q. (2005). "Instantaneous Damage Detection of Bridge Structures and
Experimental Verification," *Struct. Control Health Monit*., 15, 958–973.

Wallner, M. And Pircher, M. (2007). "Kinematics of Movable Bridges," *J.of Bridge Engr*., 12(2),147-153.

Weatherford, B.A., Willis, H. H., Ortiz, D. S. (2008). "The State of U.S. Railroads: A Review of Capacity and Performance Data," Technical Report, Rand Corporation, Santa Monica, CA.

Wilson, W.M. (1948). "Report on the Failure of Bascule Bridge No. 4 of the Great Northern Railway at Ballard, Washington," Technical Report for Great Northern Railroad.

Yeung, W.T., and Smith, J.W. (2000). "Damage Detection in Bridges Using Neural Networks for Pattern Recognition of Vibration Signatures," *J. Engr. Struct*., 27, 685-698.

APPENDIX A
DRIVE SHAFT ANALYSIS

Chapter II presents an idealized model of a Strauss Heel Trunnion Bascule bridge used in developing an estimate of drive shaft torque as a function of angle of opening. This appendix outlines the detailed derivation of Equation 2.6. Figure A.1 depicts a schematic of the bridge and its corresponding idealization, including boundaries for three free body diagrams (FBD) for the development of a simple torque model. Free body diagrams of the counterweight frame, leaf, and operating strut were analyzed to determine the behavior of the drive shafts.

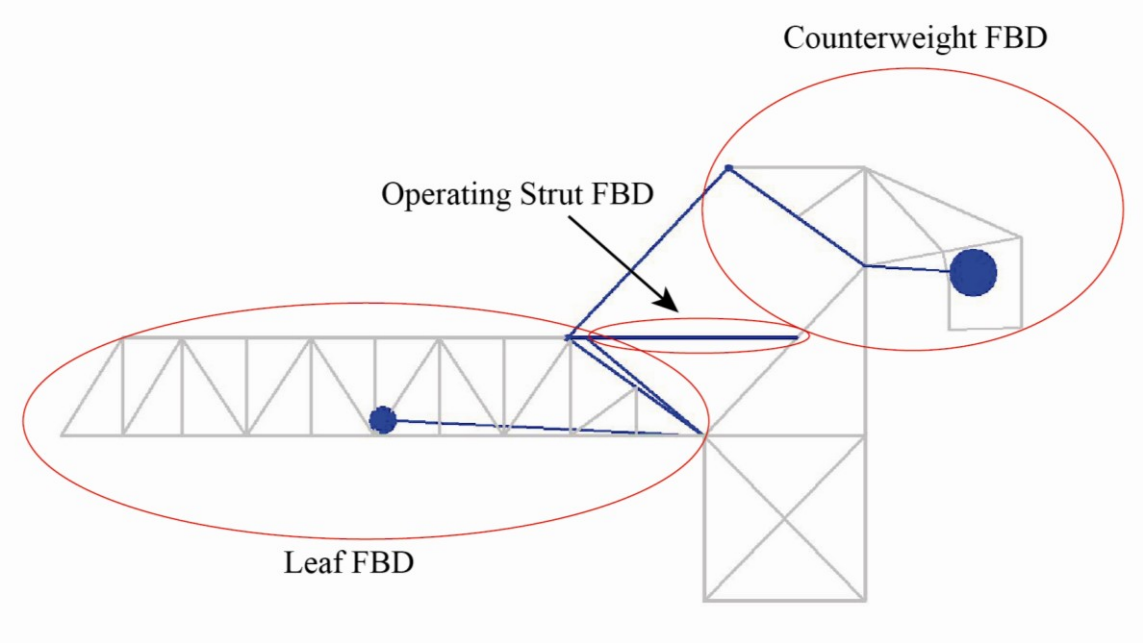

Figure A.1: Idealized Model for Torque Analysis with Free Body Diagram Boundaries

Figure A.2 illustrates the FBD of the counterweight open at an angle of θ. Blue components represent the deformed shape while gray components represent the original positions. The forces acting on the counterweight FBD are the axial link force, reactions at the trunnion pin, and the combined weights of the counterweight, counterweight truss, and half of the link weight.

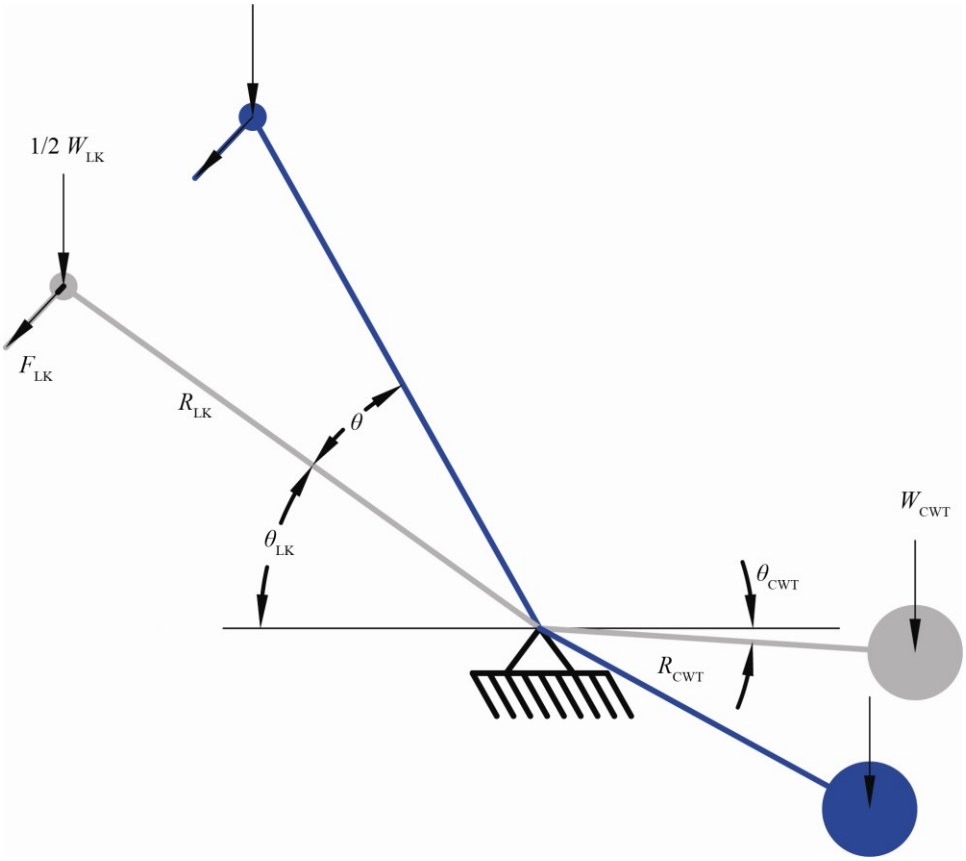

Figure A.2: FBD of Counterweight Truss

Summing moments about the pin in Figure A.2 results in the following expression for moment caused by the force in the link, M_{LK}

$$M_{LK} = W_{\mathrm{CWT}} R_{\mathrm{CWT}} \cos(\theta_{\mathrm{CWT}} + \theta) + - \frac{W_{\mathrm{LK}}}{2} R_{\mathrm{LK}} \cos(\theta_{\mathrm{LK}} + \theta) \qquad \text{(A.1)}$$

For any desired numerical value of the angle θ, Equation A.1 produces a numerical value for M_{LK}; the force in the link can also be calculated from M_{LK} as 1156 k, which is within 2.5% of the values calculated from statics and SAP2000 in Tables 2.3 and 2.4 of Chapter II.

Figure A.3 illustrates forces acting on a FBD of the leaf. Forces include reactions at the main heel trunnion, the weight of the leaf, one half the weight of the counterweight links, the axial force in the counterweight links, and reactions from the operating strut pin.

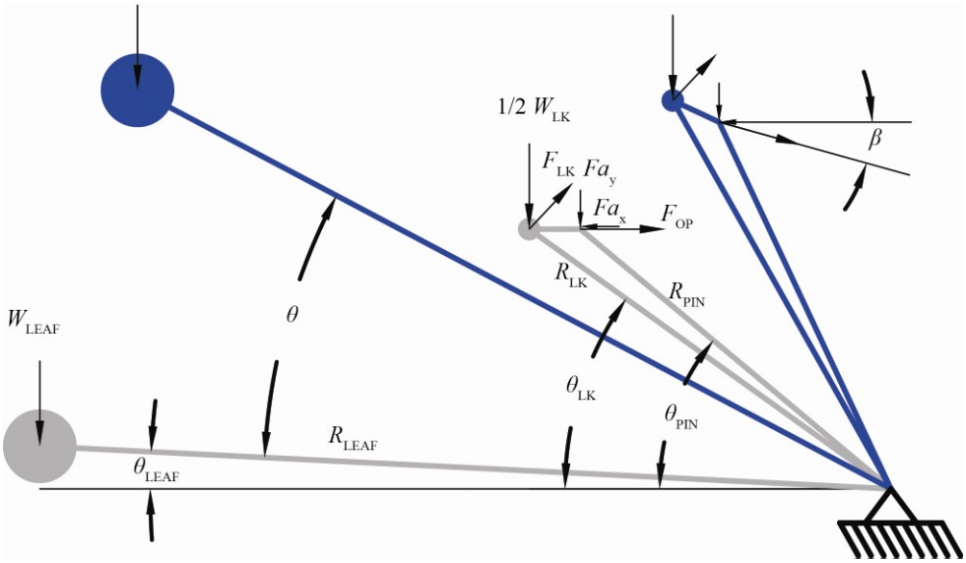

Figure A.3: FBD of Leaf

The summation of moments from forces acting on the leaf about the pin in Figure A.3 yields the following equation

$$W_{\mathrm{LEAF}}R_{\mathrm{LEAF}}\cos(\theta_{\mathrm{LEAF}}+\theta)+\frac{W_{\mathrm{LK}}}{2}R_{\mathrm{LK}}\cos(\theta_{\mathrm{LK}}+\theta)$$
$$+Fa_{\mathrm{y}}R_{\mathrm{PIN}}\cos(\theta_{\mathrm{PIN}}+\theta)+Fa_{\mathrm{x}}R_{\mathrm{PIN}}\sin(\theta_{\mathrm{PIN}}+\theta) \quad \text{(A.2)}$$
$$-M_{\mathrm{LK}}-M_{\mathrm{OP}}=0$$

The moment caused by the axial force in the operating strut, M_{OP}, is of interest because the axial force transferred through the operating strut to the pinions creates torque in the drive shafts. Equation A.3 relates the moment about the main trunnion caused by the operating strut axial force in terms of the axial force in one operating strut

$$\left|\vec{M}_{\mathrm{OP}}\right|=\left|\vec{R}_{\mathrm{PIN}}\times\vec{F}_{\mathrm{OP}}\right|=2F_{\mathrm{OP}}R_{\mathrm{PIN}}\sin(\theta_{\mathrm{PIN}}+\theta-\beta) \quad \text{(A.3)}$$

The factor of two indicates that the total moment is the product of the moment coming from both the east and west operating struts.

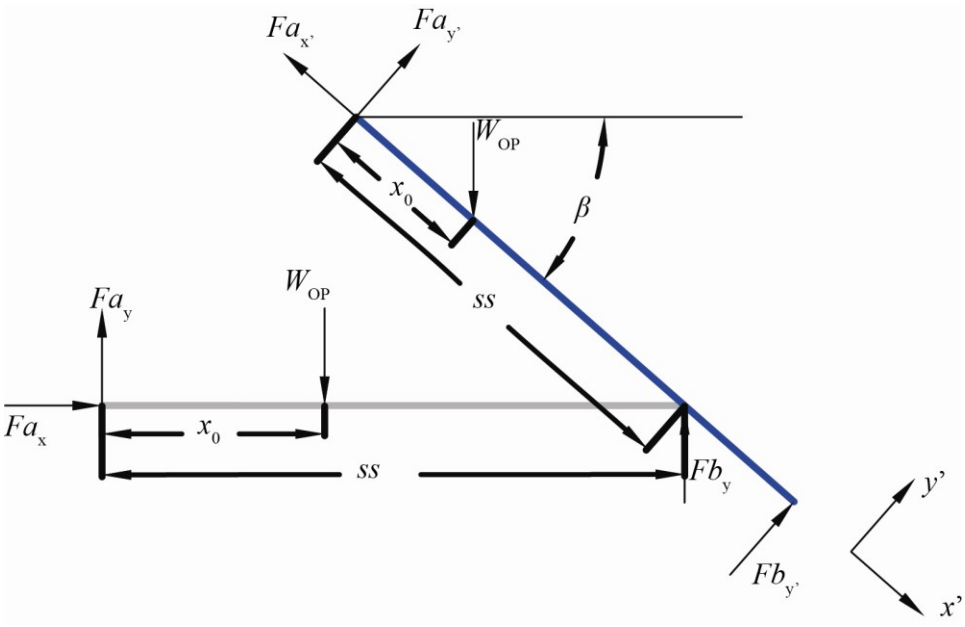

Figure A.4: FBD of Operating Strut

Equation A.2 also contains terms including the reaction forces resulting from the self weight of the operating strut. Figure A.4 illustrates a FBD used in calculating the reaction forces Fa_x and Fa_y. Statics calculations of the reactions shown in Figure A.4 result in the following expressions

$$Fa_x{}' = W_{OP}\sin\beta \tag{A.4}$$

$$Fa_y{}' = W_{OP}\cos\beta\,\frac{(ss - x_0)}{ss} \tag{A.5}$$

A coordinate transformation yields expressions for Fa_x and Fa_y

$$Fa_x = -W_{OP}\sin\beta\cos\beta + W_{OP}\sin\beta\cos\beta\,\frac{(ss - x_0)}{ss} \tag{A.6}$$

$$Fa_y = W_{OP}\sin^2\beta + W_{OP}\cos^2\beta\,\frac{(ss - x_0)}{ss} \tag{A.7}$$

In the preceding equations, the angle β is a function of θ which can be expressed from the geometry in Figure A.3 as

$$\beta = \operatorname{atan}\left[\frac{R_{PIN}\sin(\theta + \theta_{PIN}) - R_{PIN}\sin(\theta_{PIN})}{R_{PIN}\cos(\theta + \theta_{PIN}) - (x_R)}\right] \tag{A.8}$$

The variable x_R is the horizontal distance between the main heel trunnion and the roller support of the operating strut; x_R is a constant value. An expression for F_{OP} is given in Equation A.9

$$F_{\mathrm{OP}} = \Big[W_{\mathrm{LEAF}} R_{\mathrm{LEAF}} \cos(\theta_{\mathrm{LEAF}} + \theta) + \frac{W_{\mathrm{LK}}}{2} R_{\mathrm{LK}} \cos(\theta_{\mathrm{LK}} + \theta) + Fa_{\mathrm{y}} R_{\mathrm{PIN}} \cos(\theta_{\mathrm{PIN}} + \theta) + Fa_{\mathrm{x}} R_{\mathrm{PIN}} \sin(\theta_{\mathrm{PIN}} + \theta) - M_{\mathrm{LK}} \Big] / [2 R_{\mathrm{PIN}} \sin(\theta_{\mathrm{PIN}} + \theta - \beta)] \quad \text{(A.9)}$$

Where M_{LK}, Fa_{x}, Fa_{y}, and β are given by equations A.1, A.6, A.7, and A.8, respectively. Equation 2.4 defines the drive shaft torque as a function of θ and is repeated

$$T = r_{\mathrm{s}} \Big\{ \Big[W_{\mathrm{LEAF}} R_{\mathrm{LEAF}} \cos(\theta_{\mathrm{LEAF}} + \theta) + \frac{W_{\mathrm{LK}}}{2} R_{\mathrm{LK}} \cos(\theta_{\mathrm{LK}} + \theta) + Fa_{\mathrm{y}} R_{\mathrm{PIN}} \cos(\theta_{\mathrm{PIN}} + \theta) + Fa_{\mathrm{x}} R_{\mathrm{PIN}} \sin(\theta_{\mathrm{PIN}} + \theta) - M_{\mathrm{LK}} \Big] / [2 R_{\mathrm{PIN}} \sin(\theta_{\mathrm{PIN}} + \theta - \beta)] \Big\} \quad \text{(2.4)}$$

APPENDIX B
VIBRATION ANALYSIS OF THE SALMON BAY BRIDGE

Chapter II presents the basis of an analysis for determining the natural frequencies of vibration of the Salmon Bay Bridge testbed. This appendix provides detailed derivations of Equations 2.5 and 2.6. Figure B.1 illustrates the simplified, idealized dynamic model with two rotational degrees of freedom, θ_1 and θ_2, representing rotation about the counterweight trunnion and heel trunnion, respectively. This modeling assumption limits dynamic vibration, at each angle of opening θ_0, to natural frequencies ω_1 and ω_2.

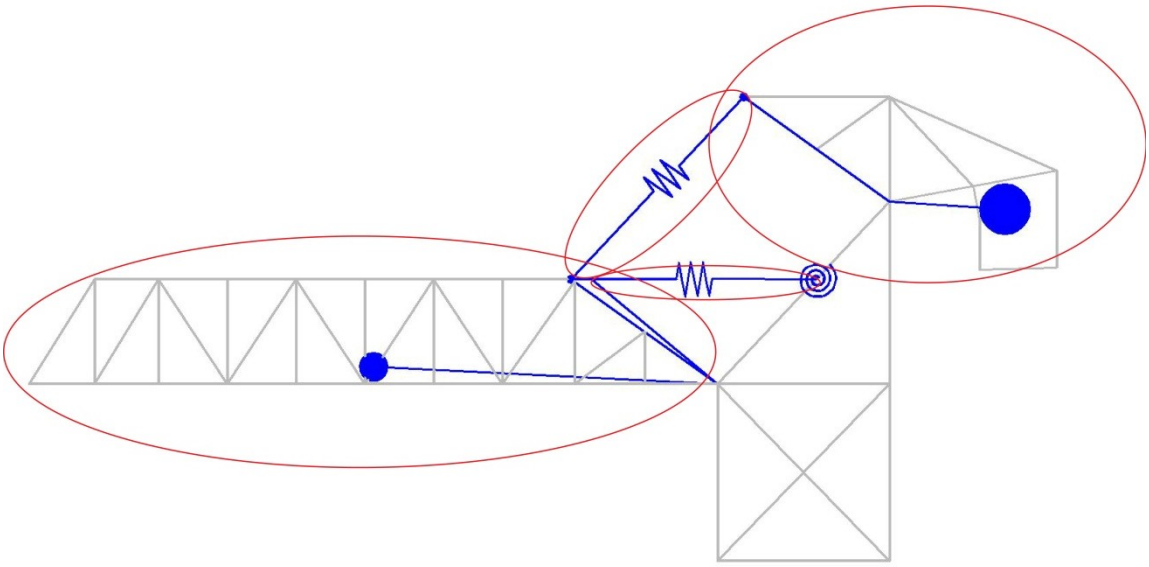

Figure B.1: Idealized Model for Modal Analysis with Free Body Diagram Boundaries

Figure B.2 is a FBD of the counterweight truss. Blue components represent the deformed structure. Forces acting on the counterweight truss are reactions from the pin (counterweight trunnion), the force in the counterweight link, and the self-weight of the

counterweight truss, including the self-weight of the counterweight frame and ½ the counterweight link weight.

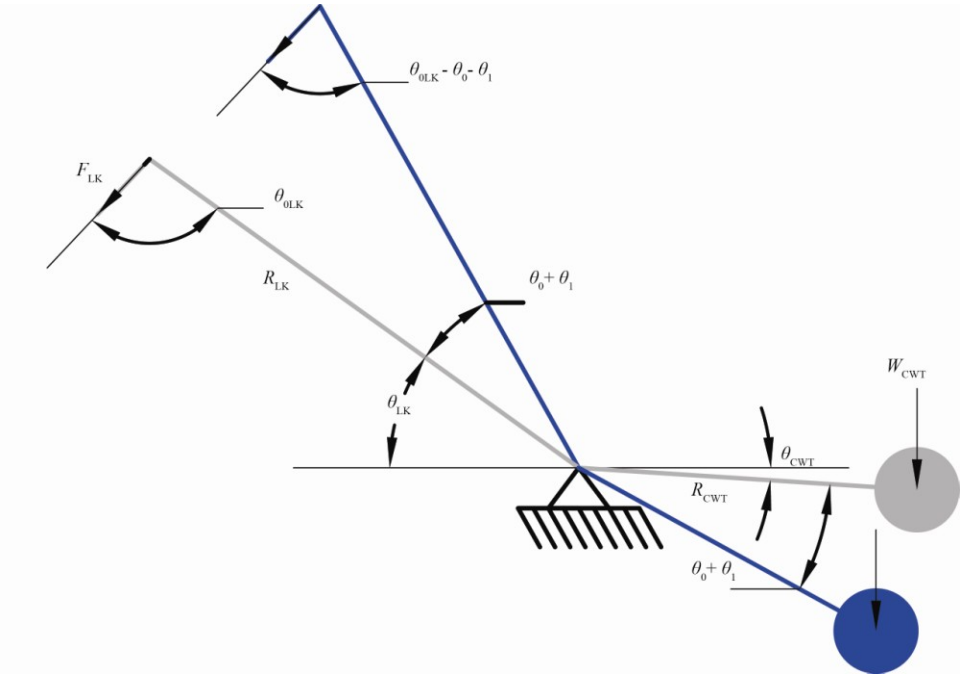

Figure B.2: FBD of Counterweight for Dynamic Analysis

A summation of moments about the counterweight trunnion leads to the following equation

$$I_{\mathrm{CWT}}\ddot{\theta_1} = W_{\mathrm{CWT}}R_{\mathrm{CWT}}\cos(\theta_{\mathrm{CWT}} + \theta_0 + \theta_1) - F_{\mathrm{LK}}R_{\mathrm{LK}}\sin(\theta_{0\mathrm{LK}} - \theta_0 - \theta_1) \quad \text{(B.1)}$$

Equation B.1 may be expressed linearly in terms of θ_1 and θ_2 by using small angle approximations as follows

$$\begin{aligned}
&\cos(\theta_{\mathrm{CWT}} + \theta_0 + \theta_1) \\
&\qquad = \cos\theta_1\ \cos(\theta_{\mathrm{CWT}} + \theta_0) - \sin\theta_1\ \sin(\theta_{\mathrm{CWT}} + \theta_0) \\
&\qquad \approx \cos(\theta_{\mathrm{CWT}} + \theta_0) - \theta_1\ \sin(\theta_{\mathrm{CWT}} + \theta_0) \qquad \text{(B.2)} \\
&\sin(\theta_{0LK} - \theta_0 - \theta_1) = \cos\theta_1\ \sin(\theta_{0\mathrm{LK}} - \theta_0) - \sin\theta_1\ \cos(\theta_{0\mathrm{LK}} - \theta_0) \\
&\qquad \approx \sin(\theta_{0\mathrm{LK}} - \theta_0) - \theta_1\ \cos(\theta_{0\mathrm{LK}} - \theta_0)
\end{aligned}$$

Because the counterweight link is modeled as a spring, the axial force in the link is a function of link stiffness and rotations θ_1 and θ_2. The extension of the counterweight link spring, δ_{LK}, is illustrated in Figure B.3.

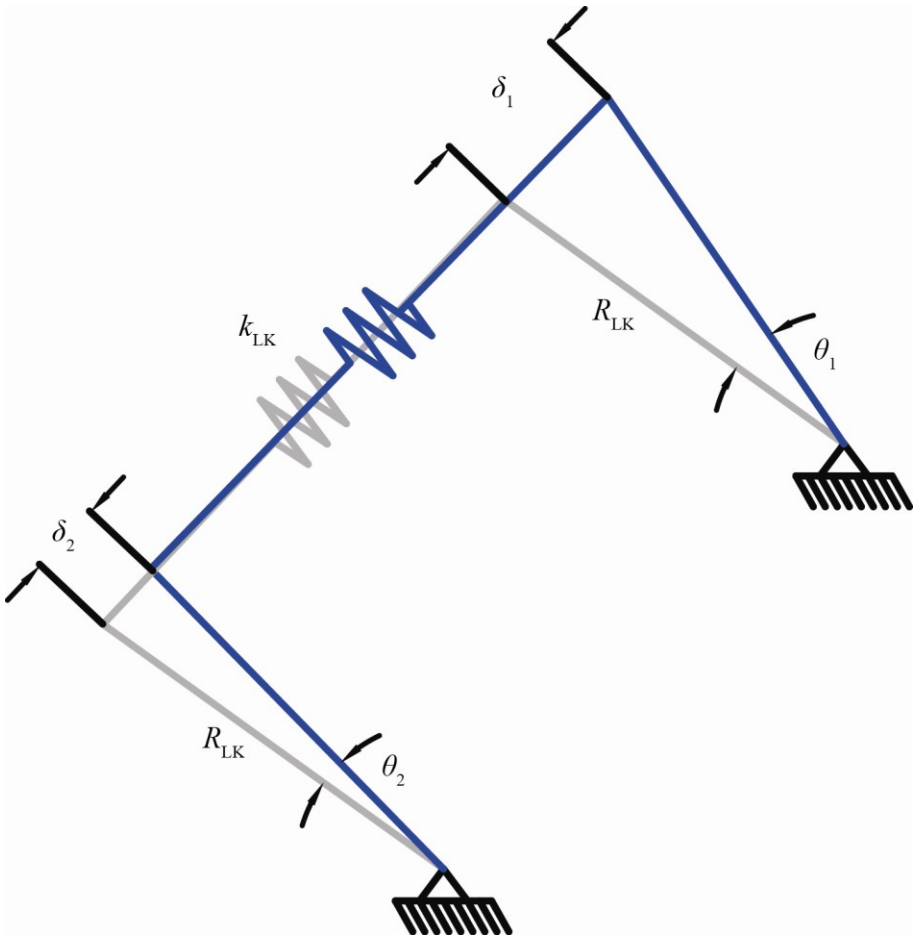

Figure B.3: FBD of Counterweight Link for Dynamic Analysis

The displacement of the counterweight end of the link is assumed to be greater than the displacement at the leaf end. Equations B.3 summarize the pertinent counterweight link displacements with small angle approximations employed for both θ_1 and θ_2

$$\begin{aligned} \delta_1 &\approx R_{\mathrm{LK}}\theta_1, \\ \delta_2 &\approx R_{\mathrm{LF}}\theta_2, \\ \delta_{\mathrm{LK}} \approx \delta_1 - \delta_2 &= R_{\mathrm{LK}}(\theta_1 - \theta_2) \end{aligned} \tag{B.3}$$

The force in the counterweight link is

$$F_{\mathrm{LK}} = k_{\mathrm{LK}}\delta_{\mathrm{LK}} = k_{\mathrm{LK}}R_{\mathrm{LK}}(\theta_1 - \theta_2) \tag{B.4}$$

Combining Equations B.1, B.2, B.3, and B.4 and neglecting products of small angles θ_1 and θ_2 results in the first EOM of the dynamic system

$$\begin{aligned} I_{\mathrm{CWT}}\ddot{\theta_1} + \big[W_{\mathrm{CWT}}R_{\mathrm{CWT}}\theta_1 \ &\sin(\theta_{\mathrm{CWT}} + \theta_0) \\ &+ k_{\mathrm{LK}}{R_{\mathrm{LK}}}^2 \sin(\theta_{0\mathrm{LK}} - \theta_0)\big]\theta_1 \\ &- k_{\mathrm{LK}}{R_{\mathrm{LK}}}^2 \sin(\theta_{0\mathrm{LK}} - \theta_0)\,\theta_2 \\ &= W_{\mathrm{CWT}}R_{\mathrm{CWT}}\cos(\theta_{\mathrm{CWT}} + \theta_0) \end{aligned} \tag{B.5}$$

The second EOM is derived in a similar manner by summing moments about the main trunnion in Figure B.4.

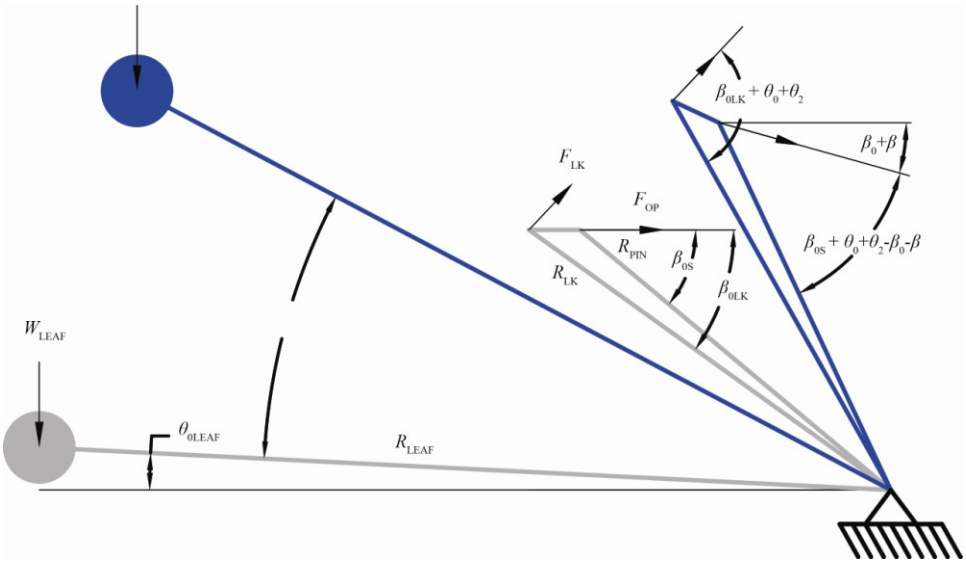

Figure B.4: FBD of Leaf for Dynamic Analysis

$$\begin{aligned} I_{\mathrm{LF}}\ddot{\theta_2} = &-W_{\mathrm{LF}}R_{\mathrm{LF}}\cos(\theta_{0\mathrm{LEAF}}+\theta_0+\theta_2) \\ &+F_{\mathrm{LK}}R_{\mathrm{LK}}\sin(\beta_{0\mathrm{LK}}+\theta_0+\theta_2) \\ &-F_{\mathrm{OP}}R_{\mathrm{PIN}}\sin(\beta_{0\mathrm{S}}+\theta_0-\beta_0+\theta_2-\beta) \end{aligned} \tag{B.6}$$

In Equation B.6, β_0 is a constant for a given value of θ_0, and β is a function of θ_2. Using the same trigonometric identities as in Equations B.2, the following linearization of angles in Equation B.6 is

$$\begin{aligned} \cos(\beta_{0\mathrm{LEAF}}+\theta_0+\theta_2) &\approx \cos(\beta_{0\mathrm{LEAF}}+\theta_0)-\theta_2\ \sin(\beta_{0\mathrm{LEAF}}+\theta_0) \\ \sin(\beta_{0\mathrm{LK}}+\theta_0+\theta_2) &\approx \sin(\beta_{0\mathrm{LK}}+\theta_0)+\theta_2\ \cos(\beta_{0\mathrm{LK}}-\theta_0) \\ \sin(\beta_{0\mathrm{S}}+\theta_0-\beta_0+\theta_2-\beta) & \\ &\approx \sin(\beta_{0\mathrm{S}}+\theta_0-\beta_0)+\ (\theta_2-\beta)\cos(\beta_{0\mathrm{S}}+\theta_0-\beta_0) \end{aligned} \tag{B.7}$$

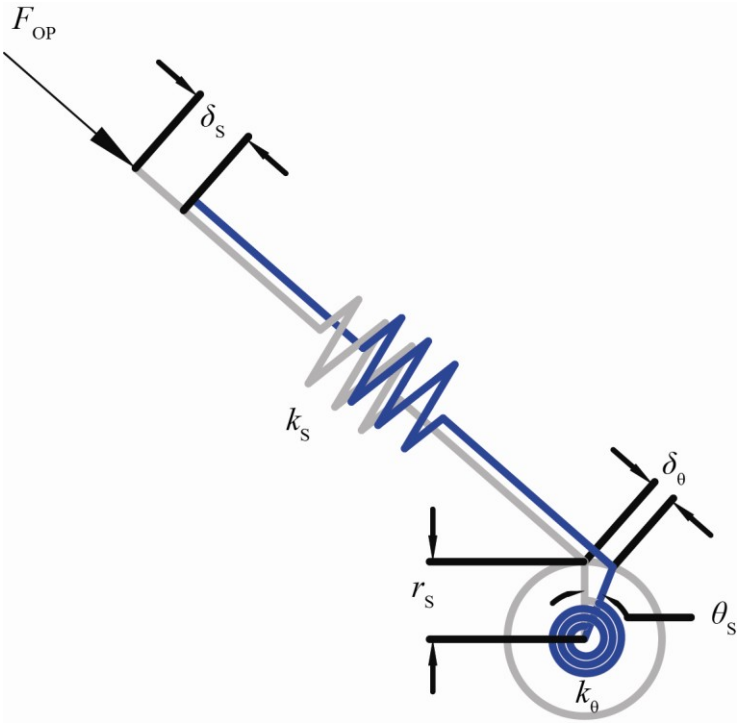

Figure B.5: FBD of Operating Strut/Drive Shaft Model

Figure B.5 illustrates the assumptions used to model the interaction of the operating strut and drive shaft as springs in series. The axial force in the operating strut is related directly to the torque in the drive shaft by Equation 2.1 in Chapter II. Torque is related to the torsional spring stiffness by

$$T = k_\theta \theta_S = k_\theta \frac{\delta_\theta}{r_S} \tag{B.8}$$

The total deformation in the springs representing the operating struts and drives shafts is

$$\delta_{TOT} = \delta_s + \delta_\theta = \frac{F_{OP}}{k_s} + \frac{F_{OP} r_s^2}{k_\theta} \tag{B.9}$$

This total deformation corresponds to the displacement along the operating strut's axis at the connection of the leaf and operating strut and is a function of known geometry and θ_2, as illustrated in Figure B.6.

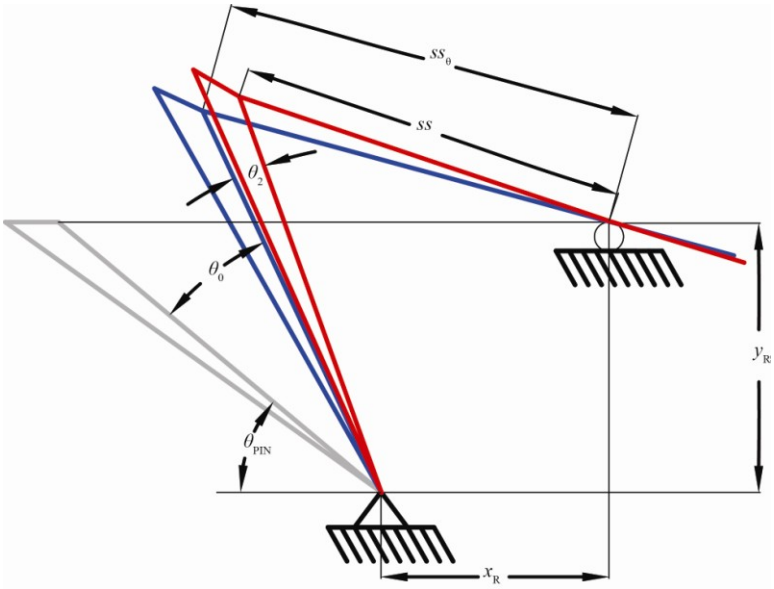

Figure B.6: Geometry of Operating Strut Deformation

The expression of δ_{TOT} as a function of known geometry and θ_2 is nonlinear with respect to θ_2

$$\begin{aligned}&\delta_{\mathrm{TOT}}\\&= ss_{\theta}\\&-\sqrt{\left(x_{\mathrm{R}}+\ R_{\mathrm{PIN}}\cos(\theta_{\mathrm{PIN}}+\theta_0+\theta_2)\right)^2\ +\left(y_{\mathrm{R}}+\ R_{\mathrm{PIN}}\sin(\theta_{\mathrm{PIN}}+\theta_0+\theta_2)\right)^2}\end{aligned} \tag{B.10}$$

At θ_0, B.10 may be expressed as a linear function of θ_2

$$\delta_{\mathrm{TOT}} = \eta\ \theta_2 \tag{B.11}$$

The factor η_2 was approximated numerically; values of η for a given angle θ_0 and small angle θ_2 are constant and provided in Table B.1.

Table B.1: Numerical Approximations of η for various angles of opening, θ_0

Angle of Opening, θ_0 (Deg.)	0	20	40	60	75
η (Feet/rad)	30.54	35.26	38.68	39.89	35.99

Equations B.9 and B.11 lead to the following expression for F_{OP}

$$F_{\mathrm{OP}} = \frac{k_s k_\theta}{k_s r_s^2 + k_\theta}\ \eta\theta_2 \tag{B.12}$$

Substituting Equations B.7 and B.12 into Equation B.6 and eliminating products of small angles yields the second EOM,

$$\begin{aligned} I_{\mathrm{LF}}\ddot{\theta_2} + \Bigg[\frac{k_s k_\theta}{k_s r_s^2 + k_\theta}\ \eta R_{\mathrm{PIN}} \sin(\beta_{0s} + \theta_0 - \beta_0) \\ + \ k_{\mathrm{LK}} {R_{\mathrm{LK}}}^2 \sin(\beta_{0\mathrm{L}} - \theta_0) \\ - \ W_{\mathrm{LF}} R_{\mathrm{LF}} \sin(\beta_{0L} + \theta_0)\Bigg]\theta_2 \\ - k_{\mathrm{LK}} {R_{\mathrm{LK}}}^2 \sin(\beta_{0L} - \theta_0)\theta_1 = \ - W_{\mathrm{LF}} R_{\mathrm{LF}} \sin(\beta_{0\mathrm{L}} + \theta_0) \end{aligned} \tag{B.13}$$

Equations B.5 and B.13 are the coupled equations describing the simplified dynamic behavior of a Strauss Heel Trunnion Bascule Bridge. The following equations assign variables to coefficients of θ_1 and θ_2 in Equations B.5 and B.13.

$$C_{\mathrm{CWTC}} = W_{\mathrm{CWT}} R_{\mathrm{CWT}} \cos(\theta_{\mathrm{CWT}} + \theta_0) \tag{B.14}$$

$$C_{\mathrm{CWT}} = W_{\mathrm{CWT}} R_{\mathrm{CWT}} \sin(\theta_{\mathrm{CWT}} + \theta_0) \tag{B.15}$$

$$C_{\mathrm{LK}} = k_{\mathrm{LK}} {R_{\mathrm{LK}}}^2 \sin(\theta_{0\mathrm{LK}} - \theta_0) \tag{B.16}$$

$$C_{\mathrm{ST}} = \frac{k_{\mathrm{s}} k_{\theta}}{k_{\mathrm{s}} r_{\mathrm{s}}^2 + k_{\theta}} \eta R_{\mathrm{PIN}} \sin(\beta_{0\mathrm{s}} + \theta_0 - \beta_0) \tag{B.17}$$

$$C_{\mathrm{LK2}} = k_{\mathrm{LK}} {R_{\mathrm{LK}}}^2 \sin(\beta_{0\mathrm{L}} - \theta_0) \tag{B.18}$$

$$C_{\mathrm{LF}} = W_{\mathrm{LF}} R_{\mathrm{LF}} \sin(\beta_{0L} + \theta_0) \tag{B.19}$$

$$C_{\mathrm{LF2}} = W_{\mathrm{LF}} R_{\mathrm{LF}} \sin(\beta_{0L} + \theta_0) \tag{B.20}$$

Substituting B.14-B.20 into B.6 and B.13

$$I_{\mathrm{CWT}} \ddot{\theta_1} + [C_{\mathrm{CWT}} + C_{\mathrm{LK}}]\theta_1 - C_{\mathrm{LK}} \theta_2 = C_{\mathrm{CWTC}} \tag{B.21}$$

$$I_{\mathrm{LF}} \ddot{\theta_2} + [C_{\mathrm{ST}} + C_{\mathrm{LK2}} - C_{\mathrm{LF}}]\theta_2 - C_{\mathrm{LK2}}\, \theta_1 = -C_{\mathrm{LF2}} \tag{B.22}$$

In matrix format, Equations B.21 and B.22 are expressed as (repeated from Chapter II)

$$\begin{bmatrix} I_{\mathrm{CWT}} & 0 \\ 0 & I_{\mathrm{LF}} \end{bmatrix} \begin{Bmatrix} \ddot{\theta_1} \\ \ddot{\theta_2} \end{Bmatrix} - \begin{bmatrix} C_{\mathrm{CWT}} + C_{\mathrm{LK}} & -C_{\mathrm{LK}} \\ -C_{\mathrm{LK2}} & C_{\mathrm{ST}} + C_{\mathrm{LK2}} - C_{\mathrm{LF}} \end{bmatrix} \begin{Bmatrix} \theta_1 \\ \theta_2 \end{Bmatrix} = \begin{bmatrix} C_{\mathrm{CWTC}} \\ -C_{\mathrm{LF2}} \end{bmatrix} \tag{2.5}$$

The natural frequencies of the system may be calculated by solving the following eigenvalue problem (repeated from Chapter II)

$$\left| \begin{bmatrix} C_{\mathrm{CWT}} + C_{\mathrm{LK}} & -C_{\mathrm{LK}} \\ -C_{\mathrm{LK2}} & C_{\mathrm{ST}} + C_{\mathrm{LK2}} - C_{\mathrm{LF}} \end{bmatrix} - \omega_{\mathrm{n}}{}^2 \begin{bmatrix} I_{\mathrm{CWT}} & 0 \\ 0 & I_{\mathrm{LF}} \end{bmatrix} \right| = 0 \qquad (2.6)$$

Table B.2 provides the numerical values of the natural frequencies given by the solution of Equations 2.6 and 2.7.

Table B.2: Preliminary Dynamic Results (Repeated)

Angle (Deg.)	f_{n1} **(Hz)**			f_{n2} **(Hz)**		
	Eq. (2.7)	**SAP2000 2D**	**SAP2000 3D**	**Eq. (2.7)**	**SAP2000 2D**	**SAP2000 3D**
0	0.71	0.70	0.29	6.36	6.33	1.44
20	0.84	0.83	0.38	6.24	6.24	1.52
40	0.95	0.92	0.40	5.72	5.41	1.63
60	1.03	0.97	0.40	4.75	3.94	0.72
75	0.98	0.88	0.37	3.61	2.52	0.63

Once the natural frequencies are known, mode shapes of the structure may be determined by solving the following equations

$$\left(\begin{bmatrix} C_{\mathrm{CWT}} + C_{\mathrm{LK}} & -C_{\mathrm{LK}} \\ -C_{\mathrm{LK2}} & C_{\mathrm{ST}} + C_{\mathrm{LK2}} - C_{\mathrm{LF}} \end{bmatrix} - \omega_{\mathrm{i}}{}^2 \begin{bmatrix} I_{\mathrm{CWT}} & 0 \\ 0 & I_{\mathrm{LF}} \end{bmatrix} \right) \begin{Bmatrix} \varphi_{1\mathrm{i}\_\theta} \\ \varphi_{2\mathrm{i}\_\theta} \end{Bmatrix} = 0 \qquad (B.23)$$

The assumption that $\varphi_{1\mathrm{i}\_\theta}$ is unity allows for the calculation of $\varphi_{2\mathrm{i}\_\theta}$ and the modal deflection profile for each angle of opening. Table B.3 displays the numerical mode shape values.

Table B.3: Numerical Values of Mode Shapes

Angle (Deg.)	Mode 1			Mode2		
	f_n (Hz)	φ_{11_θ}	φ_{21_θ}	f_n (Hz)	φ_{12_θ}	φ_{22_θ}
0	0.71	1.00	0.98	6.36	1.00	-0.36
20	0.84	1.00	0.98	6.24	1.00	-0.36
40	0.95	1.00	0.97	5.72	1.00	-0.37
60	1.03	1.00	0.95	4.75	1.00	-0.38
75	0.98	1.00	0.93	3.61	1.00	-0.38

While the mode shapes vary with θ_0, the mode shapes for 0 degrees are shown in Figure B.7. These are representative of all the modal deformations for the 2 DOF system. The rotations θ_1 and θ_2 are in phase while vibrating at the first natural frequency and out of phase while vibrating at the second natural frequency.

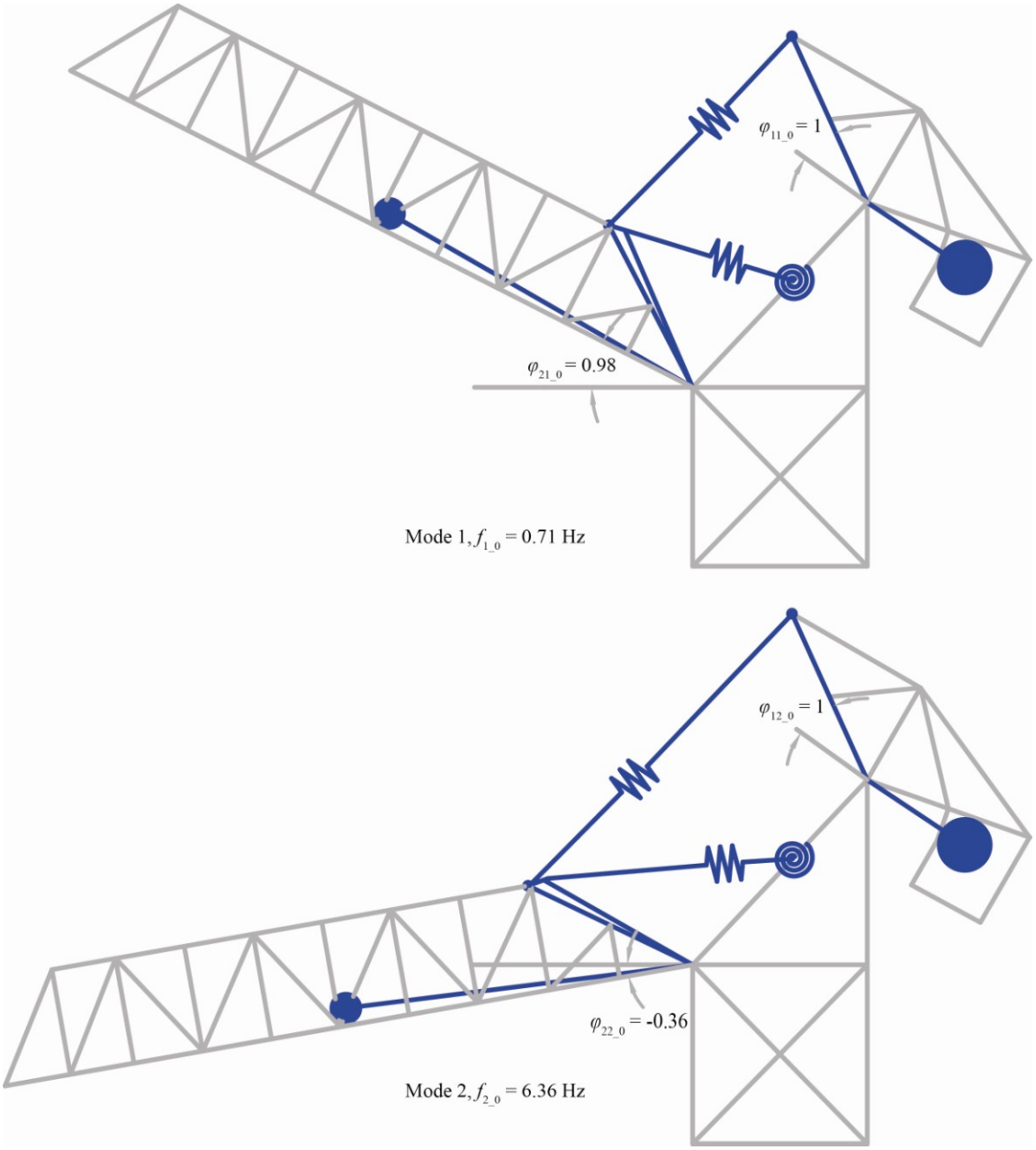

Figure B.7: Mode Shapes for $\theta_0 = 0$ Degrees

APPENDIX C
EXAMPLE OF COMPETITIVE NEURAL NETWORKS

In order to examine the performance of a competitive array of neural networks, a visual example has been created to compare traditional neural networks (i.e. single networks) to an array of competitive neural networks. In this example, a two dimensional grid is divided into four regions identified by the four colored shapes shown in Figure C.1.

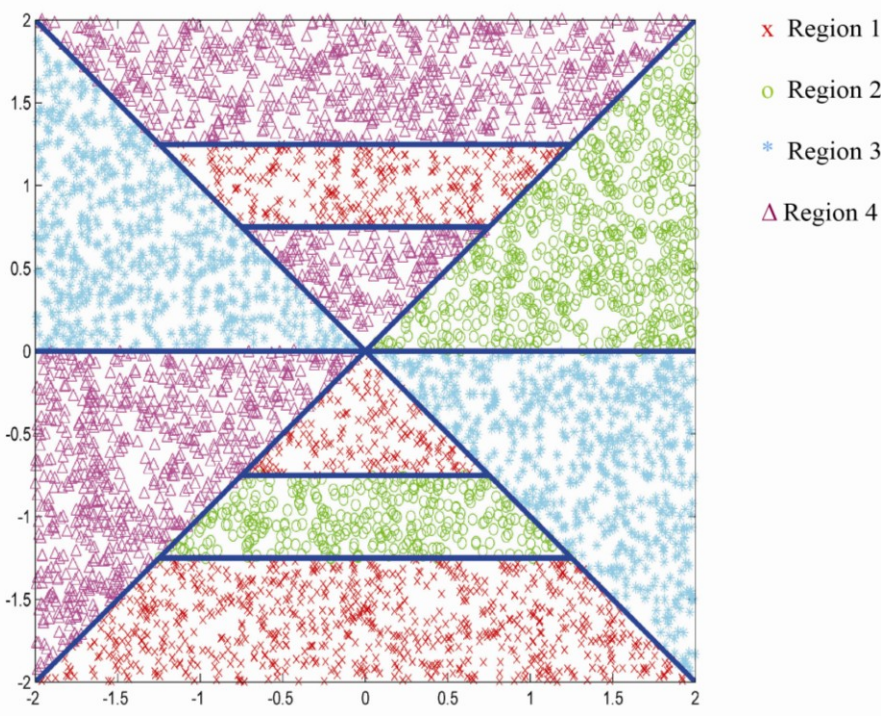

Figure C.1: Example Pattern

The regions could be an abstract representation of different operational states of a bridge structure with each colored region identifying an operational state. The input

vector for this example is a two dimensional coordinate, and the output is a classification region based on the coordinate's location on the grid shown in Figure C.1. For example, the point (1.5, 0.5) corresponds to Region 2. The goal of this neural network is to learn the region boundaries and correctly classify a given input vector without the explicit inequalities that define the regions. The regions in C.1 are disjoint and thus are more difficult to classify than simple, linearly separable boundaries (Haykin 1999).

Four single, individual, back-propagation neural networks with varying architectures were trained on 400 input/output pairs. After the four networks were trained, 500 additional pairs were simulated on the resulting networks to examine the ability of each individual network to learn the complicated boundaries of Figure C.1. Additionally, a competitive array comprised of the same four untrained individual networks was trained on the same 400 input/output pairs. Similarly to producing results with trained individual networks, 500 additional pairs were simulated by the competitive array. The only difference in the training and simulation of the individual networks and the competitive array was the method of training; architectures, training input/output pairs, and simulation input/output pairs were identical. MATLAB's Neural Network Toolbox is implemented in the algorithm (MATLAB 2011). Each individual network produced a plot of its predicted classifications; the competitive array produced one plot of classification predictions. Each classification prediction was plotted at the simulated input coordinate on the grid. A correct classification produces the correct region shape and color. Figures C2.2-C2.6 compare the classification output of the 500 simulation input pairs for the set of four single networks and the results for the competitive array of four single networks to the correct classification image. If all networks were to perform perfectly, the images in each of Figures C.2-C.6 would be identical.

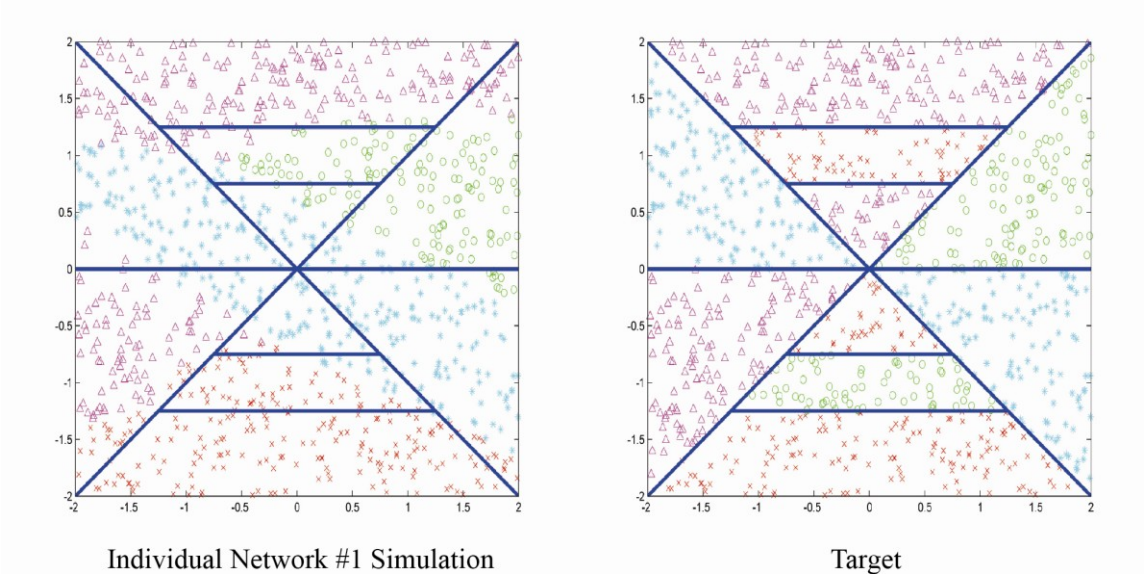

Figure C.2: Results of Neural Network Simulation from Individual Neural Network #1

The percentage of correct classifications from Network #1 was 66.7%. The network was able to correctly classify portions of the larger regions, but the smaller middle regions were classified incorrectly.

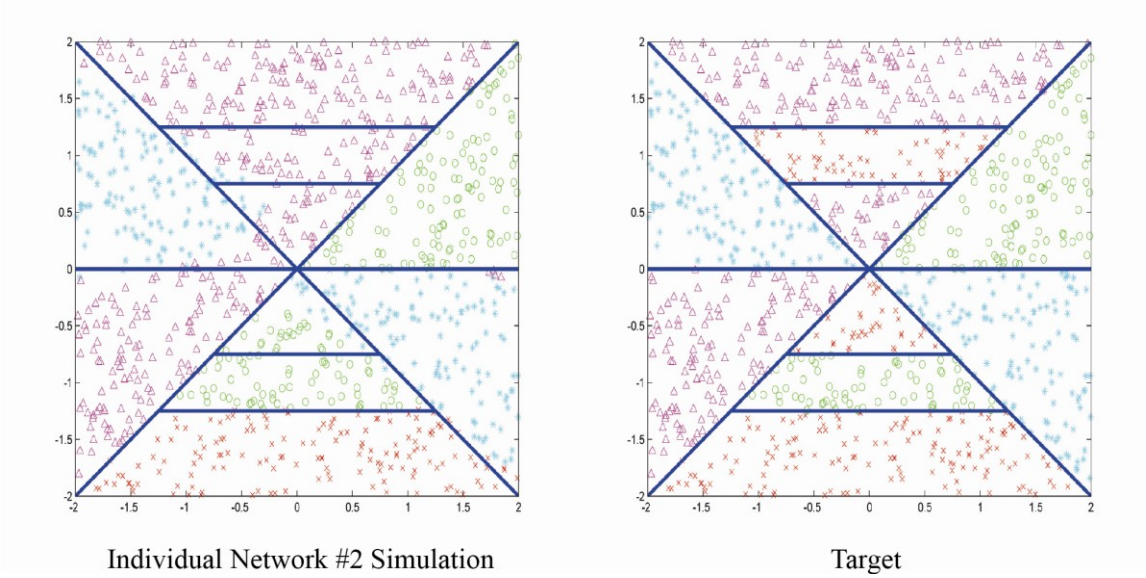

Figure C.3: Results of Neural Network Simulation from Individual Neural Network #2

The percentage of correct classifications from Network #2 was 86.1%. Performance is improved over Network #1, but the smaller portions of Region 1 classified incorrectly as neighboring Regions.

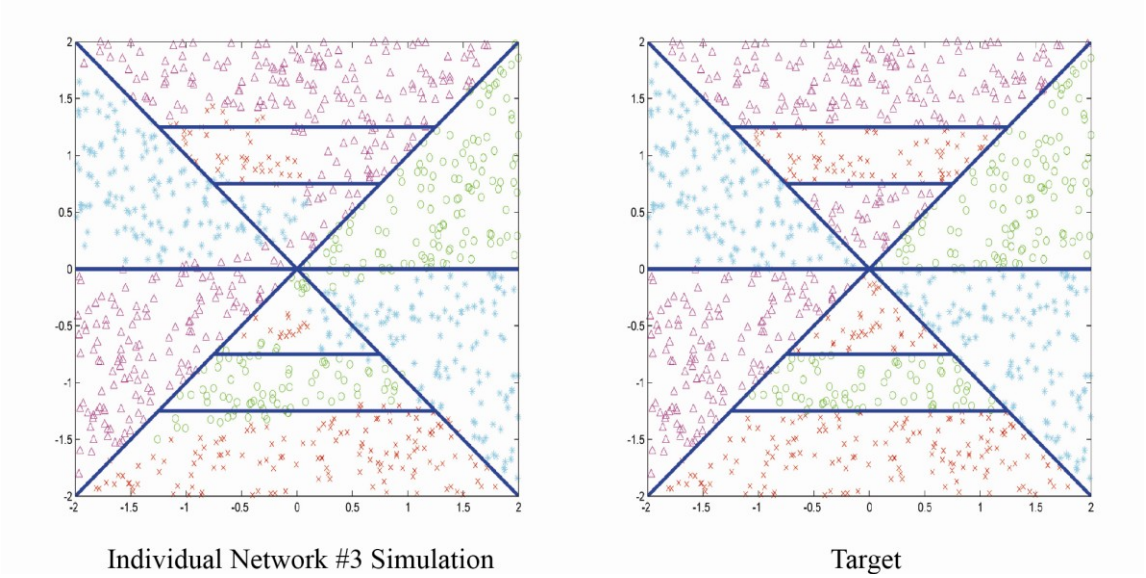

Figure C.4: Results of Neural Network Simulation from Individual Neural Network #3

The percentage of correct classifications from Network #3 was 87.1%. The performance of this network was superior to all other single networks. Large regions were classified correctly, and portions of smaller, disjoint regions were correctly classified. Classifications were unreliable on the boundaries. Figure C.4 illustrates the incorrect classification of Region 3 just left of the origin as Region 4. Region 4 was mapped as a continuous region from the top of the grid to the bottom left hand quadrant; disjoint regions in this region were misclassified.

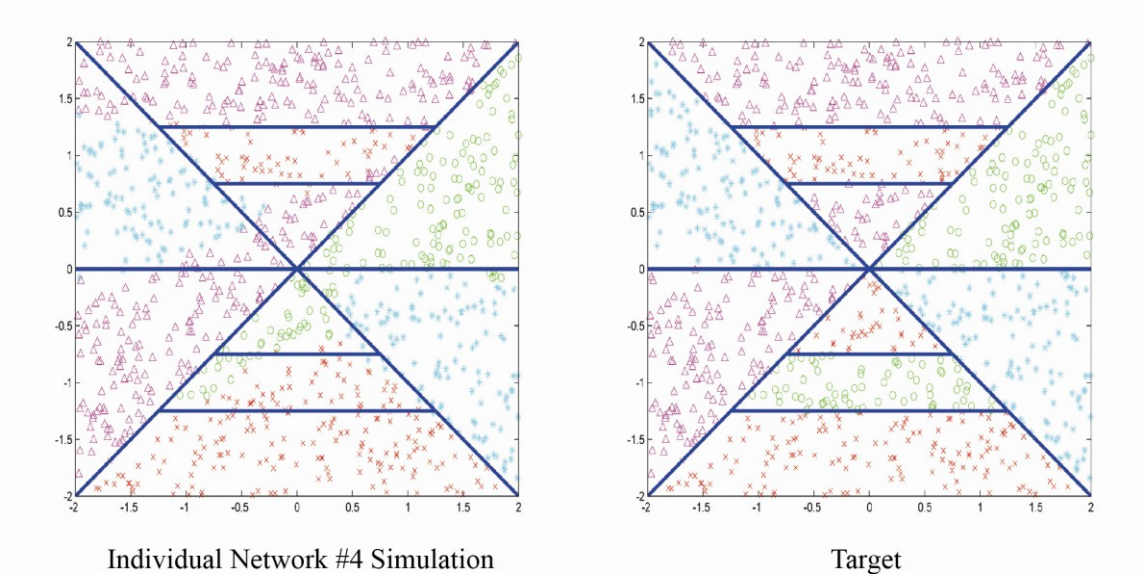

Figure C.5: Results of Neural Network Simulation from Individual Neural Network #4

The percentage of correct classifications from Network #4 was 84.6%. This network performed in a similar manner as Network #3, but with less accuracy.

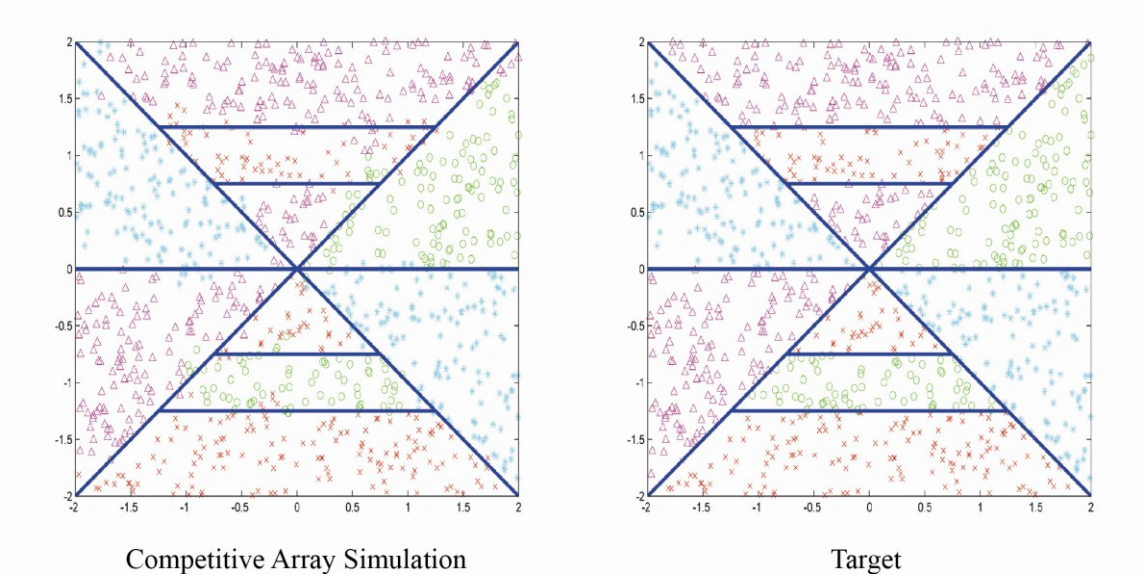

Figure C.6: Results of Neural Network Simulation from the Competitive Array of Networks

The percentage of correct classifications in the competitive array of neural networks was 91%. In addition, the competitive array was able to determine distinct disjoint regions. While some boundary misclassifications occurred, there are no incorrect continuous regions that ignore the presence of disjoint regions.

The competitive array of networks outperforms each of the single networks as its image closely resembles the target image in Figure C.6. Single networks achieve 66.7-87.1% correct classification percentages while the competitive network achieved 91.0% correct classification. In addition to superior correct classification percentages, the overall pattern regions were more accurately represented. This example illustrates the improvement in performance by neural networks when competition is implemented.

APPENDIX D
ELECTRICAL RESISTANCE STRAIN GAGE PARAMETERS

This appendix presents derivations and results for strain gage circuitry used on the Salmon Bay Bridge testbed. Equations relating voltage potential, resistance change, and mechanical strain are reviewed, and applications of specific strain gage configurations are presented.

The notion of change in resistance with strain of a material was discovered by Lord Kelvin in 1856 (Beckwith et al. 1995). The relation between the axial strain in a strain gage and the change in resistance is given by the following equation (Hambley 2005, Beckwith et al. 1995).

$$\varepsilon_{\mathrm{i}} = \frac{1}{F_{\mathrm{Gi}}}\frac{\Delta R_{\mathrm{i}}}{R_{\mathrm{i}}} \tag{D.1}$$

The gage factor is supplied by the manufacturer for each specific strain gage and is a function of resistivity, Poisson's ratio, and gage length. Typical values for F_G are near 2.0 for most gages. With the use of Equation D.1 one must only accurately measure the small changes in resistance for a given gage, and the strain can be ascertained; the Wheatstone bridge, shown in Figure D.1, is commonly used to precisely measure changes in resistance. Each resistor arm (indicated numerically) may or may not contain a strain gage. An active arm has a variable resistance strain gage; a resister in an arm without a strain gage is called a completion resistor.

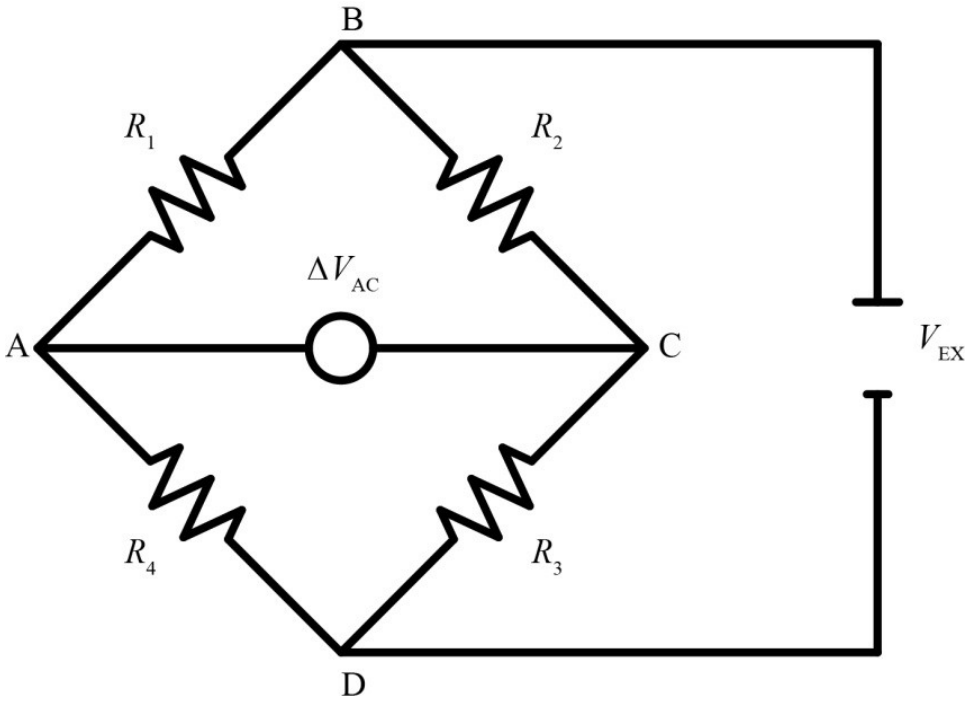

Figure D.1: Wheatstone Bridge Schematic (Repeated)

Initially, the bridge is balanced and the voltage drop across AC is zero. Equation D.2 provides the necessary relationship between arm resistances to ensure a balanced condition.

$$\frac{R_1}{R_4} = \frac{R_2}{R_3} \tag{D.2}$$

The resistance experienced by any arm is the change in resistance in the gage, ΔR_i, plus the initial resistance of the gage, R_{0i}, and is expressed in Equation D.3.

$$R_i = R_{0i} + \Delta R_i \tag{D.3}$$

Changes in resistance of the four arms will lead to a voltage output across AC; the bridge will remain balanced if Equation D.2 is satisfied, even if some of the values of R_i change. The voltage change, ΔV_{AC}, from 0 is a function of the excitation voltage, arm resistances, and the changes in those resistances, given by Equation D.4.

$$\Delta V_{AC} = V_{EX}\left[\left(\frac{R_{02}+\Delta R_2}{R_{02}+\Delta R_2+\ R_{03}+\Delta R_3}\right) - \left(\frac{R_{01}+\Delta R_1}{R_{01}+\Delta R_1+\ R_{04}+\Delta R_4}\right)\right] \tag{D.4}$$

Substituting Equation D.1 into D.4 and assuming all initial resistances and gage factors are equal results in an expression for the change in voltage as a function of the strain in each arm of the Wheatstone Bridge.

$$\Delta V_{AC} = V_{EX}\left[\left(\frac{1+\epsilon_2 F_G}{2+F_G(\epsilon_2\ +\epsilon_3)}\right) - \left(\frac{1+\epsilon_1 F_G}{2+F_G(\epsilon_1\ +\epsilon_4)}\right)\right] \tag{D.5}$$

Strains in Equation D.5 can be related through mechanics for combinations of strain gage number and orientation. Figure D.2 illustrates the perpendicular half bridge strain gage configuration on an axial specimen.

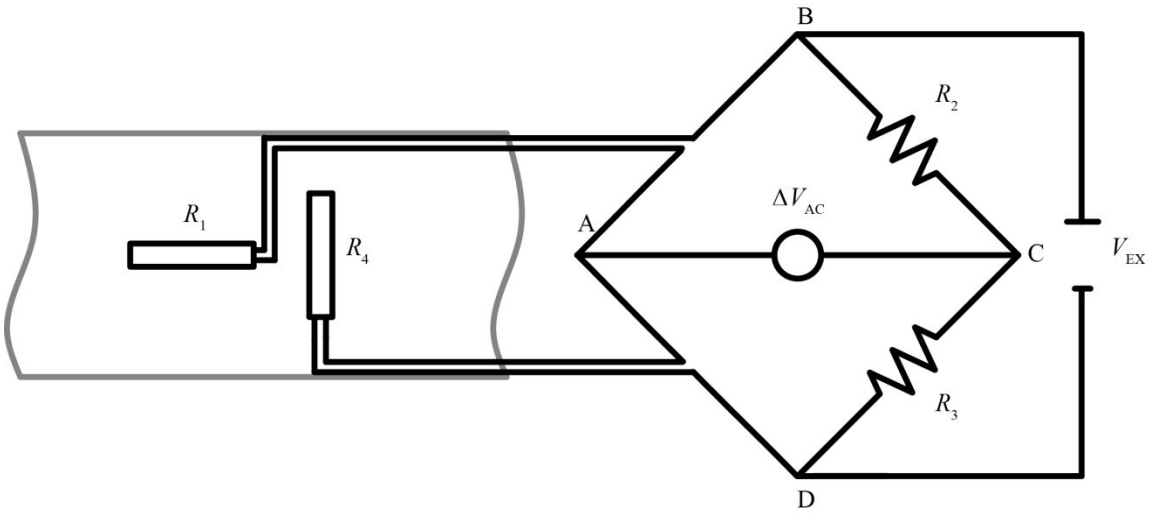

Figure D.2: Half Bridge Configuration

For the configuration shown in Figure D.2, the mechanical strain, ε_1, in arm 1 is related to the mechanical strain in arm 4 by Poisson's ratio

$$\epsilon_4 = -\nu\epsilon_1 \tag{D.6}$$

Strain in arms 2 and 3 are identically zero. Substituting Equation D.6 into D.5 results in the following non-linear expression.

$$\Delta V_{\mathrm{AC}} = V_{\mathrm{EX}}\left[\left(\frac{1}{2}\right) - \left(\frac{1+\epsilon_1 F_{\mathrm{G}}}{2+F_{\mathrm{G}}\epsilon_1(1-\nu)}\right)\right] \tag{D.7}$$

ΔV_{AC} is not linear in strain. Figure D.3 displays a plot of Equation D.7. Vertical lines represent yield strains for 30 ksi steel.

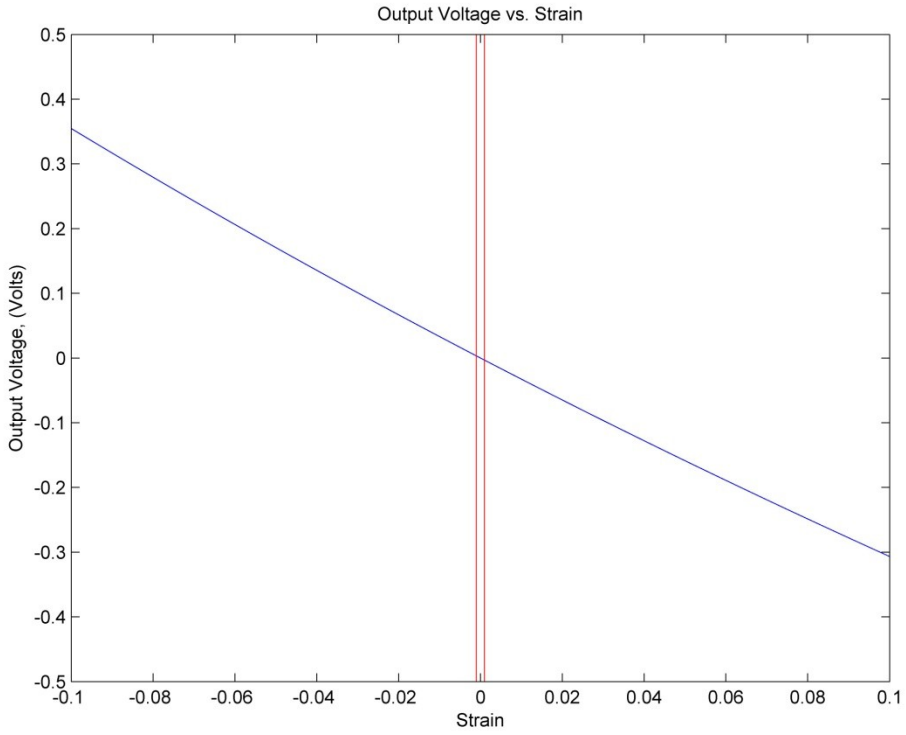

Figure D.3: Plot of Output Voltage vs. Strain

Figure D.3 illustrates that voltage change is nonlinearly related to strain, but for the ranges of voltage change associated with typical strain values below yield and shown in Figure D.4, a linear approximation is appropriate.

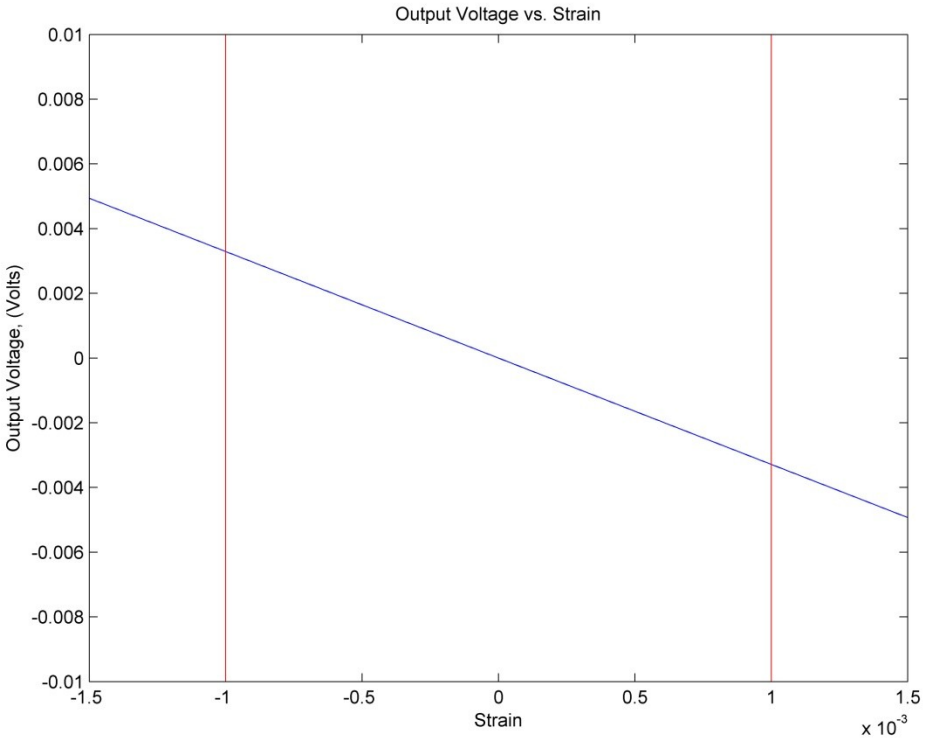

Figure D.4: Plot of Output Voltage vs. Strain for Typical Strain Values

This linear approximation can be made by examining the derivative of Equation D.7 near zero.

$$\frac{d\Delta V_{\mathrm{AC}}}{d\epsilon_1} = \frac{V_{\mathrm{EX}} F_{\mathrm{G}} (1+\nu)}{\left(2 + F_{\mathrm{G}}\epsilon_1 (1-\nu)\right)^2} \tag{D.8}$$

For small values of strain Equation D.8 becomes

$$\frac{d\Delta V_{\mathrm{AC}}}{d\epsilon_1} = \frac{V_{\mathrm{EX}} F_{\mathrm{G}} (1+\nu)}{4} \tag{D.9}$$

Strain can now be linearly approximated by

$$\epsilon_1 = \frac{4\Delta V_{\mathrm{AC}}}{V_{\mathrm{EX}} F_{\mathrm{G}}(\,1+\nu)} \tag{D.10}$$

A similar process can be completed for quarter bridge and full bridge configurations which result in different relationships between strain and output voltage. Equations D.11 and D.12 represent linearzied expressions for strain.

$$\epsilon_1 = \frac{4\Delta V_{\mathrm{AC}}}{V_{\mathrm{EX}} F_{\mathrm{G}}} \tag{D.11}$$

$$\epsilon_1 = \frac{\Delta V_{AC}}{V_{EX} F_G} \tag{D.12}$$

Comparison of Equations D.10- D.12 reveal that additional strain gages can increase the sensitivity of the measurement. Sensitivity is measured by the bridge constant which is defined as the ratio of ΔV_{AC} for a given configuration to ΔV_{AC} for a quarter bridge configuration. Table D.1 gives details for quarter bridge, half bridge perpendicular, and full bridge torque configurations.

Table D.1: Strain Gage Configuration Summary

Configuration	**Active Arms**	**Bridge Constant**	**Temperature Compensation**
Quarter Bridge	1- Longitudinal	1	no
Half Bridge, Perpendicular	1- Longitudinal, 4- Perpendicular	1+ν	yes
Full Bridge	1, 2, 3, 4 at 45°	4	yes

Examination of Equation D.2 leads to observations about compensating for temperature. If Equation D.2 is not satisfied, then an output voltage will occur. If a quarter bridge circuit is used, then the change in resistance due to temperature variation, ΔR_1, will cause an unbalanced condition and effect the measured voltage. The resistance of all completion resistors and the strain gage are assumed to be equal.

$$\frac{R + \Delta R_{\mathrm{T}}}{R} \neq \frac{R}{R} \tag{D.13}$$

If mechanical strain is also occurring, then the voltage change from mechanical strain and resistance change due to temperature cannot be separated. Clearly, if arms 1 and 4 or arms 1 and 2 experience the same temperature variation, then the output voltage is unaffected by temperature. The perpendicular half bridge and torque full bridge configurations compensate for variations in temperature.

APPENDIX E

COUNTERWEIGHT TRUSS MEMBER STRESS RANGE SUMMARIES

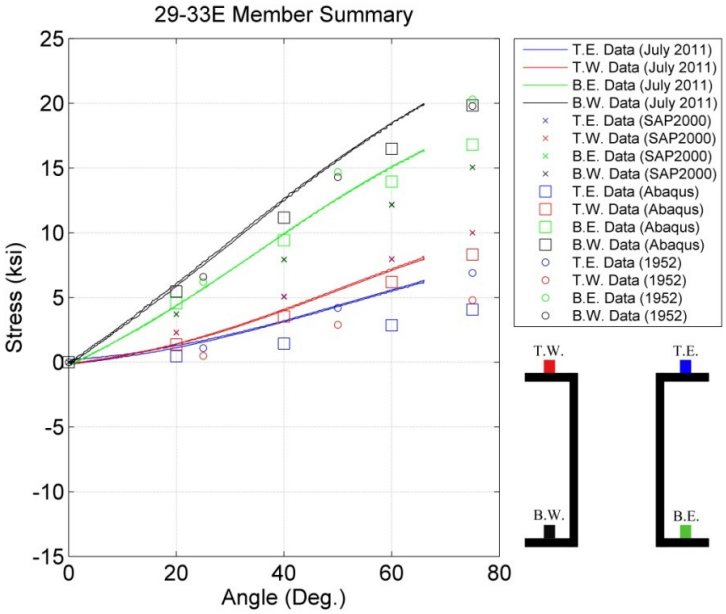

Figure E.1: Stress vs. Angle Member Summary, 29-33E

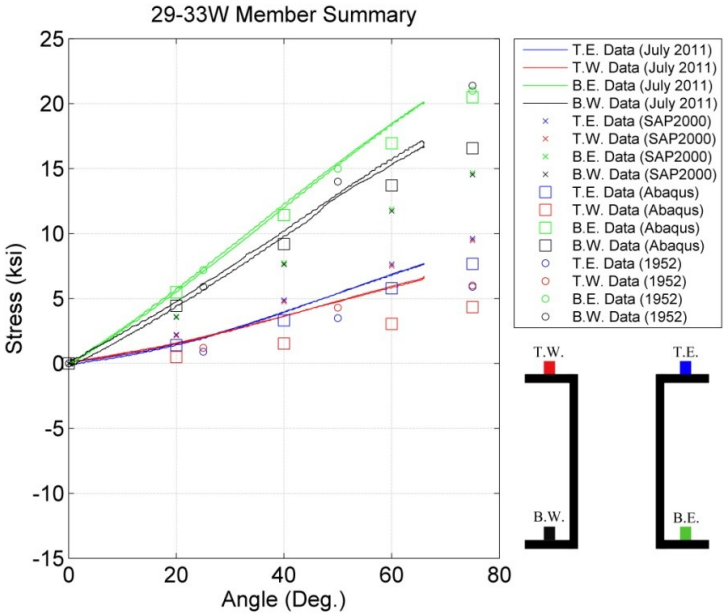

Figure E.2: Stress vs. Angle Member Summary, 29-33W

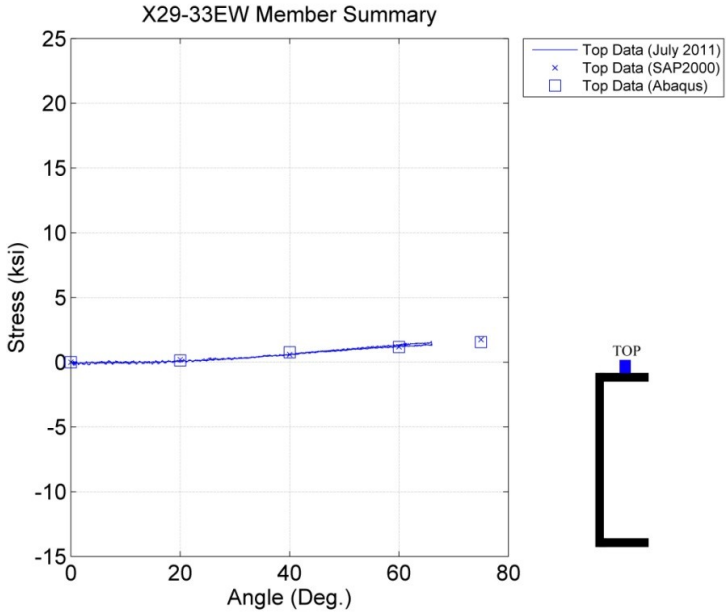

Figure E.3: Stress vs. Angle Member Summary, X29-33EW

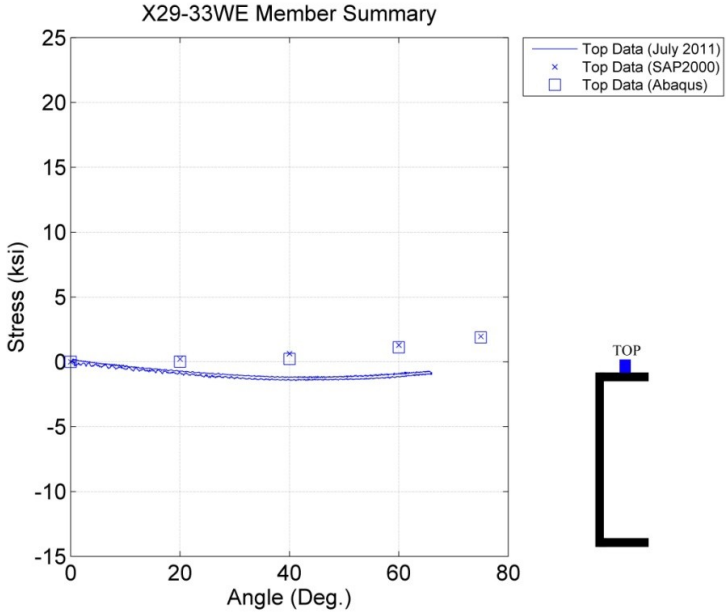

Figure E.4: Stress vs. Angle Member Summary, X29-33WE

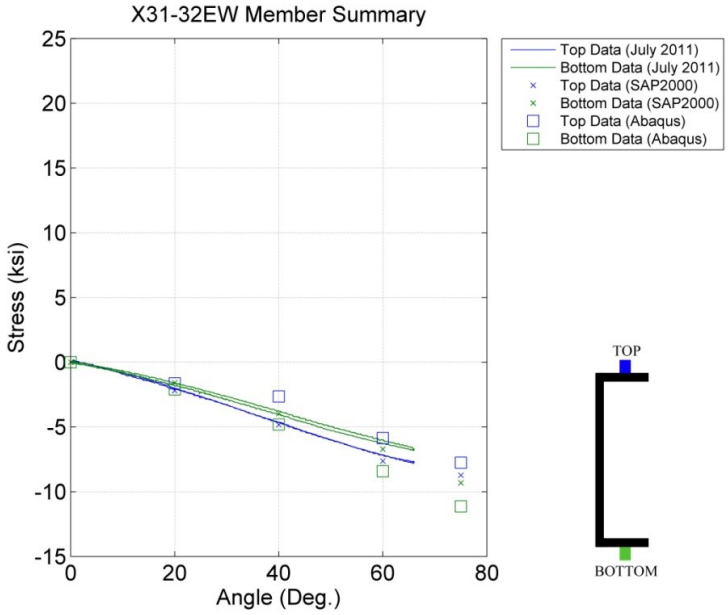

Figure E.5: Stress vs. Angle Member Summary, X31-32EW

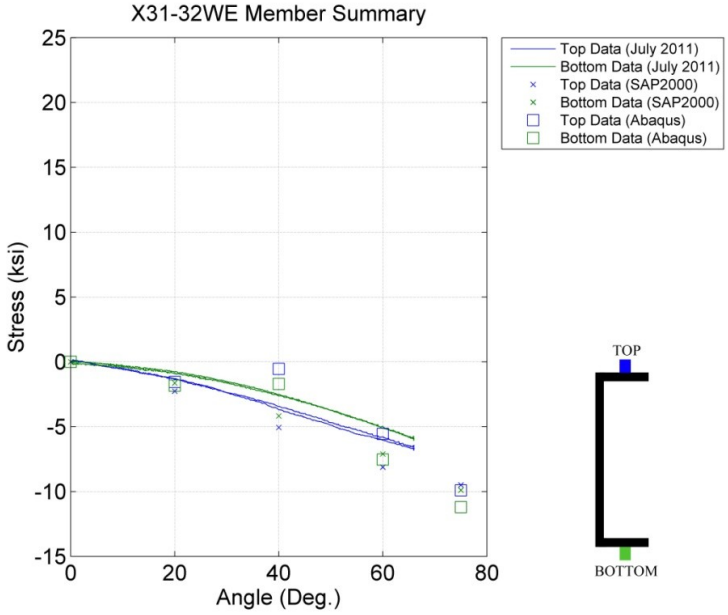

Figure E.6: Stress vs. Angle Member Summary, X31-32WE

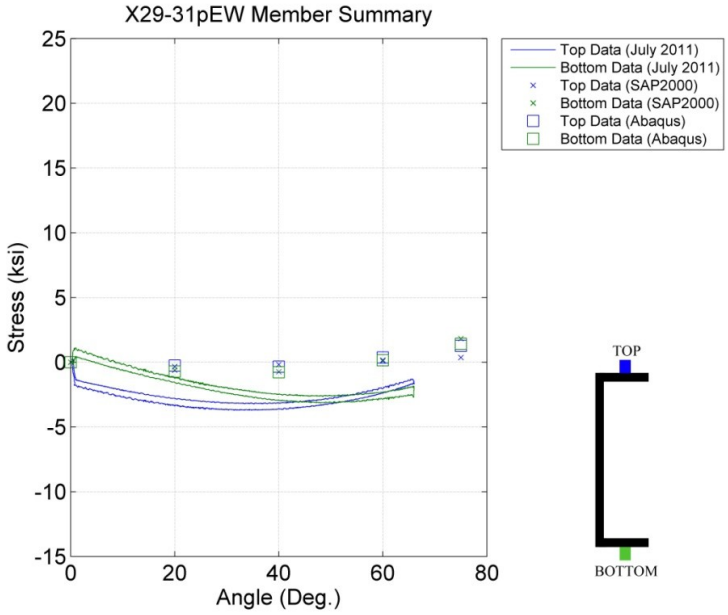

Figure E.7: Stress vs. Angle Member Summary, X29-31'EW

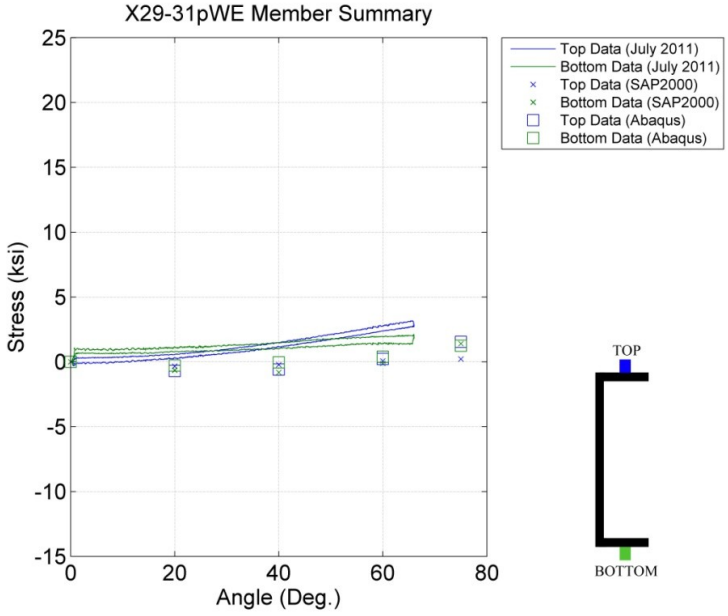

Figure E.8: Stress vs. Angle Member Summary, X29-31'WE

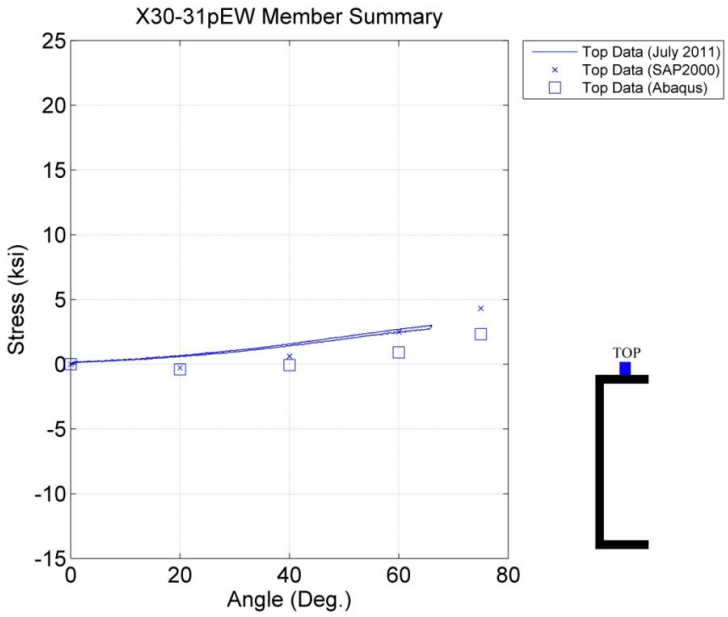

Figure E.9: Stress vs. Angle Member Summary, X30-31'EW

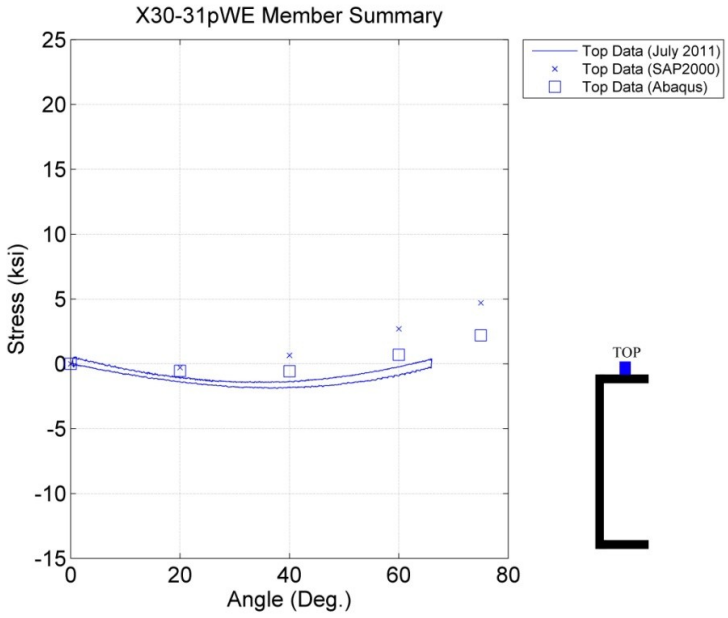

Figure E.10: Stress vs. Angle Member Summary, X30-31'WE

APPENDIX F

SUMMARY OF IMPARIED AND UNIMPAIRED STRESS RANGES

Table F.1: Stress Differences Between Impaired and Unimpaired Data Streams, ABAQUS

Member	Location	I.C. 1	I.C. 2	I.C. 3	I.C. 4	I.C. 5	I.C. 6	I.C. 7	I.C. 8	I.C. 9	I.C. 10	I.C. 11	I.C. 12	I.C. 13	I.C. 14	I.C. 15	I.C. 16	I.C. 17
29-33 E	TE	0.0	1.4	24.8	1.9	-8.7	0.1	-1.6	0.2	-8.5	-1.4	-7.3	-0.1	-2.0	2.5	-0.2	-2.5	-0.6
	TW	0.0	4.2	22.4	2.5	26.2	0.1	0.7	0.2	4.7	-2.3	-6.2	-0.8	-2.2	1.1	-0.2	-0.7	-0.6
	BE	0.0	3.6	-27.4	4.1	-9.1	0.5	-0.3	0.4	-3.5	1.3	2.7	1.2	4.1	-1.5	0.4	1.3	0.9
	BW	0.0	-11.2	-20.1	-9.5	-14.6	0.2	3.1	0.2	11.2	0.6	4.4	1.3	5.2	-2.2	0.7	1.2	1.3
29-33 W	TE	0.0	0.1	0.8	0.1	1.4	4.2	21.1	-0.7	-5.9	-0.6	-1.7	-1.9	-5.4	0.1	4.3	-0.5	-1.2
	TW	0.0	0.1	-1.6	0.1	-4.6	2.0	25.8	2.5	-17.4	-0.1	-2.0	-1.4	-7.0	-0.2	3.5	-0.6	-2.1
	BE	0.0	0.1	2.9	0.2	5.8	-12.9	-19.7	-7.0	15.9	1.2	5.2	0.6	4.3	0.3	-5.6	1.5	1.2
	BW	0.0	0.5	-0.3	0.4	-0.9	4.3	-27.5	4.5	0.3	1.2	4.1	1.1	2.2	0.1	-2.7	1.0	0.8
X29-33EW	Top	0.0	1.6	2.8	2.1	-3.2	-2.4	-2.6	-2.0	-4.0	0.6	1.2	-1.1	-3.1	1.2	0.3	0.4	-0.7
X29-33WE	Top	0.0	-1.9	-1.6	-0.4	12.0	2.1	3.2	2.7	2.5	-1.4	-3.6	0.3	0.4	-0.9	1.0	-1.1	0.1
X31-32EW	Top	0.0	0.0	0.4	0.1	0.4	0.1	-1.4	0.1	-3.9	-6.2	-6.8	15.7	2.3	-0.5	0.1	-2.0	9.5
	Bottom	0.0	-0.1	-0.5	0.1	-2.1	-0.2	-1.0	-0.5	-0.1	-2.7	-10.1	2.0	5.1	-0.6	1.1	-1.5	-5.3
X31-32WE	Top	0.0	0.1	-1.1	0.0	-1.0	-0.2	-0.2	0.2	4.3	18.9	6.5	-7.9	-10.0	2.8	-5.0	12.0	-2.1
	Bottom	0.0	0.0	-0.8	-0.2	1.5	-0.2	-1.0	0.3	-0.3	5.3	8.6	-3.9	-11.9	2.8	-4.2	-2.5	-1.3
X29-31'EW	Top	0.0	-0.4	-3.0	-0.4	-2.7	0.3	2.1	0.2	2.4	-0.7	-2.3	0.7	2.5	-0.7	1.3	-0.5	0.5
	Bottom	0.0	0.0	-0.2	-0.1	-1.6	0.2	1.1	0.2	4.2	-1.1	-4.0	0.9	3.1	-0.5	1.0	-1.1	0.7
X29-31'WE	Top	0.0	0.3	2.1	0.3	2.3	-0.4	-3.0	-0.2	-1.7	0.8	2.8	-0.6	-2.1	0.6	-1.4	0.7	-0.4
	Bottom	0.0	0.2	1.1	0.2	2.0	-0.1	-0.2	-0.2	-4.8	0.9	3.5	-1.0	-3.6	0.6	-0.8	0.9	-0.9
X30-31'EW	Top	0.0	0.4	2.7	0.4	3.3	-0.4	-2.6	-0.3	-5.1	1.4	4.6	-1.3	-4.7	1.1	-1.9	1.0	-1.0
X30-31'WE	Top	0.0	-0.4	-2.7	-0.4	-3.6	0.4	2.7	0.3	4.5	-1.3	-5.1	1.3	4.0	-1.0	2.0	-1.3	0.7

Table F.2: Stress Differences Between Impaired and Unimpaired Data Streams, SAP2000

Member	Location	I.C. 1	I.C. 2	I.C. 3	I.C. 4	I.C. 5	I.C. 6	I.C. 7	I.C. 8	I.C. 9	I.C. 10	I.C. 11	I.C. 12	I.C. 13	I.C. 14	I.C. 15	I.C. 16	I.C. 17
29-33 E	TE	0.0	-6.5	-2.5	-0.9	-1.8	0.5	-0.5	-10.0	-14.5	-0.6	-0.1	-11.6	0.1	-8.2	-1.2	-11.8	-3.8
	TW	0.0	-7.2	1.8	-0.9	-2.0	-3.6	3.6	-10.0	9.2	-3.1	2.7	-11.6	0.7	-7.0	0.0	-8.2	2.7
	BE	0.0	-0.6	5.3	-0.4	3.2	-3.7	3.6	-15.0	0.1	-3.8	4.0	4.6	5.2	5.7	0.8	1.0	3.2
	BW	0.0	-1.2	9.5	-0.4	2.9	-7.8	7.7	-15.0	23.9	-6.3	6.8	4.6	5.8	6.9	2.1	4.6	9.7
29-33 W	TE	0.0	1.9	-6.9	-2.1	-0.9	3.7	-3.5	9.6	-9.6	2.8	-3.0	0.7	-11.3	0.1	-7.0	2.9	-7.8
	TW	0.0	-2.7	-6.4	-1.9	-1.0	-0.6	0.4	-15.2	-9.5	-0.2	-0.7	0.0	-11.4	-1.4	-8.4	-4.0	-11.3
	BE	0.0	9.9	-1.1	3.0	-0.4	7.9	-7.6	24.9	-14.7	7.0	-6.1	6.0	4.6	2.1	7.0	10.2	4.4
	BW	0.0	5.4	-0.7	3.1	-0.5	3.6	-3.7	0.1	-14.5	4.1	-3.8	5.3	4.5	0.7	5.7	3.3	0.9
X29-33EW	Top	0.0	1.2	-4.1	0.8	-4.0	-13.4	13.1	121.8	135.4	-7.9	8.6	0.4	-6.8	5.3	-5.4	-0.6	-6.0
X29-33WE	Top	0.0	-4.1	1.3	-4.1	0.7	13.4	-13.1	140.7	117.4	8.8	-7.7	-6.9	0.4	-5.4	4.9	-6.2	-0.5
X31-32EW	Top	0.0	0.9	4.1	-4.2	12.2	26.2	-25.6	32.5	-25.5	21.9	-26.8	-35.4	-38.9	-5.1	14.4	0.6	4.6
	Bottom	0.0	-5.5	1.3	-13.3	4.9	22.7	-22.2	18.7	-21.0	19.8	-19.6	-32.6	-37.4	-10.5	1.5	-3.1	-0.7
X31-32WE	Top	0.0	3.9	0.7	12.6	-4.3	-26.2	25.6	-26.5	31.4	-27.5	21.4	-39.5	-34.8	15.0	-5.1	4.6	0.5
	Bottom	0.0	1.1	-5.5	5.1	-12.7	-22.7	22.2	-21.7	18.0	-20.1	19.2	-38.2	-32.0	1.3	-10.1	-0.6	-2.9
X29-31'EW	Top	0.0	-13.4	12.5	-15.1	15.1	25.1	-24.6	-30.5	23.3	10.7	-8.0	-9.9	8.9	-14.2	11.1	-12.8	10.8
	Bottom	0.0	-15.6	15.7	-10.0	9.8	32.4	-31.7	-32.6	32.5	22.2	-26.3	-10.8	11.3	-5.2	7.8	-13.0	13.1
X29-31'WE	Top	0.0	12.7	-13.1	15.4	-14.8	-25.1	24.6	24.4	-29.3	-8.2	10.4	9.1	-9.7	11.3	-13.8	11.3	-12.2
	Bottom	0.0	16.0	-15.3	9.8	-10.0	-32.4	31.7	33.8	-31.3	-27.0	21.6	11.5	-10.6	7.9	-5.3	13.7	-12.5
X30-31'EW	Top	0.0	16.4	-16.4	13.4	-13.7	-29.5	28.8	34.5	-36.8	-12.7	35.2	12.3	-12.1	10.0	-10.0	14.0	-14.8
X30-31'WE	Top	0.0	-16.7	16.0	-13.8	13.3	29.5	-28.9	-38.4	33.1	36.1	-12.2	-12.3	12.1	-10.0	9.9	-15.4	13.4

Table F.3: Stress Percent Differences Between Impaired and Unimpaired Data Streams, ABAQUS

Member	Location	I.C. 1	I.C. 2	I.C. 3	I.C. 4	I.C. 5	I.C. 6	I.C. 7	I.C. 8	I.C. 9	I.C. 10	I.C. 11	I.C. 12	I.C. 13	I.C. 14	I.C. 15	I.C. 16	I.C. 17
29-33 E	TE	0.0	35.0	612.1	47.9	-213.7	3.2	-40.3	3.9	-209.5	-33.8	-179.4	-2.9	-50.1	60.6	-5.0	-62.4	-15.0
	TW	0.0	50.2	269.8	29.6	315.4	0.9	8.2	2.1	56.7	-27.5	-74.8	-9.5	-26.7	13.0	-2.8	-8.2	-6.8
	BE	0.0	21.5	-162.7	24.3	-54.2	3.1	-1.9	2.2	-20.7	7.8	15.8	7.2	24.6	-9.0	2.2	7.6	5.4
	BW	0.0	-56.6	-101.3	-48.1	-73.6	0.8	15.6	1.0	56.5	3.1	22.1	6.5	26.0	-10.9	3.4	5.9	6.4
29-33 W	TE	0.0	0.7	10.1	1.5	18.8	54.9	274.6	-9.0	-77.3	-7.9	-21.9	-24.4	-70.5	1.2	55.4	-6.8	-15.3
	TW	0.0	2.0	-36.9	2.0	-105.7	46.1	594.3	58.0	-400.7	-2.5	-45.4	-32.9	-160.3	-3.5	80.1	-13.7	-49.0
	BE	0.0	0.6	14.2	1.1	28.2	-62.8	-95.9	-34.0	77.6	5.9	25.3	3.0	20.9	1.4	-27.5	7.1	5.7
	BW	0.0	2.8	-1.6	2.6	-5.7	26.2	-165.9	27.1	1.8	7.3	24.6	6.4	13.4	0.5	-16.3	6.1	4.5
X29-33EW	Top	0.0	104.6	178.2	134.9	-204.7	-151.7	-170.5	-128.0	-256.9	35.9	77.2	-73.5	-197.2	75.5	20.3	28.8	-46.7
X29-33WE	Top	0.0	-101.3	-84.5	-19.9	631.4	111.3	171.3	140.3	131.6	-72.2	-190.9	15.4	22.2	-47.6	50.5	-60.1	5.1
X31-32EW	Top	0.0	0.0	-4.6	-1.2	-4.9	-1.9	18.6	-1.3	50.8	79.5	88.3	-203.1	-29.8	6.9	-1.3	25.4	-123.0
	Bottom	0.0	0.5	4.8	-1.1	18.5	2.1	9.1	4.9	0.5	23.9	90.7	-18.0	-45.6	5.6	-10.1	13.5	47.7
X31-32WE	Top	0.0	-1.1	11.3	-0.4	10.0	2.0	2.2	-2.4	-43.6	-190.3	-65.4	79.5	100.5	-28.6	50.4	-121.2	21.1
	Bottom	0.0	0.3	7.5	1.8	-13.4	1.9	8.9	-2.9	2.9	-47.5	-77.0	34.7	106.6	-25.1	37.1	22.4	12.0
X29-31'EW	Top	0.0	-32.1	-238.2	-30.3	-215.7	24.2	164.7	13.9	187.5	-51.6	-180.5	58.5	200.1	-53.8	98.9	-39.8	43.0
	Bottom	0.0	-2.9	-14.2	-7.3	-116.1	13.8	76.0	15.6	294.1	-74.9	-280.4	63.1	218.5	-37.0	71.9	-77.1	46.9
X29-31'WE	Top	0.0	22.5	171.4	22.2	188.2	-36.1	-239.6	-17.8	-140.8	63.3	222.7	-50.1	-166.3	49.9	-116.7	56.9	-29.9
	Bottom	0.0	10.9	70.5	13.6	131.1	-3.6	-13.2	-11.4	-312.0	61.1	223.5	-64.7	-233.7	38.0	-53.4	55.8	-55.9
X30-31'EW	Top	0.0	17.4	122.1	17.6	148.7	-18.2	-117.5	-13.7	-226.0	61.0	203.2	-57.0	-207.8	47.3	-84.4	43.7	-45.8
X30-31'WE	Top	0.0	-16.6	-121.5	-17.8	-161.8	19.8	122.1	13.9	203.7	-60.9	-231.8	58.1	183.6	-44.2	89.8	-59.5	32.3

Table F.4: Stress Percent Differences Between Impaired and Unimpaired Data Streams, SAP2000

Member	Location	I.C. 1	I.C. 2	I.C. 3	I.C. 4	I.C. 5	I.C. 6	I.C. 7	I.C. 8	I.C. 9	I.C. 10	I.C. 11	I.C. 12	I.C. 13	I.C. 14	I.C. 15	I.C. 16	I.C. 17
29-33 E	TE	0.0	-65.5	-25.0	-9.1	-17.6	4.9	-5.1	-100.0	-144.8	-6.2	-0.9	-116.0	1.0	-81.9	-12.4	-118.5	-37.8
	TW	0.0	-71.4	17.6	-9.1	-20.2	-36.3	35.8	-100.0	92.2	-30.9	26.6	-115.5	6.7	-69.4	-0.1	-81.4	27.2
	BE	0.0	-3.9	35.1	-2.3	21.3	-24.4	23.7	-99.9	1.0	-25.5	26.8	30.6	34.9	37.8	5.5	6.4	21.5
	BW	0.0	-7.9	63.3	-2.3	19.5	-51.8	50.8	-99.9	158.4	-41.9	45.1	30.7	38.6	45.9	13.7	30.9	64.6
29-33 W	TE	0.0	19.5	-71.4	-21.9	-8.9	38.8	-36.4	100.2	-100.0	29.1	-30.8	7.6	-117.9	0.6	-73.3	30.1	-81.6
	TW	0.0	-28.5	-67.9	-20.3	-10.1	-6.2	4.5	-160.2	-100.0	-1.7	-6.9	0.3	-120.9	-14.5	-88.5	-42.6	-119.9
	BE	0.0	67.5	-7.6	20.1	-3.0	53.8	-51.6	169.3	-99.9	47.9	-41.5	40.8	31.3	14.2	47.6	69.6	30.1
	BW	0.0	36.8	-4.7	21.6	-3.7	24.7	-25.1	0.6	-99.9	28.1	-26.1	36.4	30.8	4.5	38.9	22.7	6.3
X29-33EW	Top	0.0	66.4	-235.6	45.5	-226.2	-764.8	747.3	6944.3	7717.6	-448.5	490.9	21.8	-389.3	301.8	-309.2	-34.5	-342.9
X29-33WE	Top	0.0	-210.5	64.4	-207.5	36.8	684.3	-668.6	7175.9	5985.4	451.0	-390.9	-353.3	19.3	-277.0	251.6	-315.5	-25.9
X31-32EW	Top	0.0	-10.7	-46.5	48.3	-139.6	-300.2	293.3	-372.7	292.8	-251.1	307.1	405.8	445.6	58.5	-165.0	-7.0	-52.4
	Bottom	0.0	58.8	-13.5	142.7	-52.9	-243.6	238.1	-200.2	225.8	-212.2	209.9	350.4	401.9	112.6	-16.6	32.8	7.6
X31-32WE	Top	0.0	-41.3	-6.9	-132.2	45.4	275.8	-269.5	278.9	-330.8	289.8	-224.9	416.2	366.2	-157.9	54.2	-48.1	-5.6
	Bottom	0.0	-11.0	56.1	-51.2	128.5	229.4	-224.2	219.6	-182.0	203.0	-194.6	386.7	323.9	-13.5	101.8	6.0	29.6
X29-31'EW	Top	0.0	-3608.2	3365.5	-4081.6	4073.0	6775.2	-6621.3	-8233.7	6286.0	2891.1	-2159.9	-2676.1	2409.5	-3828.0	2998.0	-3442.6	2916.5
	Bottom	0.0	-856.6	858.0	-548.4	535.3	1778.2	-1738.3	-1785.5	1779.7	1219.3	-1439.1	-592.6	620.7	-284.2	430.0	-714.1	719.3
X29-31'WE	Top	0.0	5844.0	-6020.2	7076.6	-6809.6	-11535.8	11273.4	11185.0	-13431.3	-3773.7	4788.2	4178.6	-4473.2	5210.2	-6336.1	5186.6	-5611.1
	Bottom	0.0	1139.5	-1089.7	695.4	-712.8	-2311.1	2259.2	2407.3	-2227.3	-1923.4	1541.7	821.9	-755.8	559.6	-379.8	973.2	-891.1
X30-31'EW	Top	0.0	378.7	-378.8	310.9	-317.2	-683.6	668.1	800.0	-853.0	-295.0	814.7	284.3	-279.5	231.2	-230.4	323.6	-342.2
X30-31'WE	Top	0.0	-355.4	339.9	-293.8	282.9	627.1	-613.0	-816.7	703.9	767.9	-259.1	-261.4	256.3	-213.5	210.1	-327.7	285.0

APPENDIX G
NOMENCLATURE

A^*	impaired cross sectional area
A_0	unimpaired cross sectional area
AAR	Association of American Railroads
a_r	rigid body radial acceleration
a_θ	rigid body tangential acceleration
BNSF	Burlington Northern Santa Fe Railroad
C.G.	center of gravity
C_{CWT}	counterweight coefficient
C_{LF}	leaf coefficient
C_{LF2}	leaf coefficient
C_{LK}	counterweight link coefficient
C_{ST}	operating strut coefficient
CWT	counterweight
DOF	degree of freedom
E	modulus of elasticity
e_i	unit vector
$(EI)_{FULL}$	unimpaired modulus of rigidity
$(EI)_{PARTIAL}$	impaired modulus of rigidity
EOM	equation of motion
f_{ni}	natural frequency of the ith mode
F_{ax}	horizontal reaction at operating strut pin
$F_{ax'}$	reaction at operating strut pin
F_{ay}	vertical reaction at operating strut pin
$F_{ay'}$	reaction at operating strut pin
FBD	free body diagram
F_{by}	vertical reaction at operating strut roller
$F_{by'}$	reaction at operating strut roller
F_G	gage factor
FHWA	Federal Highway Administration
F_{OP}	force in the operating strut

F_r	rigid body radial inertial force
FRA	Federal Railroad Administration
F_θ	rigid body tangential inertial force
G	shear modulus of elasticity
I^*	impaired second moment of area
I.C.	impairment condition
I_0	unimpaired second moment of area
I_{LEAF}	mass moment of inertia of the leaf
$\theta_1, \dot{\theta}_1, \ddot{\theta}_1$	angular rotation, velocity, and acceleration about main trunnion
$\theta_2, \dot{\theta}_2, \ddot{\theta}_2$	angular rotation, velocity, and acceleration about counterweight trunnion
I_{CWT}	mass moment of inertia of the counterweight
J^*	impaired polar second moment of area
J_0	unimpaired polar second moment of area
J_S	polar moment of inertia of the drive shafts
k_i	transducer coefficients
k_{LK}	axial stiffness of counterweight link
k_S	axial stiffness of operating strut
k_θ	torsional stiffness of drive shaft
L	length
L_S	length of the drive shaft
M_{CWT}	mass of counterweight
M_{LK}	moment of force in counterweight link about trunnions
n	number of neural networks in an array
N	number of possible impairment conditions
$n_{(EI)}$	ratio of impaired and unimpaired moduli of rigidity
N.I.	neural image
NDE	Non-Destructive Evaluation
R_{0i}	initial gage resistance
R_i	Wheatstone bridge arm resistance
R_{LEAF}	radius to leaf C.G.
R_{LK}	radius to counterweight link
R_{PIN}	radius to operating strut pin

r_S	drive shaft radius
SHM	Structural Health Monitoring
SIDS	Structural Impairment Detection System
ss	effective length of operating strut
T	torque
T_{ADJ}	drive shaft torque adjusted for friction
T_{CLOSE}	drive shaft torque while closing
T_F	drive shaft friction torque
θ_i	discrete bridge angles for evaluation
T_{OPEN}	drive shaft torque while opening
V_{EX}	excitation voltage
V_{OUT}	output voltage
V_S	remote sense voltage
w_i	neural network weight
W_{LEAF}	leaf weight
W_{LK}	counterweight link weight
W_{OP}	operating strut weight
x,y,z	coordinates
x_0	location of operating strut C.G.
X_i	neural network input
x_R	horizontal distance between main trunnion and operating strut roller
$\bar{Y}$	neural network training vector
Y_i	simulated result from the ith neural network
y_R	vertical distance between main trunnion and operating strut roller
Y_{SIM}	neural network simulated output
Y_{TARGET}	neural network target output
α_0	impairment length ratio for SAP2000 analysis
α	rigid body angular acceleration
θ	operating strut angle
β_0	static operating strut angle
β_{0LK}	static reference angle for counterweight link
β_{0S}	static reference angle for operating strut
δ_1	deflection of counterweight link due to θ_1

δ_2	deflection of counterweight link due to θ_2
Δ_C	deflection of impaired midspan
Δ_{FULL}	deflection of unimpaired midspan
δ_{ij}	Kronecker delta
δ_{LK}	change in length of counterweight link
ΔR_i	change in arm resistance
δ_S	strut component of operating strut deflection
δ_{TOT}	operating strut deflection
ΔV_{AC}	change in voltage across Wheatstone bridge
δ_θ	shaft component of operating strut deflection
ε_i	strain
η	numerical relationship between δ_{TOT} and θ_2
θ	bridge angle of opening
θ_0	static bridge angle of opening
θ_{0LEAF}	static angle of radius to leaf
θ_{0LK}	initial angle of radius to counterweight link
θ_{EAST}	encoder bridge angle for east drive shaft
θ_{LEAF}	leaf angle
θ_{LK}	counterweight link angle
θ_{PIN}	angle of radius to operating pin
θ_{PIN}	angle of operating strut pin
θ_S	drive shaft rotation angle
σ	stress
φ	mode shape
φ_S	angle of twist of the drive shafts
ω_{ni}	circular natural frequency of the ith mode
ω	rigid body angular velocity

VITA

Name:	Brett Alan Story
Address:	607 D CE/TTI Building Zachry Department of Civil Engineering Texas A&M University 3136 TAMU College Station, TX 77843-3136
Email Address:	bstory@tamu.edu
Education:	B.S., Civil Engineering, Texas A&M University, 2005
	M.S., Civil Engineering, Texas A&M University, 2007
	Ph.D., Civil Engineering, Texas A&M University, 2012